Phononic and Photonic Semiconductor Nanostructures

Transport, coherence, confinement, and dynamics of phonons and excitons in single and periodic nanostructures

Dr. Markus Raphael Wagner
ORCID: 0000-0002-7367-5629

Habilitationsschrift
an der Fakultät II
Mathematik und Naturwissenschaften
der Technischen Universität Berlin

Lehrgebiet
Experimentalphysik

Vorsitzende des Habilitationsausschusses:
Prof. Dr. Andreas Knorr (TU Berlin, Germany)
Gutachter*innen:
Prof. Dr. Michael Kneissl (TU Berlin, Germany)
Prof. Dr. Janina Maultzsch (FAU Erlangen-Nürnberg, Germany)
Prof. Dr. Friedhelm Bechstedt (FSU Jena, Germany)
Prof. Dr. Bernard Gil (U Montpellier, France)
Prof. Dr. Marius Grundmann (U Leipzig, Germany)
Prof. Dr. Axel Hoffmann (TU Berlin, Germany)
Prof. Dr. Pablo Ordejón (ICN2, Spain)
Prof. Dr. Jim Speck (UCSB, USA)
Prof. Dr. Martin Stutzmann (Walter Schottky Institut, Germany)

Eröffnung des Habilitationsverfahrens: 22.04.2020
Tag des Habilitationskolloquiums: 03.07.2020
Fakultätsratsbeschluss über die Zuerkennung der Lehrbefähigung: 31.07.2020

Berlin 2020

Abstract

Semiconductor nanostructures form the basic building blocks for the majority of modern electronic and photonic components. The continuous reduction of their dimensions in the past decades has opened possibilities to manipulate phononic and photonic properties at the micro- and nanoscale. With decreasing structure sizes, heat in the form of atomic vibrations can drastically modify material properties and limit the performance of devices. This fact poses a major challenge for the design of nanoscale devices due to the complexity of controlling the heat flow at the nanoscale.

The present work provides an overview of the experimental methods and physical processes that are relevant for thermal investigations of semiconductor nanostructures. The experimental methods discussed in this work include optical techniques such as micro-Raman thermometry in its one- and two- laser version, frequency and time-domain thermoreflectance, and femtosecond pump-probe spectroscopy based on asynchronous optical sampling, as well as contact-based techniques such as the 3-omega method, scanning thermal microscopy, and the microchip suspended platform. A comparative overview of the state-of-the-art of these techniques highlights the most suitable experimental approach for materials with different structures and dimensions and identifies their main advantages and disadvantages with regard to spatial resolution and temperature sensitivity.

Following the discussion of the experimental techniques, the effects of geometry and artificial periodicity on the thermal properties of materials with reduced dimensionality are examined. The text provides an overview of phonon scattering mechanisms, phonon lifetimes, and the effects of phonon confinement on the modification of thermal properties in nanostructures. In addition, recent advances in the study of coherent and non-coherent phonon heat conduction in materials with reduced dimensionality are explained. These include thin films and quasi-2D membranes, nanostructures with second-order periodicity such as two-dimensional phononic crystals and superlattices, nanowires, and quantum dots. The work highlights own publications that are part of this thesis in conjunction with recent advances in the understanding and control of phonon mediated heat propagation.

Zusammenfassung

Halbleiternanostrukturen bilden die grundlegenden Bausteine für die überwiegende Zahl der modernen elektronischen und photonischen Bauelemente. Die kontinuierliche Reduzierung ihrer Dimensionen in den letzten Jahrzehnten hat Möglichkeiten zur Manipulation der phononischen und photonischen Eigenschaften im Mikro- und Nanobereich eröffnet. Mit sinkenden Strukturgrößen kann Wärme in Form von atomaren Schwingungen die Materialeigenschaften drastisch verändern und die Leistung von Bauteilen limitieren. Diese Tatsache stellt aufgrund der Komplexität der Steuerung des Wärmeflusses im Nanobereich eine große Herausforderung für das Design nanoskaliger Bauelemente dar.

Die vorliegende Arbeit gibt einen Überblick über die experimentellen Methoden und physikalischen Prozesse, die für thermische Untersuchungen von Halbleiternanostrukturen relevant sind. Die in dieser Arbeit diskutierten experimentellen Methoden umfassen sowohl optische Techniken wie die Mikro-Raman-Thermometrie in ihrer Ein- und Zwei-Laser-Version, die Thermoreflexion in der Frequenz- und Zeitdomäne und die Femtosekunden-Pump-Probe-Spektroskopie, als auch kontaktbasierte Techniken wie der 3-Omega-Methode, der Rasterthermomikroskopie und der freistehenden Mikrochip Plattform. Ein vergleichender Überblick über den Stand der Technik dieser Methoden zeigt den am besten geeigneten experimentellen Ansatz für Materialien mit unterschiedlicher Struktur und Dimension auf und identifiziert deren wesentliche Vor- und Nachteile hinsichtlich räumlicher Auflösung und Temperaturempfindlichkeit.

Nach der Abhandlung der experimentellen Techniken werden die Auswirkungen von Geometrie und künstlicher Periodizität auf die thermischen Eigenschaften von Materialien mit reduzierter Dimensionalität untersucht. Die Arbeit gibt einen Überblick über Phononenstreumechanismen, Phononenlebensdauern und die Auswirkungen des Phononeneinschlusses auf die Modifikation der thermischen Eigenschaften in Nanostrukturen. Darüber hinaus werden in der Arbeit die neuesten Fortschritte bei der Untersuchung der kohärenten und nicht kohärenten Phononenwärmeleitung in Materialien mit reduzierter Dimensionalität erläutert. Dazu gehören dünne Filme und quasi-2D-Membranen, Nanostrukturen mit Periodizität zweiter Ordnung wie zweidimensionale phononische Kristalle und Übergitter, Nanodrähte und Quantenpunkte. Der Text beleuchtet eigene Publikationen, die Teil dieser Arbeit sind, in Verbindung mit den jüngsten Fortschritten beim Verständnis und der Kontrolle der durch Phononen vermittelten Wärmeausbreitung.

Contents

1 Introduction

In the last century, a large diversity of research lines emerged targeting the fundamental and applied properties of the collective vibrations of lattice atoms of materials called phonons. Many works were driven by the discovery of inelastic light scattering as theoretically predicted by Brillouin [1] and experimentally shown by Raman [2] in the 1920s. Following these discoveries, research efforts focused on unraveling the detailed structure of the vibrational spectrum of materials. As phonons are the main heat carriers in most non-metallic materials, the study of the phononic properties of materials is closely linked to the study of the thermal properties and the propagation of heat. Although heat transport has been investigated for centuries, it is only with the advent of nanotechnology that advanced techniques have been developed to study its properties at the nanoscale. On macroscopic length scales, heat transport is described by Fourier's law, $Q = -k\nabla T$, where Q is the heat flux, k is the thermal conductivity, and T is the temperature. It builds on the classical concept that for a certain material with well-defined composition and structure, the thermal conductivity is an intrinsic property which is independent of the geometry and size of the material, just as other intrinsic properties such as density, specific heat, or electrical conductivity [3]. This characteristic has been confirmed by 200 years of experimental observations. However, at the nanoscale or at low temperatures (low phonon occupation), deviations from this classical behavior occur due to non-diffusive heat transport, i.e., when the typical dimensions of the material are comparable to the thermal phonon mean free path Λ_{th} which defines the average distance that thermal phonons can travel without being scattered.

In recent years, a fundamental problem in our understanding of heat has become apparent, partly driven by the successful fabrication of nanoscale devices for which heat plays a fundamental role. We were forced to address the problem of heat propagation through interfaces [4], at nanoscale hotspots [5], and at spatial scales below the thermal phonon mean free path [6], i.e., where the heat flux Q is far from equilibrium. In other words, time scales prior to the average thermal phonon relaxation time have to be considered. This non-equilibrium situation complicates the problem of addressing heat propagation. Despite recent progress in the study of thermal properties of structures with reduced spatial dimensions, a comprehensive understanding and description of heat transport and local energy distribution on

the nanoscale has not yet been achieved. The lack of knowledge and control of heat propagation in nanostructures on the one hand, and the raising need for a more efficient nanoscale energy management in high power electronics and photonics on the other hand, demonstrate the necessity of intensified research in this field.
From an application point of view, the ability to control and exploit heat propagation in semiconductor nanostructures constitutes one of the main challenges for the continued miniaturization of electronic components. It is essential in the development of novel technologies such as phase-change memory devices [7] and a broad range of applications in nano- and optoelectronics [8]. Consequently, the control of thermal energy quanta on the nanoscale is considered a crucial prerequisite for a variety of scientific and technological advances in the emerging field of nanoscale energy management. A better control over heat propagation promises more efficient thermal insulation [9, 10] and improved thermoelectric energy conversion [11–14]. In particular, 2D and quasi-2D materials such as graphene [15, 16] and ultra-thin Si membranes [17] are attracting increasing attention as thermal interface materials [18]. Moreover, the lack of interaction with a substrate and the capability of nanometer precise fabrication control promote these types of nanostructures to ideal model systems for the experimental and theoretical study of the fundamental physical mechanisms of heat propagation and thermal conductivity at the nanoscale. From a fundamental point of view, aspects such as the transition from the ballistic to the diffusive thermal transport regimes, hydrodynamic phonon transport, phonon coherence, or the spectral distribution of the phonon mean free path are examples for ongoing research areas where a deeper understanding is desirable. The multitude of open questions partially arises from the technical limitations imposed by the experimental methods available to study thermal transport at the nanoscale. For example, the concept of a phonon spectrometer (in analogy with an optical spectrometer) still remains an experimental challenge [19]. Despite these challenges, several proposals have recently appeared envisioning applications similar to those already achieved in electronics and photonics such as thermal diodes [20, 21], thermal cloaking [22–25], and phonon wave guiding [26, 27]. As promising as many of these developments may be, there is still a rather steep path from the early proof-of-concepts to their application in commercial devices.

1.1 Thesis scope and objectives

This cumulative thesis comprises scientific articles published in three main research topics: (i) thermal transport and phonon coherence in semiconductor nanostructures, (ii) photonic and electronic properties of III-nitride nanostructures, and (iii) excitonic, vibrational, and functional properties of II-oxides and its nanostructures. It is based on publications which were completed during my time as postdoctoral researcher at the Technical University Berlin TUB and the University of Technology Sydney UTS (2011-2012), as Marie Curie postdoctoral fellow at the Catalan Insitute of Nanoscience and Nanotechnology ICN2 (2013-2015), and as principal investigator of the project A5 "Electronic Properties of Nanoscale Objects" within the collaborative research center CRC 787 "Semiconductor Nanophotonics: Materials, Models, Devices" at TUB (2016-2019). During these years, I have (co)authored 3 book chapters and 52 peer-reviewed publications, 48 of which are part of this cumulative thesis.

The focus of this thesis lies on the first of the three topics, i.e. experimental nanoscale thermal transport. The discussion in this part goes beyond a pure summary of my own publications but instead provides a more comprehensive overview of both experimental methodologies and physical processes, which are relevant for thermal studies of semiconductor nanostructures. In particular, the text focuses on recent developments addressing both experimental methodologies and physical phenomena related to thermal transport in nanostructures and discusses these advances in conjunction with my own works. In order to limit the extent of this cumulative work, the topics (ii) and (iii) follow a different approach. They do not attempt a comprehensive overview of their respective research fields, but rather provide a compressed summary of the main results of the scientific articles in this cumulative thesis. For a more comprehensive discussion of the "optical and structural properties of nitride based nanostructures" and "nitride microcavities and single quantum dots for classical and non-classical light emitters" including my contributions to these fields, the reader is referred to two book chapters with the same names [28, 29]. They are published within the book "Semiconductor Nanophotonics: Materials, Models, Devices" [30] which provides an in-depth view of the scientific progress achieved during the funding of the collaborative research center CRC 787. In addition, parts of my works on nitrides and oxides are also discussed in an extensive review article that focuses on the effects of polarity in GaN and ZnO materials and devices [31]. For a more detailed discussion on specific topics, the interested reader may refer to the original papers which are part of this thesis.

1.2 Thesis structure

Following the general introduction on nanoscale thermal transport in this chapter, the different experimental techniques for thermal transport studies are described in chapter 2. It provides an overview of the state-of-the-art of experimental techniques for the study of thermal properties at the nanoscale. The focus of the text lies on recent developments during the past decade. In particular, these include contact-free all optical techniques such as micro-Raman thermometry in its one- and two- laser version (2LRT), frequency and time-domain thermoreflectance (FDTR/TDTR), and femtosecond pump-probe spectroscopy based on asynchronous optical sampling (ASOPS) (chapter 2.1). The second part of this chapter focuses on contact-based techniques including the 3-omega (3ω) method, scanning thermal microscopy (SThM), and the microchip suspended platform (section 2.2). With the exception of FDTR and the microchip thermal platform, all of these techniques were applied within the publications comprising this cumulative thesis. The chapter closes with a brief outlook and highlights a few selected examples that constitute major experimental advances for nanoscale thermal transport studies in the past 2-3 years.

Chapter 3 builds on the previous discussion of experimental techniques by focusing on the scientific research questions that currently drive the field of nanoscale thermal transport. The first part of this chapter introduces relevant concepts that affect heat conduction at the nanoscale such as phonon scattering mechanisms, phonon confinement, and phonon dynamics. Subsequently, the discussion focuses on recent developments in the study of coherent and non-coherent heat transport in phononic metamaterials such as phononic crystals and superlattices. Even though the chapter maintains a close connection to the original publications that are part of this cumulative thesis, it goes beyond these works by providing a comprehensive overview of the research field of coherent phonon heat conduction. Therefore, the publications, which are part of topic (i), are placed within the larger context of the relevant literature and are discussed considering most recent developments in the field. The chapter concludes once more with an outlook, this time not focused on breakthroughs in experimental methodologies but rather highlighting new physical discoveries of the past 2-3 years, which challenge existing knowledge and preconceptions in phononic nanoscale thermal transport. Parts of the content of chapters 1 to 3 were previously published as separate book chapter [32] (Copyright (2019) from 21st Century Nanoscience – A Handbook: Nanophysics Sourcebook (Volume One), edited by K. D. Sattler, chapter 11 by J. S. Reparaz and M. R. Wagner, reproduced by permission of Taylor and Francis Group, LLC, a division of Informa plc).

Furthermore, chapters 4 and 5 list the publications related to my research on III-

nitride and II-oxide semiconductor nanostructures, respectively. Chapter 4 contains publications in two main parts: The first part targets the investigation of optical phonons and excitons in III-nitride thin films and single crystals. These include the effects of uniaxial and hydrostatic pressure on the optical phonons frequencies, Born's transverse effective charge, and dielectric constant in GaN, AlN, and InN as well as the optical study of doping related charge and energy transfer mechanisms in GaN. The second part adapts the structure of the previous chapter and orders the results by dimensionality of the investigated nanostructures, i.e. 2D quantum well, 1D nanowires and quantum wires, and 0D quantum dots.
Chapter 5 comprises publications related to the phononic and excitonic properties of oxide thin films and nanostructures with particular focus on ZnO. These include the optical, thermal, and functional properties of various ZnO nanostructures including nanospheres, nanocrystals, nanoprisms, and nanowires. The effects of polarity in ZnO and GaN are addressed in a comprehensive review article which covers fundamental and theoretical aspects, growth of epitaxial films and nanostructures, measurement techniques, and devices [31].
The most relevant findings and conclusions derived from the scientific works which are part of this thesis are briefly recapitulated in the summary in chapter 6.

2 Experimental techniques for thermal transport studies

During the last two decades, several novel research methodologies were developed to study thermal transport at the nanoscale. These include contact-free optical techniques based on reflectivity or Raman scattering measurements (section 2.1) as well as contact-based electrical and scanning probe techniques (section 2.2). This chapter aims to give a short and comparative overview of the state-of-the-art of these methodologies highlighting the most suitable experimental approach for samples with different structure and dimensionality. The 3-omega method [33] (section 2.2.1) was developed in the 1990s and sets its place as the most established and accurate technique to study thermal transport in thin films and bulk samples. More recently, contactless techniques received considerable attention due to their experimental versatility and their ability to avoid thermal contact resistances arising from electrical contacts. The most prominent examples are time- and frequency-domain thermoreflectance (TDTR and FDTR) [34, 35] which apply a metallic transducer to monitor a laser induced temperature rise by its temperature-dependent optical reflectivity (section 2.1.2). Raman thermometry [36, 37] in its one and two-laser versions (section 2.1.1) has also proven to be of great value for 2D systems and for suspended thin films (quasi-2D). Lower dimensional systems such as quantum dots (0D) and nanowires (1D) are typically much smaller than the diffraction limit for visible and near UV lasers and therefore require techniques, which provide higher spatial resolution. This can be achieved by e.g. scanning thermal microscopy (SThM) [38] (section 2.2.2), and microchip suspended platforms consisting of a heater and a thermometer (section 2.2.3). Scanning thermal microscopy achieves the highest spatial resolutions since it is based on atomic force microscopy. Finally, the microchip suspended platform approach is specifically suitable for nanowires, 2D and quasi-2D systems, although this approach usually requires a considerable amount of fabri-

cation efforts. The following sections provide a short overview of the operational principle of each of these methodologies including their main advantages and disadvantages in terms of spatial resolution, temperature sensitivity and geometrical requirements. For an in depth discussion, the reader may also refer to the original publications as well as a number of reviews discussing each approach in detail [3, 39–53].

2.1 Optical techniques

2.1.1 Raman thermometry (one- and two-laser version)

Raman thermometry in its conventional one-laser version is a contactless optical technique for which a laser beam is focused onto the surface of a sample and the Raman shift of any Raman active optical mode is monitored as function of the absorbed power. With increasing absorbed power, the laser induced heating results in a lattice expansion of the material which causes an increasing red shift of the Raman mode. Thus, the lattice temperature can be directly determined provided that the spectral position of the selected Raman mode as function of temperature is available for calibration. Such a calibration can be easily obtained by e.g. temperature-dependent low power Raman measurements in a cryostat or heating chamber. The thermal conductivity k of the sample can then be extracted if the absorbed power by the incident laser is known. With the simultaneous knowledge of the local spot temperature, the laser power absorbed by the specimen, and the laser spot size and shape, it is possible to solve the 2D heat equation by using appropriate boundary conditions. This technique can be applied to bulk samples and supported thin films, however, it is for the case of 2D materials and suspended thin films (quasi-2D) where it provides the best results. The main reason is that a quasi-2D geometry considerably simplifies the applied heat flow model as well as the modeling of the laser spot shape, particularly in its depth profile. In a 2D material as well as in suspended thin films, the heat source given by the laser spot can be considered as circular and homogeneous in the out-of-plane direction.
This approach has proven to be of great value for cases where other methodologies are experimentally challenging, e.g., the case of graphene and other 2D materials. Fig. 2.1 displays an example of the successful application of this technique [36]. The systems under investigation are suspended Si thin films with thicknesses between 10 nm and 1000 nm. The thermal conductivity of the thin films decreases with decreasing thickness due to boundary scattering (geometrical phonon scattering) at the surfaces of the suspended films [36]. In order to conduct Raman thermometry measurements in 2D and quasi-2D systems, the following requirements should be fulfilled:

- **Laser absorption:** The systems under investigation must absorb the incident laser light, which results in local heating of the material. Usually, this means that the excitation energy of the heating laser should be larger than the bandgap energy of the material.
- **Raman mode:** The material must exhibit at least one optical phonon mode which is Raman active with a pronounced temperature dependence. Typically, first order Raman modes in conventional semiconductors experience a redshift with increasing temperature. Associated temperature coefficients range between 20 and 65 $\mathrm{K/cm^{-1}}$ [37].
- **Absorbed power:** The absorbed power must be experimentally determined with the highest possible accuracy. A common source of large errors in the determination of k is to rely solely on calculations of the absorbed power based on material composition and dimensions. However, it must be noted that the absorbed power also depends strongly on the local temperature of the laser spot on the sample.
- **Boundary Conditions:** The area of the suspended thin film or 2D material must be large enough to ensure thermal equilibrium at the edges of the sample. Neglect of this condition will result in large errors in the determination of the thermal conductivity of the sample.

Although Raman thermometry based on a one-laser approach is an interesting technique mainly due to its simplicity, its main drawback is that only one point of the temperature field is probed to determine k. This may constitute a major limitation in cases where the boundary conditions cannot be determined a priori since at least two points are required to obtain the temperature field and the thermal conductivity. A prominent example for error-prone Raman thermometry measurements are exfoliated flakes of 2D materials with dimensions in the 10 μm range as the temperature field cannot be expected to decay to the bath temperature over the lateral size of the flakes [15].
Two-laser Raman thermometry (2LRT) [37] is a novel technique developed within the scientific works of this thesis which was successfully applied to study the thermal properties of ultra-thin membranes [37, 54] and 2D phononic crystals [55, 56] (see also section 3.4). It overcomes the previously discussed limitation by introducing a second laser to decouple heating of the sample and probing of the local temperature. While the heating laser with wavelength λ_1 is used to produce a temperature gradient in the sample, an independent probe laser with wavelength λ_2 is used to measure the spatial distribution of the local temperature through the temperature-dependent red-shift of a Raman mode of the sample. The main advantages of this technique as

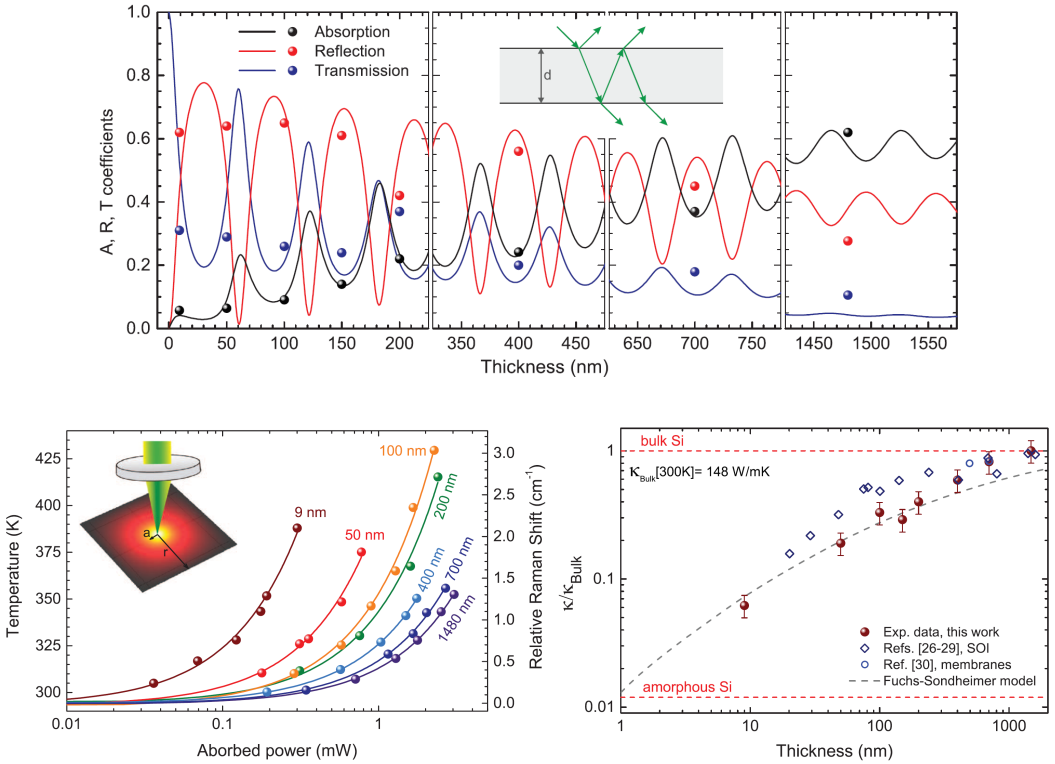

Figure 2.1: (top) Measured absorption, reflection and transmission coefficients as a function of thickness of Si thin films (dots) and corresponding calculations solving the Maxwell equations (lines). (left) Temperature of the spot as function of the absorbed laser power. (right) Thermal conductivity obtained solving the heat equation [36]. (Reprinted from APL Mater. 2, 012113. Copyright (2014) licensed under CC BY 4.0.

compared to other contactless steady state methods such as infrared thermometry is its sub-micron spatial resolution and sensitivity to in-plane thermal transport. Techniques based on scanning probes such as scanning thermal microscopy (SThM), or infrared scanning near-field optical microscopy (IR-SNOM) achieve even higher spatial resolution, however, the difficulties in modeling the thermal response of the tips constitutes a major drawback. On the other hand, short pulse optical techniques such as time domain thermoreflectance (TDTR) or thermal transient grating (TTG) only provide indirect access to k through the thermal diffusivity (α).

We next derive the analytical solution for the temperature field in the case of a free-standing isotropic membrane. A temperature distribution is created upon excitation with a point-like laser source as shown in Fig. 2.2. The solution is simply given by integrating Fourier's equation: $P_{abs}/(2\pi r) = -k\nabla T$, where P_{abs} is the power absorbed by the system, $2\pi rd$ is the cross-sectional area of the heat flux, k is the thermal conductivity, and T is the temperature. Integration of the Fourier's equation

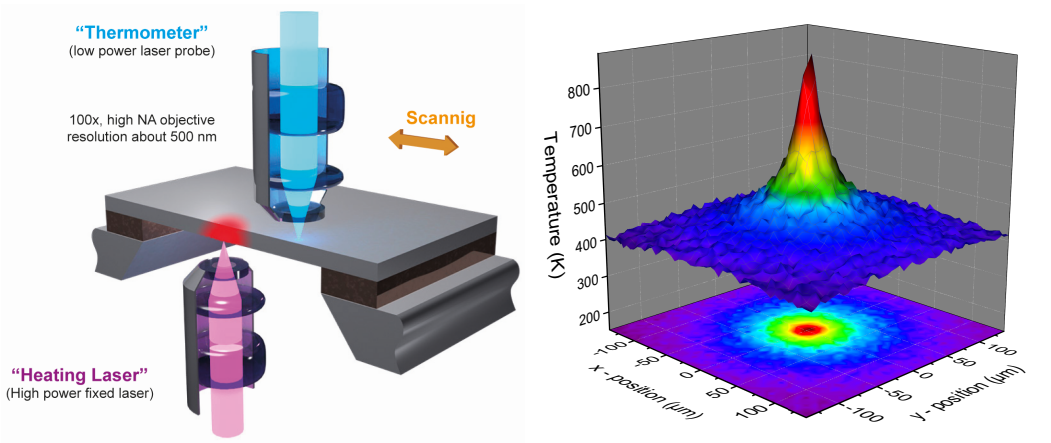

Figure 2.2: a) Schematics of the two-laser Raman thermometry setup consisting of a fixed heating laser and a low power scanning Raman laser. (b) Representative thermal map of a 250 nm thick Si membrane. The projection of the temperature profile onto the bottom plane shows an isotropic temperature distribution. Adapted based on Ref. [37].

leads to the following solutions for the temperature field

$$T(r) = T_0 - \left[\frac{P_{abs}}{2\pi d k_0}\right] ln(r/r_0) \;\; \rightarrow k = k_0 \tag{2.1}$$

$$T(r) = T_0 - \left[\frac{r}{r_0}\right]^{-\frac{P_{abs}}{2\pi d A}} \;\; \rightarrow k(T) = \frac{A}{T} \tag{2.2}$$

for the cases of a temperature-independent thermal conductivity (k_0) and a temperature dependent thermal conductivity $k = A/T$ [37].

Fig. 2.2a displays the schematics of the experimental arrangement. The heating laser with λ_1 is focused onto the lower surface of a membrane, whereas a probe laser with λ_2 is scanned over its upper surface to obtain the local temperature. It should be noted that while relatively high powers are required for the heating laser (λ_1) in order to create a spatially dependent thermal field, low powers are important for the probe laser (λ_2) to avoid an additional thermal perturbation. As a general guideline, a power ratio of at least 10:1 between the heating and probe lasers should be used. Both lasers are focused onto the samples using long distance objectives with numerical aperture NA $\geq$ 0.5. Although these objectives provide lower spatial resolution than short distance objectives (which typically have a NA $\geq$ 0.9), they are required to obtain thermal maps in a controlled environment and under variable temperature conditions in vacuum chambers or micro-cryostats. Especially for thin films with large surface to volume ratio, measurements in vacuum are obligatory to exclude cooling by air convection, a common error source of Raman thermometry

measurements under ambient conditions [56].
Fig. 2.2b displays a 2D temperature map of a 250 nm thick suspended Si film [37]. The maximum temperature of $T \approx 800$ K is reached at the center of the map where the heating and probing lasers are focused onto the same position of the Si membrane. With increasing spatial offset between the two lasers, a thermal decay with radial symmetry is observed in the temperature projection plane. Although this radial symmetry arises from the isotropic nature of Si, it is expected that materials with a directional dependent thermal conductivity (k_{ij}) will exhibit an asymmetric thermal decay. Thus, a major advantage of this technique is its capability to obtain the (anisotropic) temperature dependence of the thermal conductivity in a wide temperature range self-consistently based on the acquisition of a single 2D temperature map [37]. It is interesting to note that the temperature field in Fig. 2.2b does not fully decay to room temperature at a distance of 150μm from the heating laser which is caused by the relatively high thermal conductivity of about 80 $\mathrm{Wm^{-1}K^{-1}}$ for a Si film thickness of 250 nm [36, 37, 54].

2.1.2 Time- and frequency-domain thermoreflectance

Time-domain thermoreflectance (TDTR) [34, 57, 58] and frequency-domain thermoreflectance (FDTR) [35, 59] set their place as versatile all-optical techniques for the measurement of thermal conductivity, heat capacity, and thermal boundary resistance. The contactless nature of both techniques simplifies the measurements and required fabrication steps as compared to other methods such as the 3-omega method (section 2.2.1), scanning thermal microscopy (section 2.2.2), and the microchip suspended platforms (section 2.2.3). TDTR and FDTR are also suitable to study electrically conductive samples, which is usually more complicated using e.g. the 3-omega technique due to the need of an insulating layer that prevents current leakage from the metallic transducer to the sample under investigation. In addition, they provide relatively high spatial resolution near the diffraction limit. In order to present the basic concepts of both techniques, which share the same physical principles but in different domains (time and frequency), we follow the derivation by Cahill [34], and Schmidt et al. [35]. The operational principle of these techniques is based on a two-laser approach similar to a pump-and-probe experiment. Schematic illustrations of common experimental setups for FDTR and TDTR measurements are shown in Fig. 2.3 [35]. A comparatively low power laser, the probe laser, is focused on the surface of the sample (or transducer), whereas a higher power laser, the pump laser, creates a thermal non-equilibrium state. The reflectivity as a function of time (frequency) is probed, leading to a time (frequency) dependent temperature rise in the spot region.
In the case of FDTR, the pump laser is modulated using an electro-optical modulator

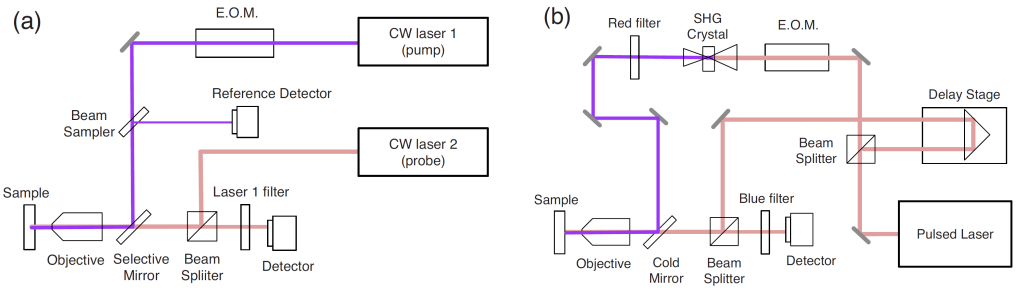

Figure 2.3: (a) Schematics of the FDTR setup based on two continuous wave lasers. The pump laser is modulated using an electro-optical modulator. (b) Schematics of the TDTR setup. A pulsed laser is used as pump and probe laser. The pump laser is frequency doubled to facilitate spectral filtering of pump and probe signals and the probe laser is time delayed by a mechanical delay stage [35]. Reprinted from Rev. Sci. Instrum. 80, 094901 (2009) with the permission of AIP Publishing.

(EOM), acousto-optical modulator (AOM), or simply directly modulating the laser intensity intra-cavity to generate the thermal excitations. Since the pump laser is modulated at a frequency ω_0, the reflectivity of the sample will oscillate with the same frequency. However, due to the finite response time of the sample (or finite thermal diffusivity) the reflectivity oscillations will usually exhibit a different phase than the excitation, i.e., the reflectivity oscillations are retarded with respect to the pump laser. This quantity is named as "phase lag" and can be easily probed by using a secondary laser with a different wavelength (chosen to facilitate spectral filtering of the pump laser). In order to measure this "phase lag" the most convenient approach is to use a lock-in amplifier, which selectively measures the signal at the reference (excitation) frequency, thus, damping the noise arising from other frequencies. Thus, if the intensity of the pump laser is: $I_{pump}\ \alpha\ e^{-i\omega_0 t}$, then the system response at the probe wavelength will be: $I_{pr} = A\ e^{-i(\omega_0 t+\varphi)} = Z(\omega_0)e^{-i\omega_0 t}$, where φ is the "phase lag". The phase of the signal detected by the lock-in amplifier carries the information on the thermal properties of the sample. Two solutions can be derived for a multi-layered system depending on the choice of the probe laser. The phase lag φ can be expressed as:

$$\varphi = \tan^{-1}\left\{\frac{Im\left[Z\left(\omega_0\right)\right]}{Re\left[Z\left(\omega_0\right)\right]}\right\} = \tan^{-1}\left(\frac{V_{out}}{V_{in}}\right) \tag{2.3}$$

where V_{in} and V_{out} are the measured in-phase and out-of-phase signals of the lock-in amplifier at the modulation frequency.

We then obtain for a continuous wave (cw) laser:

$$Z\left(\omega_0\right) = \beta \frac{A_0}{2\pi} \int_0^\infty x \left[\frac{-D(\omega_0)}{C(\omega_0)}\right] \frac{e^{-x^2\left(r_{pump}^2 + r_{probe}^2\right)}}{8} dx \tag{2.4}$$

and for a pulsed laser with repetition rate ω_s and delay between pulses τ:

$$Z\left(\omega_0\right) = \beta \frac{A_0}{2\pi} \sum_{j=-\infty}^{\infty} \left\{ \int_0^\infty x \left[\frac{-D(\omega_0 + j\omega_s)}{C(\omega_0 + j\omega_s)}\right] \frac{e^{-x^2\left(r_{pump}^2 + r_{probe}^2\right)}}{8} dx \right\} e^{-i\omega_s j\tau} \tag{2.5}$$

where β is proportional to the thermal coefficient of the surface, A_0 is the power of the pump laser, r_{pump} and r_{probe} are the radius of the pump and probe lasers, and C and D are coefficients of the transfer matrix, with $C = k_z q \cdot \sinh(qd)$ and $D = \cosh(qd)$. For the coefficients (C and D) the quantity q is given by $q^2 = (k_r x^2 + \rho C_v i\omega)/k_z$, with k_r and k_z being the thermal conductivities in the radial and cross-plane directions, ρ and C_v are the density and specific heat capacity of the material, d is the thickness of the sample, and $\omega = \omega_0$ or $\omega = \omega_0 + j\omega_s$, depending on the probe laser being cw or pulsed, respectively. This approach is very convenient for multilayer structures in which case the transfer matrix of the system is obtained as a product of the individual matrices:

$$M = M_n \ldots M_1 = \begin{pmatrix} A_n & B_n \\ C_n & D_n \end{pmatrix} \ldots \begin{pmatrix} A_1 & B_1 \\ C_1 & D_1 \end{pmatrix} \tag{2.6}$$

Here, M_n accounts for the bottom layer, and M_1 for the top layers where the pump laser is incident. It is valid for the common case that the bottom layer (or the substrate) is in thermal equilibrium, otherwise, additional boundary conditions must be included in the previous set of equations [34, 35]. Finally, the solution for the transient case as required for TDTR is simply a generalization of Eq. (2.5) which is achieved by substituting τ by the temporal variable t. In addition, since usually the lock-in technique is also used to increase the signal-to-noise ratio, the real and imaginary parts of Eq. (2.5) are directly related to the in-phase and out-of-phase components measured by the lock-in amplifier.

Fig. 2.4 displays two typical examples of the data obtained by TDTR (pulsed excitation) and FDTR (cw and pulsed excitation) [52]. The cross-plane thermal conductivity of a GaN substrate is determined using TDTR by comparing the measured ratio signal $R = -V_{in}/V_{out}$ of in-phase (a) and out-of-phase (b) signals with thermal model simulations as function of delay time (c). The dashed lines in Fig. 2.4c indicate ±30% bounds of the best fit resulting in a value of k_z =170 $\mathrm{Wm^{-1}K^{-1}}$. For the case of FDTR, Fig. 2.4(right) displays calculated ratio signals for cw and pulsed measurements of a sapphire substrate with a 100 nm Al transducer [52]. In order to achieve a high accuracy of the determined values, the FDTR measurements should

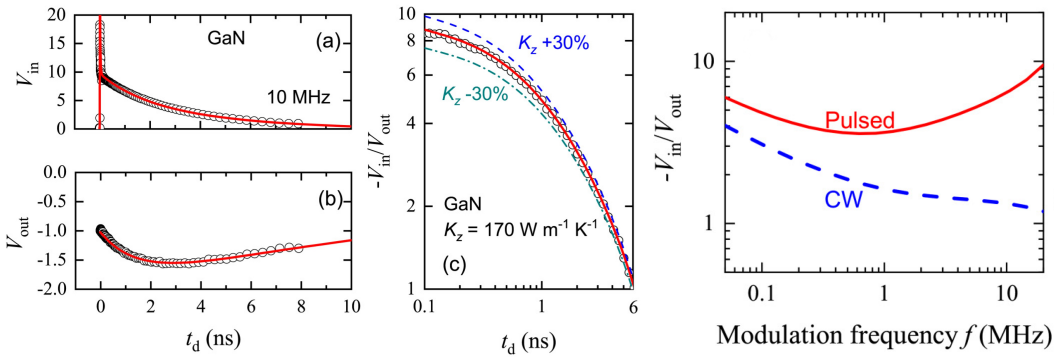

Figure 2.4: (a), (b): In-phase (V_{in}) and out-of-phase (V_{out}) signals measured by TDTR for a GaN substrate with a 100 nm Al transducer as function of delay time. (c): Signal ratio $-V_{in}/V_{out}$ as a function of delay time compared with thermal modeling to extract the thermal conductivity of the GaN substrate. (right): Calculated signals for cw and pulsed FDTR measurements of a sapphire substrate covered with a 100 nm Al transducer over the range 0.05-20 MHz. For the pulsed solution, the delay time is fixed at 100 ps [52]. Reprinted from J. Appl. Phys. 124, 161103 (2018) with the permission of AIP Publishing.

be conducted in a wide frequency range, preferably, scanning up to frequencies of 10 MHz or above. The main characteristics of TDTR and FDTR can be summarized as follows:

- Both techniques are suitable to measure the thermal conductivity, heat capacity, and thermal boundary resistances with rather high accuracy.
- To obtain these quantities it is not necessary to know the power absorbed by the sample in contrast to, for example, Raman thermometry or the 3-omega method.
- Their contactless fashion makes TDTR and FDTR well suited to measure electrically conductive samples, thus, avoiding potential errors arising from current leakage as might occur in the case of the 3-omega method.
- The techniques require minimal sample preparation and they work equally well in ambient conditions as well as in vacuum chambers or cryostats.
- They are currently not suited to measure the thermal conductivity of monolayer or few-layer 2D materials. For these materials, Raman thermometry (in particular in its 2 laser version) or the microchip suspended platform technique are preferable.

2.1.3 Femtosecond pump-probe reflectance spectroscopy by asynchronous optical sampling

The previous sections have focused on optical techniques which provide information about heat transport properties in materials where the phonon population is controlled by the temperature of the system, in other words, no well-defined phase relation exists among phonons. The development of ultrashort laser pulses in the 1980's provided new experimental tools to study the non-equilibrium dynamics of charge carriers and phonons in nanostructures. The optical excitation of materials by ultra-short laser pulses results not only in the formation of excitons and free carriers, their relaxation via scattering with e.g. other excitons, electrons, phonons, impurities or lattice defects, and recombination back to their energetic ground state, but can also introduce the propagating of mechanical waves via acoustic phonons. Of particular interest for the thermal transport in semiconductors are coherent acoustic phonons, i.e. phonons that maintain their phase relation, as they may contribute to coherent phonon heat conduction (see section 3.4).

The propagation of coherent acoustic phonons (CAPs) can be investigated by picosecond / femtosecond opto-acoustics which emerged as experimental technique for the investigation of elastic properties of thin films [60, 61]. In its original form, the technique employs a picosecond pump-probe setup in transient reflectivity configuration. The dynamic response of a material to an initial pump pulse is probed by a second probe laser pulse as function of the delay between the two pulses. The temporal offset between pump and probe pulses is generated by splitting the primary laser into two beams and introducing a time delay between the pulses of both beams by using mirrors on a motorized translation stage (delay line). As the optical pulse duration is short compared to the timescale of thermal expansion, the material's surface experiences a photo-induced stress which is relieved by strain waves consisting of coherent acoustic phonons [62]. The propagation of coherent acoustic phonons in the material and their back-reflection at interfaces or surfaces generates a modulation of the optical properties such as the reflectivity. A time-delayed probe pulse can directly monitor these strain-induced modulations and provide detailed information on elastic and structural properties including e.g. precise measurements of the thickness of buried layers and the roughness of interfaces [63–65].

With the increasing research interest in semiconductors with reduced dimensions, some of the inherent limitations of pump-probe picosecond opto-acoustics became more relevant as compared to the study of e.g. thin films. In particular, these are the beam pointing stability and spot size variation for long time delays due to the large increase of the optical path of one beam as well as the slow acquisition times and limited signal-to-noise ratio in nanostructures with weak optical response.

An elegant solution to overcome these challenges is asynchronous optical sampling

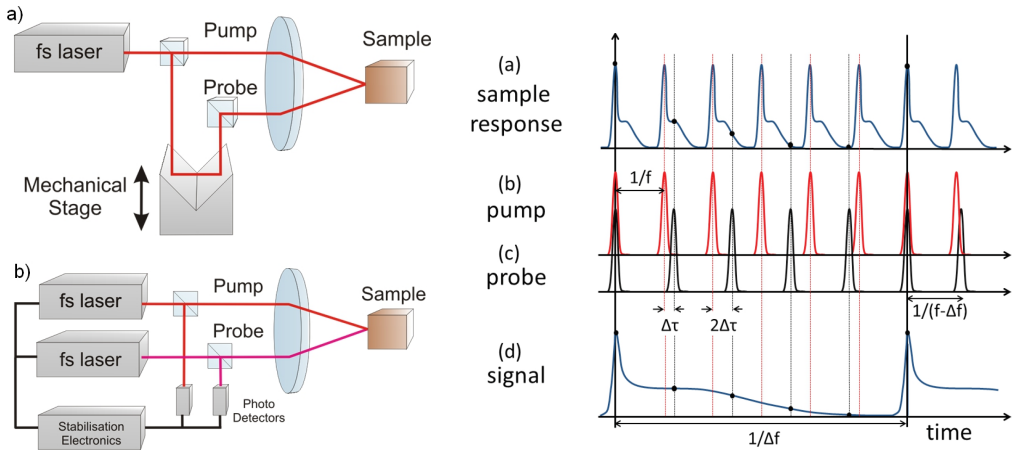

Figure 2.5: (left): a) Schematic illustration of a conventional pump-probe setup with mechanical delay line, b) ASOPS setup consisting of 2 laser oscillators with actively stabilized frequency offset. (right): Illustration of time-domain signal acquisition by ASOPS: (a) sample response to the pump pulse, (b) pump and (c) probe pulses with frequency offset Δf, (d) complete time-domain signal recorded in the time 1/Δf. Reprinted from Ref. [66] with permission of Laser Quantum, Novanta.

(ASOPS) [67], which removes the necessity of a mechanical delay line to introduce the temporal offset between pump and probe pulses (Fig. 2.5a), but instead produces pulses from two actively stabilized laser oscillators with slightly detuned repetition rates (Fig. 2.5b). The dynamic response of the sample (Fig. 2.5(a)) is measured by the continuously varying pump-probe delay due to the frequency offset Δf of the two laser oscillators (Fig. 2.5(b),(c)). While the pump frequency f determines the accessible time window $1/f$, the frequency offset Δf determines the time required to record the dynamical response of the sample $1/\Delta f$ (Fig. 2.5(d)), i.e. a complete transient of 1 ns can be obtained in 100 μs for a typical frequency offset of 10 kHz in a 1 GHz ASOPS. Owing to the high repetition rate of 1 GHz, an excellent signal-to-noise ratio of above 10^7 can be achieved for typical acquisition times in the seconds to minutes range. With the development of dual-GHz femtosecond oscillators [68–70], the combination of ASOPS with picosecond / femtosecond opto-acoustics become a powerful tool for the study of the propagation of coherent acoustic phonons in the GHz [71, 72] to several THz [73] range and thus enabled access to phonons in the frequency range relevant for nanoscale thermal transport [74–76]. Corresponding measurements of CAPs in ultra-thin membranes and phononic crystals which were conducted within the scope of this thesis are discussed in sections 3.2-3.4 [54, 55, 77].

Furthermore, the ASOPS technique has also led to fundamental breakthroughs in

Fourier transform dual-comb spectroscopy [78] and THz time-domain spectroscopy [79–81]. Modern implementations of this technique apply few femtosecond pulse lasers which enable sub-nanometer precision in the measurement of layered structures by photo-acoustic echos. In combination with imaging stages, topography maps of buried layers and their interfaces can be obtained [63, 82]. Despite the advantages of 1 GHz ASOPS setups (short acquisition times, excellent signal/noise ratio) the high pulse repetition rate limits the accessible time window to 1 ns and provides limited spectral resolution for the investigation of low GHz coherent acoustic phonons. To overcome this limitation, ASOPS systems with lower repetition rates (40-80 MHz) are used to increase the frequency resolution at the expanse of a reduced acquisition speed. For example, a 48 MHz ASOPS was employed to image the propagation of surface acoustic waves with picosecond temporal and MHz spectral resolution [82]. In the other direction of the frequency spectrum, an ultrafast 10 GHz ASOPS system with a 100 kHz scan rate was recently developed [83]. As it acquires a full transient in only 10 μs, signal-to-noise ratios exceeding 30 dB can be achieved in the millisecond range. While the repetition rate of 10 GHz limits the accessible time window to 100 ps, few tens of picoseconds are often sufficient for applications such as terahertz time-domain spectroscopy (THz-TDS). Consequently, exciting new experiments including 2D spatial lifetime mapping [84], time resolved spectrocopy in millisecond pulsed magnetic fields with B $>$ 30 Tesla [85], and real-time THz-TDS [86] become possible.

2.2 Electrical and probe techniques

2.2.1 The 3-omega method

The 3-omega technique is based on electrically heating a thin planar metallic resistor with length L, using an AC harmonic current at a frequency ω, and subsequently measuring the resulting voltage drop at the first ($V_{1\omega}$) and third ($V_{3\omega}$) harmonics of the excitation current. The key concept behind this approach is the occurrence of a voltage component at the third harmonic ($V_{3\omega}$) of the excitation current ($I_{1\omega}$), which arises from the convolution of the current oscillating at 1ω, with the resistance of the metallic strip oscillating at 2ω, i.e., heat dissipation on the metallic strip is independent on the sign (or direction) of the excitation current. In simple words, applying an AC current to a thin resistor will increase the temperature of the resistor due to the Joule effect with a magnitude that depends on the thermal conductivity k of the underlying sample. The power dissipated by the harmonic current, $P(t) = V(t)I(t)$, leads to a time-dependent temperature rise of the resistor consisting of a DC part (T_{DC}) which can be related to the root-mean-square (RMS) value of $P(t)$, and an AC part (T_{AC}) which oscillates around T_{DC} at odd harmonics of the

fundamental excitation frequency. The amplitude of the AC oscillations $|T_{AC}|$ can be expressed in terms of the third harmonic of the voltage signal, and through the temperature coefficient of resistance of the resistor, $\beta = (1/R_0)[dR/dT]$, as:

$$|\Delta T_{AC}| = \frac{2V_{3\omega}}{\beta V_{1\omega}} \tag{2.7}$$

where R and R_0 are the resistance of the samples at T and T_0, respectively. The analytic solution to this problem can be approximated solving the heat equation for the case of an infinitely long and narrow heat source (the metallic strip) over a semi-infinite substrate. Following the solution by S. Carslaw and D. G. Jaeger [87], the temperature distribution over the heat source is obtained solving the heat equation as follows:

$$\Delta T = \frac{P_0}{\pi L k} K_0(qr), \tag{2.8}$$

where K_0 is the zeroth-order modified Bessel function, $1/q = (\alpha/i2\omega)^{1/2}$ is the wavelength of the induced thermal wave (or thermal penetration depth), α is the thermal diffusivity of the specimen, ω is the angular frequency, P_0 is the power dissipated in the resistor, and L is the length of the resistor. In the limit of $|qr| \ll 1$, i.e., large thermal penetration depth, the previous equation can be approximated as:

$$\Delta T = \frac{P_0}{\pi L k} \left[A - \frac{1}{2} \log(2\omega) - \frac{i\pi}{4} \right], \tag{2.9}$$

where A is a constant. The magnitude of the power component which drives the AC temperature oscillations is $P_{RMS} = P_0/2$. Half of the power is responsible for a DC temperature rise, the other half drives the temperature oscillations, which are manifested in $V_{3\omega}$. Finally, the thermal conductivity of the sample can be obtained by inserting the measured temperature rise into Eq. 2.9 as all remaining quantities are known.

Up to this point, the discussion applies to the case of semi-infinite substrates. The solution for thin films is rather easy to obtain and was derived by D. G. Cahill [33] already at the beginning of the 1990's. The key idea is to consider that the thin film under investigation behaves like an interface resistance and, thus, contributes to the temperature rise of the heater which itself is frequency-independent. This approximation is expressed by:

$$|\Delta T_{AC}| = |\Delta T_{AC}|_{substrate} + |\Delta T_{AC}|_{TF} \tag{2.10}$$

In order to find the explicit expression for this last term, one considers a thin film on a substrate with a film thickness d and a thermal conductivity k_{TF} which is deposited over a substrate with a thermal conductivity k_s. The resistor on top of the thin film is defined by a width $2b$ and a length L. Applying the 1D form of

Fourier's law along the cross-plane direction, i.e., parallel to the thickness d of the thin film one obtains:

$$\frac{P}{2bL} = -k_{TF}\frac{|\Delta T|_{TF}}{d} \tag{2.11}$$

The previous expression gives the thermal conductivity of the thin film from the measured temperature offset with respect to the reference measurement (substrate). This equation constitutes a valid approximation if the substrate and thin film fulfill the following criteria:

- $2b \gg d$: the physical meaning of this approximation is to ensure that the 1D form of Fourier's law can be applied.
- $1/q = (\alpha/i2\omega)^{1/2} \gg d$: the thermal penetration depth must be large as compared to the thickness of the thin film which implies that the thermal properties of the thin film are frequency-independent. In Eq.(2.9) only the contribution arising from the substrate is frequency-dependent.
- $k_s \geq 10k_{TF}$: this relation comes mostly from experience and ensures that heat flows in the cross-plane direction through the thin film with negligible in-plane contribution.

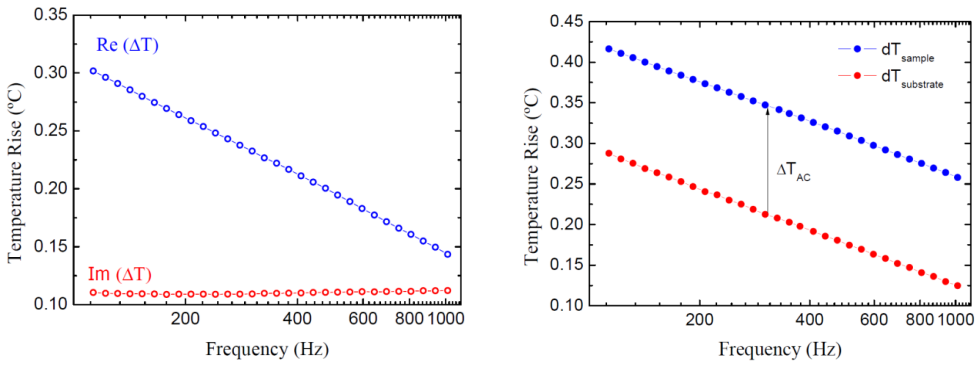

Figure 2.6: a) A typical example of the output obtained from 3-omega measurements in a borosilicate glass (Pyrex 7740) substrate. Data points show the measured temperature rise as function of frequency for the in-phase and out-of-phase signals. b) Temperature rise of the resistor for thin films with respect to the reference substrate for a 200 nm SiO_2/Si thin film. The thermal conductivity is extracted from the temperature offset averaging through the entire frequency range.

Fig. 2.6 shows two examples of data measured using the 3-omega method in a borosilicate glass (Pyrex 7740) substrate (left) as well as for the case of a 200 nm thick SiO_2 thin film deposited over a Si substrate (right). In both cases, the temperature rise in the metallic transducer is plotted as a function of the excitation frequency.

In the bulk case, the real part of the temperature oscillations is fitted using a linear function, whereas for the case of the thin film a reference sample containing only the substrate must be measured. The thermal conductivity is obtained by the temperature offset between the substrate and the thin film plus the substrate. In addition to substrates and thin films, the 3-omega technique can also be applied to multilayered systems [88, 89]. The depth sensitivity is obtained through the frequency response to the voltage third harmonic of the injected current [33]. Within the works of this thesis, the 3-omega method was applied to study the properties of thermal interface materials (TIMs) such as sintered silver pastes [90]. These materials are of high technological relevance as they are commonly used to optimize the thermal contacts between e.g Si microchips or GaN LEDs and metal (Cu, Al) heat sinks [90].

2.2.2 Scanning thermal microscopy

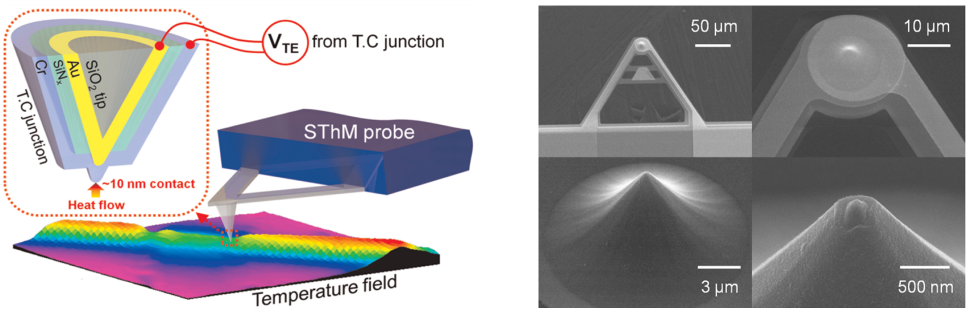

Figure 2.7: (left) Schematic illustration of the scanning thermal microscopy (SThM) technique with a Au-Cr nano thermocouple junction placed at the end of the tip. The heat transfer between the tip and the sample is dominated by solid tip-sample contact whose diameter is in the 10 nm regime. The thermoelectric voltage generated from the Au-Cr junction is directly proportional to the local temperature of the sample at the point contact and enables quantitative temperature measurements. (right) Scanning electron microscope images of the SThM probe with integrated Au-Cr thermocouple at different magnification levels [91]. Reprinted with permission from ACS Nano 6, 4248. Copyright (2012) American Chemical Society.

Scanning thermal microscopy (SThM) is based on scanning probe microscopy previously developed for topography imaging with high spatial resolution. In order to acquire thermal maps, SThM uses a thermocouple junction which is placed inside the tip of a scanning probe microscope (Fig. 2.7 (left)). The corresponding scanning electron microscopy (SEM) images of a thermocouple probe tip are shown at different magnifications in Fig. 2.7 (right). Since the invention of SThM in 1986 [38], the technique was continuously improved regarding spatial resolution and temperature

sensitivity [5, 91–97]. It was successfully applied for the study of thermal properties in semiconductor micro- and nanostructures for microelectronics, optoelectronics, polymer science, and carbon allotropes [41, 50, 98–101]. Modern implementations of SThM that avoid contact related artefacts [100, 102, 103] achieve sub-10 nm spatial and sub-10 mK temperature resolution [91, 97]. While there are a large number of different approaches to probe temperature and create local hotspots using scanning probe microscopy tips, the most common methods are:

- **Thermovoltage-based methods** make us of the thermoelectric voltage generated at the junction between two electrodes. The electrodes can be chosen as the tip-sample interface, or built-in sensors within the tip such as a thermocouple and/or Schottky diodes.
- **Thermoresistive probe methods** are typically based on metallic or Si-doped tips where the temperature coefficient of resistance is the mechanism used to sense the temperature: $R(T) = R_0(1 + \beta\Delta T)$.

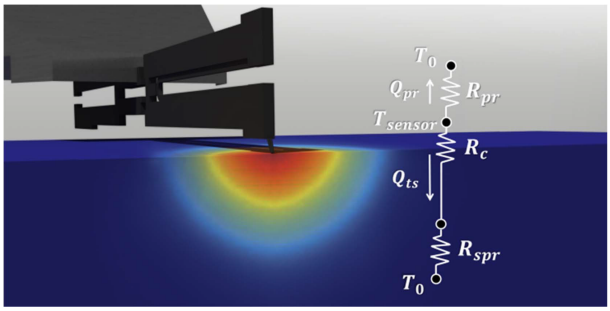

Figure 2.8: Schematic of the nanoscopic tip-sample contact and the corresponding thermal resistance circuit. The quantities represent the thermal resistance of the probe R_{pr}, the thermal contact resistance between the probe and the sample R_c, and the thermal spreading resistance within the sample R_{spr}. Q_{ts} and Q_{pr} are heat fluxes transferred from the probe tip to the sample and to the probe base and T_{sensor} and T_0 are the heater temperature and ambient temperature, respectively [104]. Reprinted from Nanotechnology 28, 505704. Copyright (2017) licensed under CC BY 3.0.

Although SThM is a promising technique in terms of lateral spatial resolution, its main drawback is the data reduction procedure. In order to obtain the local temperature and thermal conductivity, several assumptions must be made to model the conditions at which the experiment is conducted. For example, the influence of air and water (water meniscus), or the detailed geometrical shape of the tip can have substantial influence on the data reduction. Heat transport due to convection

through the surrounding air, heat losses through the tip itself, the influence of contact resistance between the tip and the sample, heat radiation losses, etc., are some of the boundary conditions that must be considered and modeled in order to obtain reliable quantitative thermal data of the specimen [105]. A simplified schematic illustration of the nanoscale tip-sample contact and its thermal resistance circuit is depicted in Fig. 2.8 [104]. These and related problems of tip based thermal measurement techniques are currently stimulating research efforts of several groups around the world. For a more comprehensive discussion of thermal probe techniques, the interested reader is referred to several recent review articles [50, 99–101].

2.2.3 Microchip suspended platforms

Suspended platforms constitute a unique alternative to measure the thermal conductivity of 1D and 2D materials. Typically, these platforms consist of a metallic heater/thermometer deposited over a SiN_x membrane [44, 106]. A gap is intentionally etched in the middle of the suspended membrane, where the sample under investigation is placed. Fig. 2.9 displays two examples of microchip thermal sensing platforms.

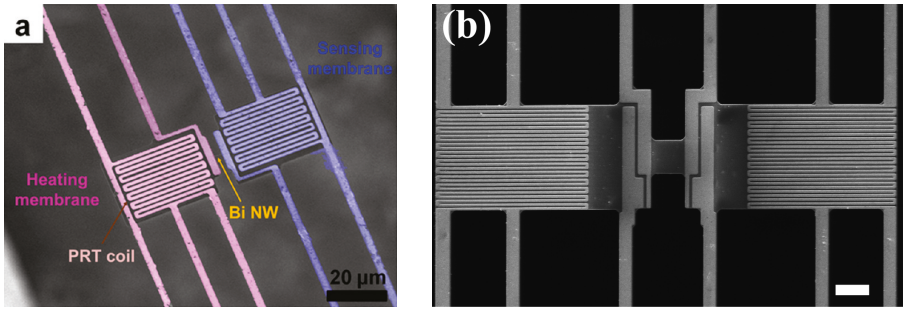

Figure 2.9: (left) Scanning electron microscope image of a suspended platform used to measure a single NW [107]. Reprinted with permission from ACS Nano 5, 3954. Copyright (2011) American Chemical Society. (right) SEM image of a suspended platform to measure a graphene flake [108]. Reprinted with permission from Nano Lett. 11, 113. Copyright (2011) American Chemical Society.

The methodology resembles the steady-state approach based on Fourier's law, i.e., a known heat flux is induced through the nanostructure and the temperature gradient is obtained using the metallic thermometers deposited on each side of the membrane. The resolution of the suspended platform approach in thermal conductance is of the order of 1 nWK^{-1} at room temperature. However, improvements based on a Wheatstone bridge circuit have demonstrated a significant reduction of the noise to values of 10 pWK^{-1} [109]. More recently, the sensitivity of this design was pushed even further with a reported temperature resolution of 50 μK and

0.25 pWK^{-1} thermal conductance resolution [110]. Resistive thermometry using a modulated heat current on a suspended single pad device was also reported which is capable of resolving about 1 pW heat current with a temperature resolution of 10-50 μK [111, 112]. Suspended structures have been used to measure the thermal conductance of a variety of nanostructures such as single- and multi-walled carbon nanotubes [113–115], hexagonal boron nitride [116], graphene [117], black phosphorus nanoribbons [118] as well as Si, SiC, SiGe, Bi, Bi_2Te_3, InAs, PbS, PbSe, PbTe, GaN, and ZnO nanowires [119–125]. This approach, however, is prone to large experimental errors if the thermal leakages within the suspended platform are not carefully taken into account [126]. The reason is that usually only small heat fluxes can be induced through the nanostructures and, thus, heat leakages of any form become relevant. In summary, microchip suspended platforms possess the following characteristics:

- Their design is excellent to study 1D and 2D structures as heat from the heater to the thermometer flows exclusively through the nanostructure, thus avoiding the influence of substrates or interface resistances.
- The temperature and thermal conductance resolution are among the best nanoscale thermal characterization techniques if common error sources such as unknown thermal contact resistance, modifications of the temperature distribution on the platforms (in case of highly conductive samples), and potential radiation losses can be excluded.
- The fabrication process is more demanding compared to other experimental approaches. Expensive equipment and facilities such as clean-rooms are necessary to fabricate the sensing platforms. Depending on the dimensions of the nanostructure under investigation, its placement in between the gap of suspended heating and probing pads may prove challenging.

2.3 Conclusion and perspectives

This chapter has provided an overview of various contact-free and contact-based experimental techniques that represent the state-of-the-art for thermal transport measurements of semiconductor nanostructures. With the exception of frequency-domain thermoreflectance and microchip suspended platforms, all of the discussed techniques were applied for the scientific publications which are part of this cumulative thesis. The choice of the most suitable experimental methodology largely depends on the geometrical aspects of the structure. Contact-free techniques have received particular attention in recent years due to their versatility and intrinsic avoidance of thermal interface contacts. However, each material system, dimension,

and geometry should be evaluated in detail in order to select the most suitable experimental methodology for the study of nanoscale thermal properties.
Apart from the previously discussed techniques, which have achieved a certain level of maturity regarding experimental design, modeling, and distribution in nanoscale characterization labs around the world, novel experimental concepts and techniques are continuously being developed. These developments are stimulated by the continuing miniaturization of semiconductor devices with characteristic transistor dimensions in the few nanometer range, envisioned novel nanophononic applications such as phonon lasers [127, 128], thermal diodes [21], thermal transistors [129], thermal cloaks [22, 25], and guided heat transport [26], as well as the recent discoveries of hydrodynamic transport in graphite [130] and coherent phonon heat conduction in superlattices [131, 132] (see chapter 3). Two selected examples for such novel experimental techniques that have emerged in the past few years are time-resolved magneto-optical Kerr effect thermometry (TR-MOKE) and scanning nanothermometry based on a superconducting quantum interference device placed on a sharp tip (SQUID-on-tip).

Time-resolved magneto-optical Kerr effect thermometry (TR-MOKE)

One of the main limitations of time-domain thermoreflectance measurements arises from the metallic transducer that is typically deposited on the sample in order to ensure a pronounced temperature induced modulation of the probe beam (large thermoreflectance coefficient). The thickness of the transducer needs to be sufficient to be optically opaque (typically $d \geq 50$ nm) as the data analysis in TDTR relies on the fact that changes of the intensity of the probe beam are proportional to changes in the surface temperature of the sample [133]. While this transducer is not a problem for comparably thick samples, it hampers measurements of the thermal conductivity and thermal interface conductance of ultra-thin films and 2D materials. The recently developed TR-MOKE thermometry [133–135] overcomes this limitation by replacing the temperature-dependent intensity of the reflected light as measurement signal by the temperature-dependent polarization rotation of the probe beam. In this case, the linear polarized probe beam can be reflected by a semi-transparent ultra-thin (about 4 nm) ferromagnetic transducer (Co/Pt) that is perpendicular magnetized insight an external magnetic field. The time-dependent polarization rotation is produced by the magneto-optical Kerr effect which follows the temperature dependence of the magnetization [133]. The polarization rotation is detected by splitting the probe beam into orthogonal polarization states using a Wollaston prism and detecting the changes in intensity by a balanced photodetector for any given time delay between pump and probe pulses [135]. Using this approach a significant increase in sensitivity to the conductance of interfaces with low thermal

conductivity materials can be achieved as the thinner transducer minimizes lateral heat flow inside the transducer and improves the sensitivity to lateral heat flow in the sample [133, 135]. Since the time resolution for thermal pump-probe experiments is typically limited by the heat diffusion time through the transducer (about 4 ps for a 5 nm Co/Pt transducer), the reduction of the transducer thickness in TR-MOKE could also provide access to non-equilibrium effects of heat carriers in the time-domain [135, 136].
Furthermore, both TDTR and TR-MOKE can be modified to measure the in-plane thermal conductivity by introducing a spatial offset between the focused spots of pump and probe beam on the sample [137]. Instead of measuring the ratio between in-phase and out-of-phase signal (see 2.1.2), the beam-offset variant of TDTR measures the full-width half maximum (FWHM) of the out-of-phase signal as the pump beam is spatially displaced from the probe beam [138]. This approach enables the determination of the thermal conductivity tensors in anisotropic materials with reduced symmetry. Recently, this beam-offset technique was successfully applied to TR-MOKE thermometry and used to measure the thermal conductivity tensor of MoS_2 [133] and black phosphorous [139].

Scanning nanothermometry based on a superconducting quantum interference device placed on a sharp tip (SQUID-on-tip)

Although the previously discussed techniques provide a diverse set of tools to investigate the thermal properties of nanostructures, they share one common shortcoming: None of them is sensitive enough to study energy dissipation mechanisms in quantum systems. As an example, the dissipated power limit of an ideal qubit operating at $f = 1$ GHz and $T = 4.2$ K as given by Landauer's principle [140] is $P = E_0 f = k_B T \ln 2 f = 40$ fW [141, 142]. Depending on the dimensions of the qubit and the thermal conductivity of the substrate, such a power dissipation will result in a temperature increase in the few μK range, several orders of magnitude below the sensitivity of the discussed techniques. Thus, the thermal study of energy dissipation processes in quantum structures seemed out of reach with the existing experimental tools. Recently, Halbertal et al., have overcome this limitation by developing a nanothermometry system capable of contact-free thermal imaging at cryogenic temperatures with sub-μK sensitivity [143]. The technique is based on a superconducting quantum interference devices (SQUID) consisting of a single Pb superconducting junction that is placed on a sharp quartz pipette of a scanning microscope operating at cryogenic temperatures. It is capable of thermal imaging with a nanometer spatial resolution in combination with a remarkable temperature sensitivity limited by a thermal noise level of 440 nK. Using this technique, Halbertal et al., were able to observe energy dissipation changes due to single-electron charging

of individual quantum dots in carbon nanotubes [143] and phonon emission from individual atomic-scale defects in graphene [144].
These examples demonstrate the currently highly dynamic state of the research field of experimental nanoscale thermal transport. It can be expected that existing nanoscale characterization techniques will be further refined and improved in the coming years in order to provide the experimental tools to study thermal properties of individual quantum structures and transport dynamics of thermal phonons with comparable spatial and temperature resolution and sensitivity as already achieved in the cases of photons and electrons in nanophotonics and nanoelectronics.

3 Thermal transport in nanostructures

This chapter discusses the effects of geometry and artificial periodicity on the thermal properties of materials with reduced dimensionality. The text focuses on non-metallic nanostructures where phonons constitute the main particles responsible for thermal transport and heat propagation. The first sections summarize the most common phonon scattering mechanisms that influence the thermal conductivity (section 3.1) and discuss the effects of phonon confinement on the phonon dispersion relation and phase velocities in semiconductor nanostructures (section 3.2). The modification of the thermal conductivity and phonon dispersion relation in materials with reduced dimensions is closely related to the alteration of phonon lifetimes. Consequently, section 3.3 focuses on the dynamics of coherent acoustic phonons in nanostructures.
Following these fundamental aspects of thermal properties of semiconductor nanostructures, the subsequent discussion targets recent advances in the study of coherent on non-coherent phonon heat conduction in materials with reduced dimensionality (section 3.4). These include thin films and quasi-2D membranes (section 3.4.1), nanostructures with second-order periodicity such as two-dimensional phononic crystals and superlattices (sections 3.4.2 and 3.4.3), nanowires (section 3.4.4) and quantum dots (section 3.4.5). The chapter highlights works that are part of this cumulative thesis in conjunction with recent progress in the understanding and control of phonon mediated heat propagation within the last decade. For a more general discussion including earlier developments, the reader may consult a variety of comprehensive reviews on nanoscale thermal transport and phononic crystals [3, 40, 42, 46, 47, 145–152].

3.1 Thermal conductivity modification at the nanoscale

The continuous reduction of dimensions during the last decades has opened the window to manipulate phononic and photonic properties at the micro- and nanoscale. With decreasing dimensions, the presence of heat in the form of atomic vibrations can drastically modify material properties and, in some cases, even structurally change nanomaterials as e.g. in the case of phase change materials [7]. This fact constitutes a major challenge for the design of nanoscale devices due to the complexity of controlling heat flow at the nanoscale. One of the main reasons lies within the diverse frequency spectrum of phonons that generally consists of many different possible vibrations (modes) depending on the symmetry of the atomic lattice. Furthermore, phonons experience anharmonic decay which complicates the control of their individual propagation as they convert to lower frequency phonons through *Normal* and *Umklapp* scattering within short timescales. Thus, two key questions which summarize the importance of this topic are:

- Which are the leading mechanisms that influence thermal transport at the nanoscale?
- To what extent can we control these mechanisms in order to influence nanoscale heat transport?

Nanoscale heat transport is rather complex to fully address due to the large number of different scattering processes and interactions involved. However, we can divide phonon-related thermal processes into two main categories with fundamentally different physical origin. These are non-coherent particle-like and coherent wave-like processes that arise from the particle/wave duality of phonons. While most of the modifications of thermal conductivity in nanostructures can be explained by non-coherent processes, wave-like phonon heat conduction is a more elusive phenomenon that only recently attracted increased research attention. In order to explain the modification of thermal properties in semiconductor nanostructures by non-coherent processes, we need to consider the different scattering processes that heat-carrying phonons can undergo. These are:

- **Normal scattering** N**:** Phonon-phonon scattering for small wave-vector phonons is a non-resistive scattering mechanism that conserves momentum and does not affect the propagation of heat.
- **Umklapp scattering** U**:** Phonon-phonon scattering for large wave-vector phonons results in a sum moment outside of the first Brillouin zone. The resulting phonon momentum is not conserved as Umklapp processes transfer

momentum to the crystal leading to resistive scattering that degrades the heat current.

- **Boundary scattering B:** Scattering of phonons at boundaries such as surfaces, interfaces, or domain walls is usually diffusive and increases thermal resistivity. Specular (non-diffusive) phonon reflection at boundaries can occur when the roughness of the surface or interface is very small compared to the wavelength of the phonons.
- **Defect scattering D:** Scattering of phonons at intrinsic point defects such as vacancies, interstitials, or substitutionals, which disturb the periodic lattice potential.
- **Impurity scattering M:** Scattering of phonons at chemical elements which are not intrinsic to the crystal lattice (low concentration).
- **Alloy scattering A:** Scattering of phonons due to the introduction of chemical elements at higher concentrations that form an alloy. The distribution of the alloying element within the lattice determines the disorder degree and affects the phonon scattering rates.
- **Isotope scattering I:** Scattering of phonons due to the mass difference between different isotopes of a chemical element.
- **Free carrier scattering C:** Scattering of phonons with free carries such as electrons, holes, and excitons.

Except for Normal scattering (and specular-reflected phonons at boundaries), all other listed phonon scattering processes are resistive since they limit the average distance that a phonon can travel in a material without collision (phonon mean free path Λ). Within the kinetic theory, the thermal conductivity is given by

$$k = \frac{1}{3}\sum_{ij} C_{ij} v_{ij} \Lambda_{ik}, \tag{3.1}$$

where C is the specific heat capacity, v is the phonon group velocity and Λ is the phonon mean free path with summation over all phonon modes i and phonon branches j of the phonon spectrum contributing to k. The phonon mean free path Λ is determined by the product of phonon velocity v and phonon lifetime τ with

$$\Lambda_{ij} = v_{ij}\tau_{ij}. \tag{3.2}$$

The total scattering rate $1/\tau_{total}$ can be expressed by Matthiessen's rule as:

$$\frac{1}{\tau_{total}} = \frac{1}{\tau_N} + \frac{1}{\tau_U} + \frac{1}{\tau_B} + \frac{1}{\tau_D} + \frac{1}{\tau_M} + \frac{1}{\tau_A} + \frac{1}{\tau_I} + \frac{1}{\tau_C} + ... \tag{3.3}$$

Thus, an increase of the phonon scattering rate at e.g. boundaries of nanostructures with smaller dimensions ($1/\tau_B$) will results in a reduced thermal conductivity of the material as expressed by Eqs. 3.1 - 3.3.
In contrast to these incoherent processes, coherent scattering arises from the wave nature of phonons which results in the modification of the phonon dispersion relation and formation of phononic bandgaps, and influences the coupling between different phonon branches, phonon group velocities, and phonon lifetimes. Typical examples of these cases are phononic metamaterials, i.e. materials with an artificial second-order periodicity such as phononic crystals (section 3.4.2) and superlattices (section 3.4.3) in which acoustic and thermal properties can be tailored by appropriate choice of materials, lattice symmetry, dimensions, and periodicity [153]. While incoherent scattering can rather easily be introduced and tuned using the previously described mechanisms to increase or decrease phonon scattering, the field of coherent heat manipulation is still in an early development stage, mainly due to the stringent conditions on surface roughness and periodicity in order to achieve phonon wave interference [154].

3.2 Phonon confinement

The quantum confinement of electrons and photons is a well-known phenomenon that occurs when structures exhibit a contrast of a relevant material property that limits the propagation of these particles in at least one spatial dimension. In the case of electrons (and holes) typical examples are semiconductor quantum wells and quantum dots where spatial confinement leads to a modification or discretization of the electronic density of states and a corresponding shift of absorption and emission lines. With the discovery of photonic crystals [155, 156], confinement of photons was exploited to achieve e.g. directional control of photon emission, to increase extraction efficiency, or to inhibit spontaneous light emission in these structures [157–159]. In a similar way, confinement of phonons results in a pronounced modification of the phonon dispersion relation and density of states and can be used to generate phononic bandgaps in which phonon propagation is prohibited (section 3.4.2).
Free-standing ultra-thin Si films are ideal examples to study the 1-dimensional confinement of phonons. Being unsupported, a quasi two-dimensional geometry is achieved that enables studies free from the effects of a substrate. The acoustic mismatch with the surrounding air (or vacuum) leads to a confinement of the mechanical energy of the elastic waves supported by the system. The propagation of acoustic waves is often described within the elastic continuum theory, which is usually valid provided the wavelength of elastic waves is significantly larger than the atomic lattice constant.

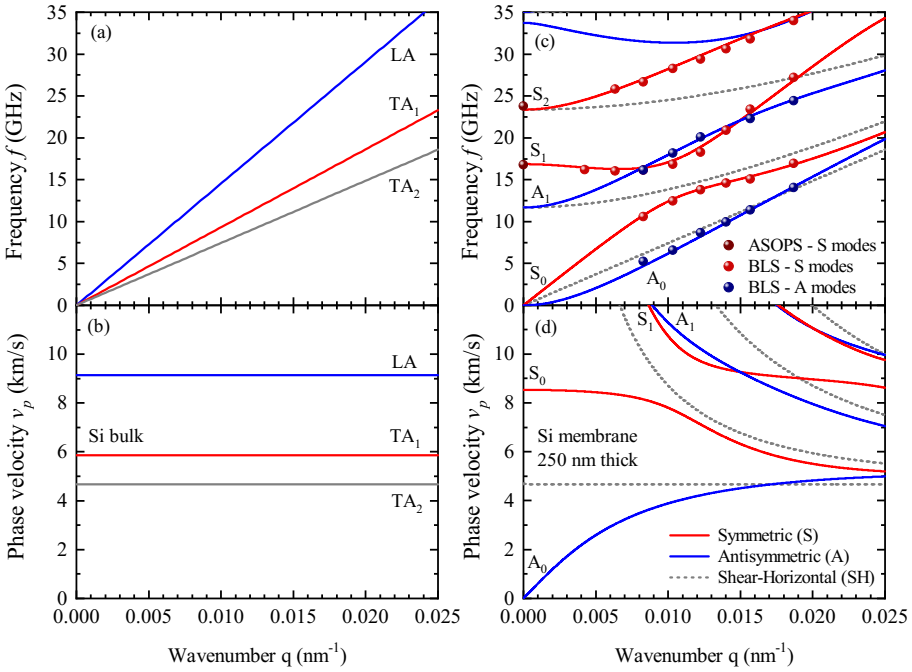

Figure 3.1: Phonon dispersion relation (a),(c) and phase velocity (b),(d) of acoustic phonons in bulk silicon and in a 250 nm thick Si (001) membrane in [110] direction, respectively. Lines indicate LA (blue), TA_1 (red), and TA_2 (grey) phonon modes in bulk Si and antisymmetric (blue), symmetric (red) and shear horizontal (grey) modes in the membrane. Red and blue data points represent measurements of S and A phonon frequencies by angular resolved Brillouin light scattering spectroscopy (BLS). Dark red data points indicate measured phonon frequencies of symmetric S_1 and S_2 Γ-point phonon modes by femtosecond pump-probe reflectance spectroscopy based on asynchronous optical sampling (ASOPS) (section 2.1.3). Adapted based on [53, 55, 160].

The acoustic phonon dispersion relation of bulk Si and of a 250 nm thick Si (001) membrane are displayed in Fig. 3.1a and Fig. 3.1c, respectively. The dispersion relation is shown in [110] direction for small wavenumbers near the center of the Brillouin zone. For bulk Si, the well-known LA, TA_1, and TA_2 acoustic phonon modes are observed in decreasing order of their phase velocity (Fig. 3.1b). In the case of the 250 nm thick Si membrane, the spatial confinement in one dimension gives rise to three types of acoustic waves that are classified by their displacement relative to the mid-plane of the membrane: antisymmetric (A) or flexural (F) waves (blue), symmetric (S) or dilatation (D) waves (red), and shear-horizontal (SH) waves (gray). Apart from the 0^{th} order of these modes which have vanishing energy at the center of the Brillouin zone, the breaking of the spatial continuity results in the appearance

of higher-order modes [160]. For example, in the case of the displayed 250 nm thick silicon membrane, the first-order symmetric (dilational) mode S_1 (D_1) is observed at 16.8 GHz. The experimental determination of the mode frequency is achieved by femtosecond time-domain reflectance spectroscopy using a 1 GHz ASOPS setup (see sections 2.1.3 and 3.3 for details about the technique and physical mechanisms, respectively) [55]. In the applied normal incidence geometry, this method is only sensitive to modes with non-zero out-of-plane displacement at the center of the Brillouin zone. This condition applies for odd-order symmetric Γ-point phonons such as S_1, S_3, S_5 [161, 162]. The data points at non-zero wave-vector originate from angular resolved Brillouin light scattering (BLS) spectroscopy, directly probing the modification of the acoustic phonon dispersion relation by 1-dimensional spatial confinement in quasi 2D membranes [160]. Fig. 3.1d displays the phase velocities of the different modes in the membrane. A strong reduction in the phase velocity occurs for the fundamental (zero-order) antisymmetric A_0 mode [53]. In the case of an 8 nm thin Si membrane, its velocity decreases to 300 m/s [163]. By contrast, the velocity converges to the surface wave velocity in the [110] direction of bulk silicon of 5085 m/s for thicker membranes.

The discussion in this section has demonstrated that phonon confinement in membranes constitutes a path to tailor the phonon dispersion relation, with the membrane dimensions as tuning parameter [163, 164]. Furthermore, the phonon dispersion relation can also be modified by strain, thus, fabrication of strained membranes offers an additional degree of freedom to tailor the phonon propagation [165]. In the larger context of this chapter, it should be noted, that thermal transport properties will only experience a significant influence by phonon confinement if the material dimensions are comparable to the wavelength of thermal phonons. As most of the heat is transported by phonons in the low THz range [153], the dimensions for which confinement of thermal phonons becomes relevant are in the sub-10 nm regime. Consequently, the reduction of the thermal conductivity of Si membranes with thickness below 1 μm (section 3.4.1) cannot be attributed to phonon confinement - as it will affect only phonons in the low GHz frequency range - but rather to the reduction in the phonon mean free path by boundary scattering (section 3.1) [36, 37, 54]. On the other hand, periodic structures, such as phononic crystals, superlattices, or multi-quantum wells can experience significant modifications of thermal transport properties by phonon wave interference effects as discussed in sections 3.4.2 and 3.4.3.

3.3 Coherent acoustic phonon dynamics

Apart from the previously discussed reduction of thermal conductivity by phonon boundary scattering (section 3.1) and the modification of the phonon dispersion relation by phonon confinement (section 3.2), the lifetime of coherent acoustic phonons (CAP) also shows a pronounced size dependence at the nanoscale. While there are extensive works on the optical phonon lifetimes and electron-phonon coupling dynamics in bulk and epitaxial semiconductors, coherent acoustic phonon lifetimes in nanostructures are among the least well-known quantities. Even in the technologically relevant case of Si, measurements of acoustic phonon lifetimes are scarce [76, 161, 166]. In contrast to optical phonons, coherent acoustic phonons can be used to study the elastic properties of nanostructures and interfaces since their group velocity is non-zero. Thus, they can propagate inside micro- and nanostructures and provide information on e.g. anisotropic or size dependent phonon velocities in nanostructures [167–170].

Fig. 3.2a displays femtosecond pump-probe reflectivity spectra of Si membranes with three different thicknesses measured by the asynchronous optical sampling technique (section 2.1.3) [55, 70, 71, 161]. The fast initial change in reflectivity represents the electronic response of the material induced by the excitation and relaxation of free carriers. The subsequent weaker oscillations (blue shaded area) are caused by coherent acoustic phonons. The optical excitation of coherent acoustic vibrations arises from the electronic and thermal stresses (σ_{DP} and σ_T) induced by the pump pulse which are caused by the generated electron-hole pair density and the temperature-induced lattice deformation, respectively [61, 161, 171]. After the fast relaxation of free carriers, the total stress is given by

$$\sigma = \sigma_{DP} + \sigma_T = -B\frac{\partial E_g}{\partial P}N - 3B\beta\Delta T, \tag{3.4}$$

where B is the bulk modulus, E_g is the band gap energy, P is the hydrostatic pressure, N is the generated electron-hole pair density, β is the linear thermal expansion coefficient, and ΔT is the difference in lattice temperature. The first term describes the electronic stress due by the hydrostatic deformation potential and the second term corresponds to the thermal stress due to the temperature rise and the subsequent lattice deformation [161, 171]. For the case of Si, the electronic stress is found to dominate over the thermal stress with $\sigma_{DP}/\sigma_T \approx -7.4$ [161]. The so excited out-of-plane (dilatational) oscillations change the optical cavity thickness of the membranes which leads to a modulation of the probed reflectivity by the Fabry-Perot effect [76, 161, 162]. The time-domain spectra of the relative change in reflectivity in Fig. 3.2a can be fitted by a combination of damped harmonic oscillators

$$\frac{\Delta R}{R}(t) = \sum_n A_n \sin(\omega_n t)\exp(\frac{-t}{\tau_n}) \tag{3.5}$$

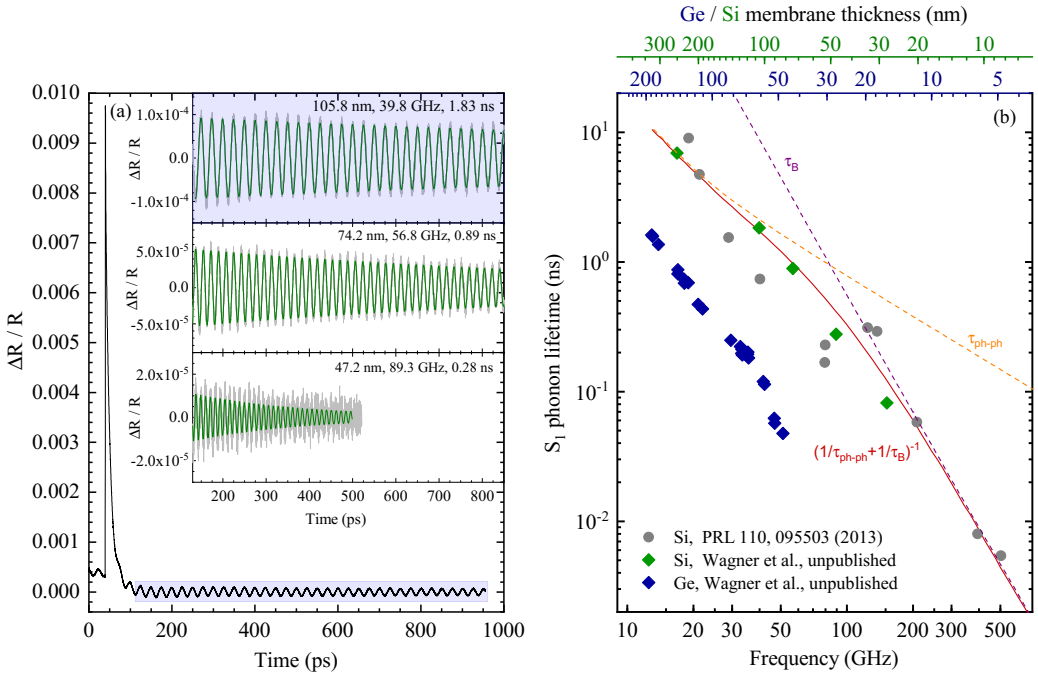

Figure 3.2: (a) Relative change of reflectivity ΔR/R for a Si membrane with a thickness of 105.8 nm as function of time delay between pump and probe. Insets: Close-ups of coherent acoustic phonon oscillations for three different Si membranes with thicknesses of 105.8 nm, 74.2 nm, and 47.2 nm (from top to bottom). (b) Coherent acoustic phonon lifetimes of the first-order symmetric (dilatational) mode S_1 (D_1) as function of frequency (bottom scale) and membrane thickness (top scale). Green diamonds are obtained from measurements shown in (a), gray spheres are values published in Ref. [76], dark blue diamonds are obtained by measurements of suspended Ge membranes with thicknesses between 200 nm and 50 nm. Adapted based on [55, 76, 77] and unpublished data.

where A is the mode amplitude, ω is the mode frequency and τ is the corresponding phonon lifetime with summation n over all symmetric modes S_n. The frequencies spectrum of the CAP modes can be derived from the time-domain spectra by numerical Fourier transformation. Using this approach, one can directly obtain the complete zone-center ($q = 0$) coherent phonon spectrum from the low GHz up to the THz regime [55]. While the time-domain reflectivity spectra contain information on all coherent optical phonons that have non-vanishing out of plane propagation vectors, the largest amplitude is given by the first-order dilatational mode S_1 (c.f. Fig. 3.1). In addition, higher-order modes up to the 19ths harmonic of the first-order symmetric (S_1) mode were observed in Si membranes [161]. The different harmonics in the vibrational spectrum appear as equidistant peaks as a consequence of the confinement of the acoustic modes [161, 172, 173]. The amplitude of the higher-order

odd symmetric modes decreases with $1/\omega^2$ [55]. The absence of even harmonics can be understood taking into account that those modes have only in-plane displacement at the Γ point so that no modulation of the optical cavity thickness occurs [162]. Using the value of the longitudinal sound velocity for Si [001] of $v_L = 8433$ m/s [174], the initial thickness of the membrane d_0 determines the frequencies of the observed modes $\omega_n = n\pi v_L/d_0$ [161]. Apart from the mode frequencies, the time-domain spectra in Fig. 3.2 provide direct access to the coherent acoustic phonon lifetimes τ_n. For a complex frequency spectrum with higher harmonics, the phonon lifetime of the CAPs can exhibit a strong frequency dependent damping where higher-order modes decay faster then the fundamental S_1 mode [162, 175].

For the study of size effects on the CAP lifetimes, it proves practical to focus on the most intense fundamental S_1 mode and omit the higher harmonics. In this case, Eq. 3.5 takes the simplified form: $\Delta R/R(t) = A\sin(\omega t)\exp(-t/\tau)$. Fig. 3.2b displays the measured lifetimes τ of the S_1 coherent acoustic phonons as function of their frequency for Si and Ge membranes with thicknesses between 8 nm and 250 nm. The two different top axis reflects the difference in the longitudinal sound velocity between Si and Ge as all data points are shown as function of the same frequency axis. With decreasing thickness of the membranes, one observes an increase in the measured frequency and simultaneous reduction in the coherent acoustic phonon lifetime. Within the displayed frequency range, the CAP lifetime is reduced by several orders of magnitude. In combination with theoretical modeling of the intrinsic phonon-phonon and extrinsic phonon-boundary scattering rates, the measured frequency dependent CAP lifetimes provide information about the dominating phonon scattering mechanism (section 3.1). The red curve is fitted to the experimental data of the Si membranes with $\tau(\omega) = (1/\tau_{ph-ph}(\omega)+1/\tau_B(\omega))^{-1}$. It shows that boundary scattering dominates for high frequency phonons in ultra-thin structures, whereas phonon lifetimes in thicker membranes are dominated by Normal phonon-phonon scattering processes. In general, intrinsic phonon lifetimes are modeled either by the Landau-Rumer model [176] or the modified Akhieser model [177], which consider the thickness-dependent modification of the thermal conductivity of the membranes [36, 37, 54]. The surface scattering is included using Ziman's wavelength-dependent specularity parameter [178]. The combination of these empirical models was found to describe the trend of phonon lifetimes well over several orders of magnitude, varying from being dominated by intrinsic effects for thicker membranes to being limited by surface roughness for thinner membranes [53, 76].

3.4 Coherent and non-coherent phonon heat conduction

3.4.1 Thin films and membranes

Many studies of the fundamental aspects of thermal transport in semiconductors with reduced dimensionality are based on Si supported and free standing thin films. The maturity of Si technology allows for the production of nominally undoped, defect-free, free-standing, ultra-thin films (membranes). These membranes come close to ideal text-book examples to demonstrate how the reduction of dimensionality from 3D to quasi-2D, i. e. confinement in 1 dimension, results in the modification of the phonon dispersion relation (see also section 3.2) and leads to phonon boundary scattering resulting in a substantial reduction of the thermal conductivity (section 3.1). One possible application of nanostructured crystalline Si thin films are their use in thermoelectric devices [13, 179]. In order to achieve this goal a rather large reduction (at least 2 orders of magnitude) of the thermal conductivity is desirable due to its large value of about 148 $Wm^{-1}K^{-1}$ for bulk Si at room temperature [180]. Pioneering studies of supported Si thin films have revealed clear size effects of the thermal conductivity, i.e., the in- plane and cross-plane components of k were found to decrease as function of film thickness [181–183]. These results were later confirmed by extensive studies based on contactless methodologies such as Raman thermometry in its one-laser [36, 184] and two-laser version [37, 56], time- and frequency-domain thermoreflectance (TDTR and FDTR) [34, 35] and transient thermal grating (TTG) [185, 186].

The origin of the thickness dependent thermal conductivity reduction in supported and suspended thin films is the boundary scattering of phonons at the surface of the films. In other words, the thickness of the films sets an upper limit for the mean free path of thermal phonons Λ_{th}. Thus, if phonons with mean free path larger than the thickness of the samples are present, these phonons will experience mostly diffusive scattering at the surface resulting in a reduction of the thermal conductivity as compared to its bulk value. Fig. 3.3 displays a summary of published data of the thickness dependent thermal conductivity of Si membranes using electrical and optical techniques [54]. Apparently, a large reduction of k occurs as the thickness of the thin films is reduced. In addition, the data shows that the roughness and chemical conformation of the surface becomes important when approaching film thicknesses below about 50 nm [54]. In particular for very thin films of about 10 nm, the presence of the native SiO_2 reduces the thermal conductivity by approximately a factor of 2 as compared to pure Si suspended films of equal thickness (see open diamonds in Fig. 3.3) [54]. An additional reduction of k for rough surfaces as compared to ideally smooth ones is predicted by molecular dynamics simulations and measured by two laser Raman thermometry (Fig. 3.3) [54]. These effects must be considered

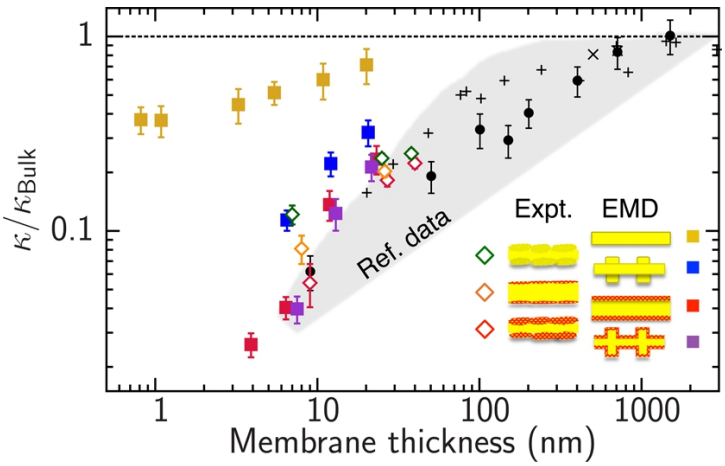

Figure 3.3: Normalized computed and measured thermal conductivities (k/k_{Bulk}) of silicon membranes at T = 300 K as a function of membrane thickness. The filled squares represent results from equilibrium molecular dynamics simulations computed for smooth crystalline (orange), rough crystalline (blue), oxidized (red), and rough oxidized (violet) silicon membranes. The experimental data (open diamonds) are obtained using two-laser Raman thermometry (section 2.1.1). Red diamonds and green diamonds represent membranes with a native oxide layer and HF-etched membranes, respectively. The orange diamonds represent membranes with 6 h oxidation after etching [54]. Reprinted with permission from ACS Nano 9, 3820. Copyright (2015) American Chemical Society.

also in periodic structures such as phononic crystals since they can play a significant role in the modification of the thermal conductivity and might complicate the differentiation between non-coherent and coherent phonon effects.

The main effect of roughness and surface oxidation is to drastically shift the accumulation functions toward shorter phonon MFPs, or, in other words, to largely obstruct the propagation of phonons with long mean free paths and, consequently, their contribution to the thermal conductivity. Fig. 3.4 shows that 50% of the thermal conductivity is contributed by phonons with MFPs up to 160 nm in the smooth crystalline silicon membrane, while the same fraction is contributed by phonons with MFPs up to 15 nm in the rough oxidized membrane [54]. Surface oxidation (red squares) and roughness (without oxidation, blue squares) lead to rather similar accumulation functions, while the combination of the two (violet squares) shifts the accumulation function toward even shorter phonon mean free paths. While the phonon mean free paths in the Si membranes with ideally reconstructed surfaces remain fairly long (>1000 nm), phonons with mean free paths shorter than 100 nm contribute roughly 90% of the total thermal conductivity in ultra-thin membranes (7 nm) with rough native oxide layers.

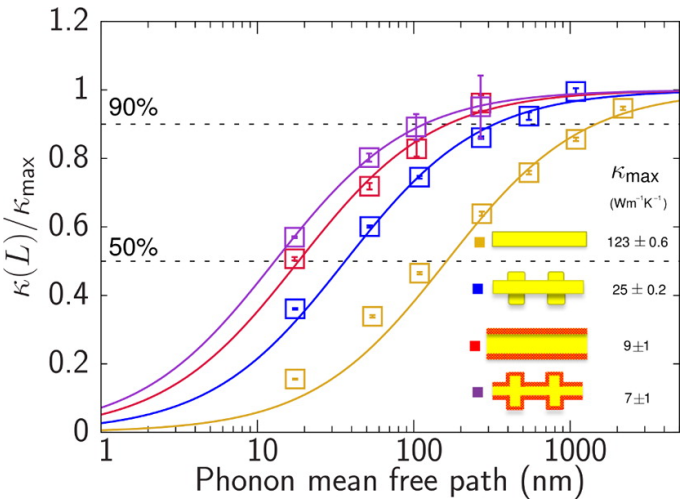

Figure 3.4: Thermal conductivity accumulation functions in free-standing silicon membranes as a function of phonon mean free paths (MFP). The orange, blue, red, and violet squares represent an atomically smooth silicon membrane, a rough (1 nm) membrane, a smooth oxidized membrane, and a rough oxidized membrane with a thickness of 7 nm, respectively. The solid lines are obtained utilizing the size dependence of thermal conductivities computed using non-equilibrium molecular dynamics (NEMD) [54]. Reprinted with permission from ACS Nano 9, 3820. Copyright (2015) American Chemical Society.

Apart from Si, various other semiconductors can be used to fabricated sub-micrometer thin membranes including GaAs, GaN, SiC, SiN, Ga2O3, Ge, and diamond [187, 188] However, only very few works in e.g. Ge [77, 189], poly-crystalline diamond [190–192], and amorphous SiN [190] address also phononic properties (acoustic and thermal) in these membranes. As the ultimate limit of confinement in 1 dimension, 2D materials constitute the obvious choice to study the fundamental aspects of thermal transport in nanostructures. In particular, the recently developed experimental method of 2 laser Raman thermometry (section 2.1.1 and Refs. [37, 55, 56]) is ideally suited for the study of the thermal properties of 2D materials and their heterostructures since it is a contact-free all-optical technique and, in contrast to other techniques neither requires the deposition of a metallic transducer (TDTR, FDTR) nor nanofabrication facilities (microchip suspended platform). For an overview of the extensive literature on thermal properties in 2D materials, the interested reader may refer to a variety of recent review articles on graphene [193–198] as well as other 2D materials [150, 199–202].

3.4.2 Phononic crystals

Phononic crystals constitute an attractive class of material structures with the potential to control and manipulate the propagation of thermal energy. Comparable to photonic crystals [155, 156], the introduction of a second-order periodicity which fulfills the Bragg condition ($n\lambda \sim 2a$) results in a modification of the phonon dispersion relation and the formation of phononic bandgaps where the phonon density of states is zero and the propagation of mechanical waves is prohibited in the phononic crystal structure (see Fig. 3.5). The reason for the formation of these bandgaps lies within the wave interference of phonons in periodic structures and was comprehensively summarized by Maldovan [154]. An early demonstration of such a phononic bandgap was realized in an artistic sculpture consisting of periodically arranged steel cylinders, which result in a strong attenuation of certain sound frequencies in the low kHz range [203]. Since then, the continuing progress in miniaturization and nanofabrication has pushed the accessible frequencies for the formation of phononic bandgaps from a few kHz to the edge of the THz domain, thus allowing not only the modification of the propagation of sound (kHz), ultrasound (MHz), and hypersound (GHz), but also opening the prospect to control the propagation of heat [153]. This development has paved the way towards the realization of novel thermal applications and devices such as thermal diodes [20, 21], thermal transistors [204, 205] and thermal cloaks [22–25]

An active research topic in the field of phononic crystals concerns the influence of particle-like incoherent and wave-like coherent phonon heat transport and their individual contributions to the reduction of the thermal conductivity in PnCs [55, 206–211]. The term incoherent phonon scattering refers to all diffusive scattering processes in which the phase information of the phonon is lost. These include phonon-phonon (Umklapp) scattering, phonon-impurity scattering and diffusive phonon-boundary scattering as discussed in section 3.1. In contrast, coherent phonon effects preserve the phase of the phonons and wave interference occurs. Several recent publications have therefore tried to distinguish particle-like effects and wave-like effects in two-dimensional phononic crystals [55, 206–215]. The majority of these works focuses on silicon based two-dimensional phononic crystals built of air-filled cylinders in a silicon suspended thin film or membrane where the holes are usually aligned in ordered square, hexagonal, or honey-comb lattices. The main line of arguments to explain the reduction of thermal conductivity in these phononic crystals usually follows the following ideas:

- The introduction of air holes leads to the formation of additional interfaces which increase phonon boundary scattering and effectively reduce the thermal conductivity.

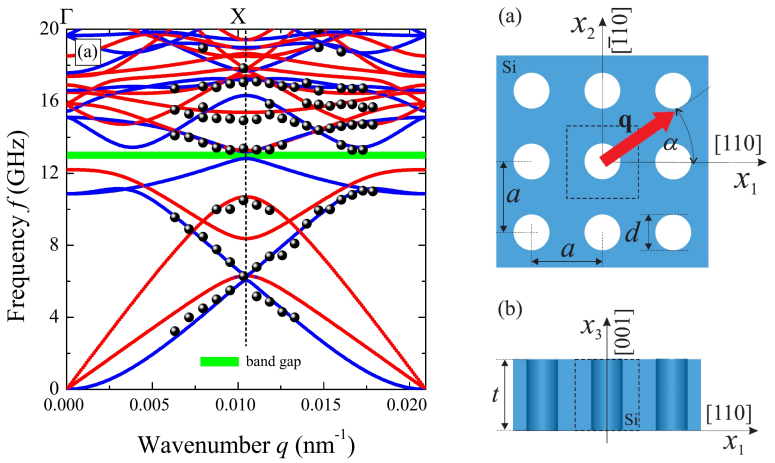

Figure 3.5: Left: Phonon dispersion relation of a 2D phononic crystal of air-filled cylinders in a Si suspended film of 250 nm thickness. Data points represent measured frequency by Brillouin light scattering, solid lines show the calculated phonon dispersion relation for symmetric (red) and antisymmetric (blue) modes obtained by finite element modeling. The green bar indicates the presence of a phononic band gap in the GHz frequency range. Right: Schematic top view (a) and lateral view (b) of the phononic crystals structure and orientation [160]. Reprinted with permission from Physical Review B 91, 075414. Copyright (2015) American Physical Society.

- For a second-order periodicity below the mean free path of phonons, an additional reduction of the thermal conductivity may occur as the length scale for ballistic propagation of phonons is reduced by the additional interfaces.
- Beyond these purely particle-related effects, coherent wave-like effects may also reduce the thermal conductivity due to the introduction of phononic bandgaps and the reduction of the phonon group velocities.

While the first two points describe well-established mechanisms related to phonon scattering processes, the experimental proof for coherent phonon heat conduction poses significant challenges in the absence of a direct measurement technique for thermal phonon coherence and fuels controversial discussions up to the present day. So far, most works rely on the measurement of the thermal conductivity in structures with varying geometrical features in order to deduce indirectly the presence of coherent phonon heat conduction.

An elegant approach to study the existence of coherent wave-like phonon effects and the potential impact of phonon coherence on the thermal properties is based on the fabrication of ordered and disordered two-dimensional phononic crystals. The approach relies on the basic principle that wave interference of phonons will be dis-

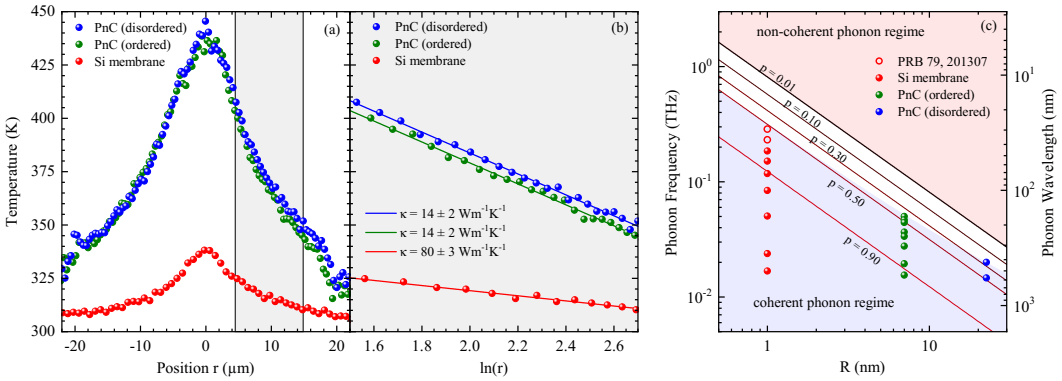

Figure 3.6: (a) 2 laser Raman thermometry line scans of an unpatterned Si membrane, an ordered, PnC and a disordered PnC. (b) Logarithmic plot of the highlighted area in (a) to visualize the *ln(r)* relation (section 2.1.1). (c) Phonon frequency / phonon wavelength as a function of disorder and roughness parameter *R*. Solid lines indicate the dependence for selected specularity parameters p between 0.01 and 0.90. Data points represent measured coherent acoustic phonon frequencies. The blue-shaded area indicates the coherent phonon regime extrapolated from the highest measured coherent phonon frequencies, the red-shaded area marks the non-coherent phonon regime [55]. Reprinted with permission from Nano Letters 16, 5661. Copyright (2016) American Chemical Society.

turbed by the introduction of disorder, which will nullify a potential reduction of the thermal conductivity by coherent phonon effects. Fig. 3.6 displays thermal conductivity measurements of ordered and disordered two-dimensional phononic crystals obtained by two laser Raman thermometry (section 2.1.1). Independent of the level of disorder in the PnC lattice, the same thermal conductivity of about 14 $\mathrm{Wm^{-1}K^{-1}}$ at room temperature were observed as compared to 80 $\mathrm{Wm^{-1}K^{-1}}$ in the unpatterned Si membrane (Fig. 3.6 a,b) [55]. This six fold reduction is well within expected parameters and can be solely explained by non-coherent effects related to increased phonon scattering in the patterned membrane. Beyond that, the equal thermal conductivity of the ordered and disordered PnCs indicates that high frequency thermal phonons do not experience coherent effects in these structures.

Using femtosecond pump-probe reflectivity measurements, we have therefore investigated the frequency limit for the presence of coherent acoustic phonons [55]. It could be shown that phonon interference is strongly affected by both disorder and roughness and that for a given roughness of 1 nm, coherent phonon effects would play a negligible role for frequencies above about 400 GHz (see Fig. 3.6). Taking into account that most of the heat-carrying phonons at room temperature have frequencies in the low THz range, the absence of coherent phonons in this range directly explains why the room temperature thermal conductivity is not affected by disorder in

the phononic crystals. Consequently, modifications of the thermal conductivity due to phonon coherence will only occur for very smooth surfaces/interfaces where the limit of the coherent phonon regime reaches the THz range or for sufficiently low temperatures where the wavelength of the thermal phonons is significantly larger and thereby greatly exceeds the characteristic roughness of the phononic crystal structure.

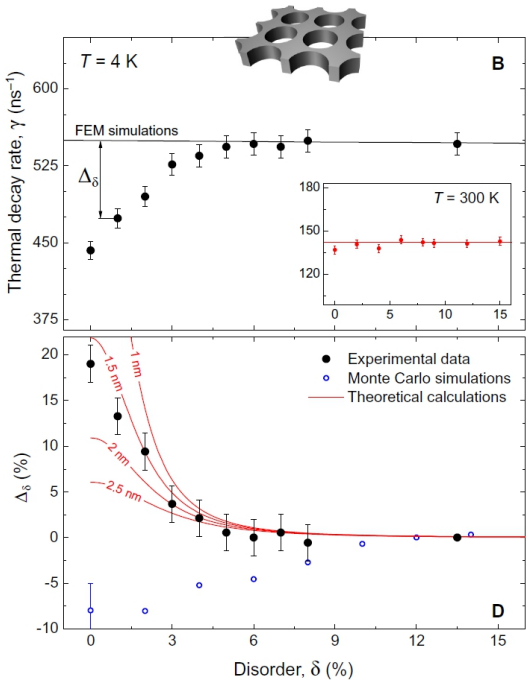

Figure 3.7: Top: Thermal decay rate measurements of 2D phononic crystals with varying disorder. At 4K, the thermal decay rate depends on the level of disorder whereas at 300 K heat dissipates through ordered and disordered structures at an equal rate (inset). Bottom: Theoretically expected disorder dependence alongside the experimentally measured difference between thermal decay rates for different values of the effective surface roughness [210]. Reprinted with permission of AAAS from Science Advances 3, e1700027. Copyright The Authors, some rights reserved; exclusive licensee American Association for the Advancement of Science. Distributed under a Creative Commons Attribution NonCommercial License 4.0 (CC BY-NC).

These conclusions were later confirmed by the study of 2D PnCs with varying level of disorder in the second-order periodicity at cryogenic temperatures. Corresponding time-domain thermoreflectance measurements (section 2.1.2) of PnCs with varying level of disorder were reported by Maire et al. and are displayed in Fig. 3.7 [210]. A pronounced reduction of the thermal decay rate, which corresponds to a reduction in thermal conductivity, is observed in the ordered PnC lattice at T = 4 K. With

increasing level of disorder, the values approach a constant threshold. In contrast, the thermal decay rate at room temperature (Fig. 3.7 inset) is independent of the amount of lattice site disorder in the PnCs. Temperature depend studies have further shown that the reduced thermal conductivity in the ordered PnCs is only observable for temperatures below about 10 K. At these temperatures, the wavelength of the heat-carrying phonons is of similar size as the periodicity of the phononic crystal lattice so that wave-interference effects in ordered PnCs occur at frequencies of heat-carrying phonons.

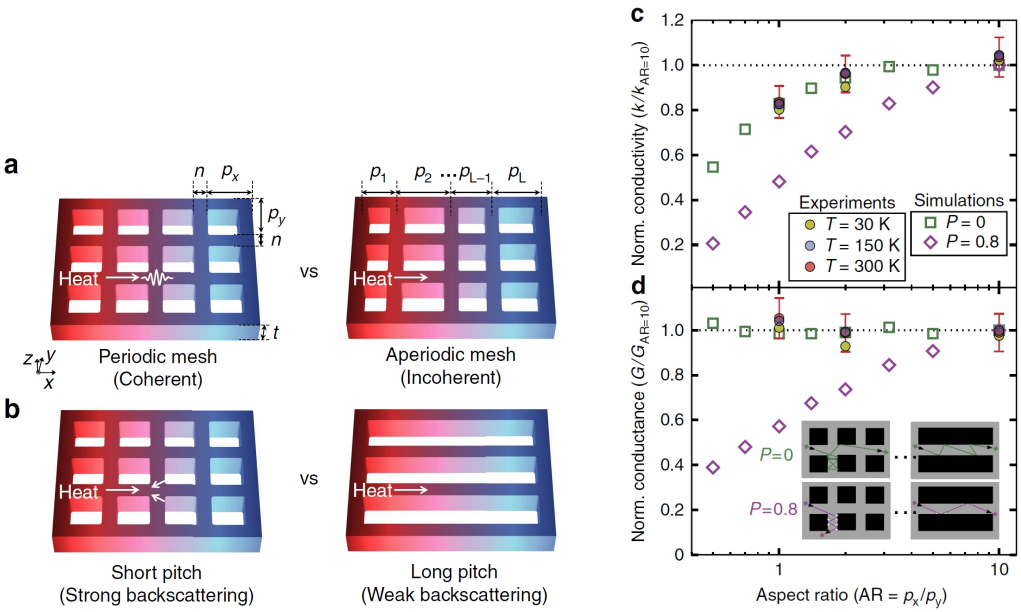

Figure 3.8: a) Periodic and aperiodic nanomesh structures to distinguish between coherence effects and particle backscattering effects, b) Variation of pitch to quantify the contribution of phonon backscattering at the bridging necks. c) Normalized thermal conductivity and d) normalized thermal conductance as function of varying pitch aspect ratio for experimental values at three different temperatures and simulations assuming fully diffusive (p=0) and partly specular (p=0.8) scattering [216]. Reprinted from Nature Communications 8, 14054. Copyright (2017) licensed under CC BY 4.0.

A particular case of ordered and disordered 2D phononic crystals are quadratic and rectangular nanomeshes [212, 216, 217]. One advantage of these nanomeshes is the possibility to adjust the spacing of holes in one direction while leaving it constant in the other direction. In this way, a transition from a regularly-ordered lattice to an equally spaced nanowire geometry can be realized (see Fig. 3.8). Such a design variation can be used to decouple the contributions of wave-related coherence effects and particle-related effects with particular sensitivity to the contributions

of phonon backscattering [216]. Analogous to the previously discussed phononic crystals, nanomeshes are typically realized as thin suspended films or membranes with a fabricated periodic mesh of holes.

Fig. 3.8 shows the schematic illustrations of periodic and aperiodic nanomeshes with different pitch between the vertically bridging necks and the corresponding measurements of the normalized thermal conductivity and thermal conductance. The modification of the thermal conductivity as function of pitch in the aperiodic nanomeshes is caused by the change in wall density that can be explained by phonon-backscattering. This conclusion is in accordance with several recent works, which mostly agree that coherent phonon effects do not contribute to the reduction of the thermal conductivity in lithographically fabricated 2D phononic crystals at room temperature.

Apart from the investigation of coherent wave-like effects, another promising research development in recent years targets the realization of directional heat propagation by ballistic phonon transport [136, 218, 219]. The concept relies on the fact that phonons can travel in straight lines (or undergoing fully specular reflection at surfaces and interfaces) without heat dissipation for hundreds of nanometers as observed in various nanostructures including membranes [185], holey silicon [220], and nanowires [124]. However, in order to exploit this property for practical applications, it is crucial to achieve control over the directionality of the phonon propagation. Such a directional control of ballistic phonons was recently demonstrated by Anufriev et al. in patterned silicon nanostructures consisting of aligned and staggered phononic crystals with varying periodicity [26]. Using TDTR measurements (section 2.1.2) it was shown that the obstruction of ballistic heat conduction in staggered structures results in a significant reduction of the thermal conductivity as compared to the samples with aligned holes. Furthermore, it was demonstrated that heat propagation can be guided by a regular phononic crystal lattice.

Fig. 3.9 displays phononic crystal lattices that are aligned (b) and disaligned (c) towards suspended nanowires. The relative differences between thermal decay times as function of nanowire length (T = 4 K) and temperature (1 μm length) are shown in Fig. 3.9 (d) and (e), respectively. In the case of the aligned nanowires, heat dissipates up to 15 % faster through the coupled structure as compared to the uncoupled one. The results demonstrate that phononic crystals can act as a directional source of ballistic phonons that propagate preferentially in a predefined direction, in this case along the nanowire axis [26]. The effect decreases with increasing length of the nanowires as heat conduction eventually becomes diffusive regardless of the initial direction for length scales beyond the phonon mean free path.

The directional heat propagation becomes even more pronounced at low temperature due to two different effects: Firstly, the phonon wavelength λ becomes longer at low

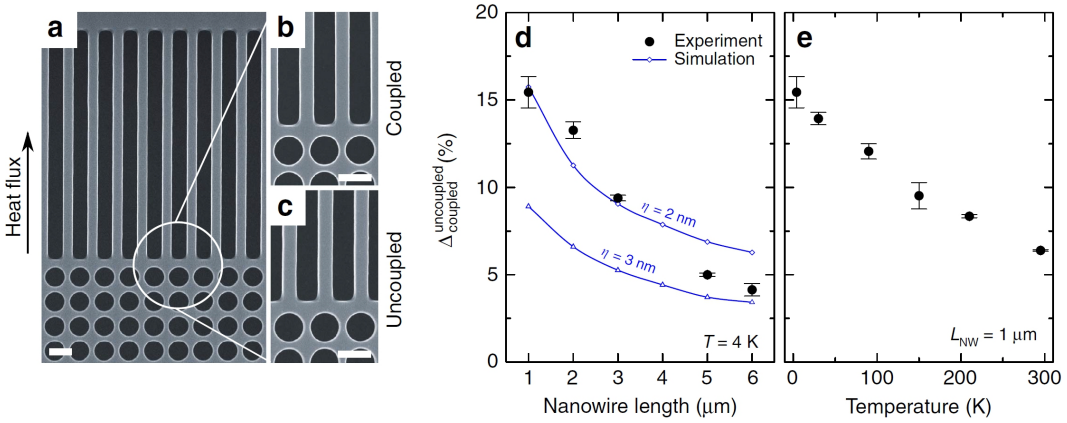

Figure 3.9: (a) SEM image of a nanowire-coupled phononic crystal sample. Close-up views showing the difference between the coupled (b) and uncoupled (c) samples. The scale bar is 300 nm. Difference between the coupled and uncoupled samples $\Delta_{coupled}^{uncoupled} = (\tau_{uncoupled} - \tau_{coupled})/\tau_{coupled}$ as function of nanowire length (d) and temperature (e) measured by TDTR. Error bars show standard deviation between different measurements on the same sample. Monte Carlo simulations (blue lines) for roughness η of 2 and 3 nm [26]. Reprinted from Nature Communications 8, 15505. Copyright (2017) licensed under CC BY 4.0.

temperatures, which increases the probability of specular scattering p expressed by

$$p = \exp(-\frac{16\pi^2\eta^2 cos^2\alpha}{\lambda^2}) \tag{3.6}$$

where η is the surface roughness and α is the normal incidence angle. Hence, the incident angle for specular reflection becomes wider with increasing phonon wavelength, which effectively increases the number of ballistic phonons at low temperatures. Secondly, the phonon mean free path Λ lengthens at lower temperatures [6, 221, 222] or, in other words, phonons can travel ballistically over longer distances in the micrometer range.

These recent approaches demonstrate the potential of controlling the directionality of ballistic heat propagation and will further benefit from the realization of smaller nanostructures by advanced nanofabrication techniques and materials with increased phonon mean free path. It therefore becomes conceivable to fabricate phononic structures that can guide, confine, or disperse heat fluxes on length scales of typical nano- and microstructures.

3.4.3 Superlattices

The propagation of heat in superlattices (SLs) is determined by a variety of different mechanisms. In particular, the thermal properties are defined by the acoustic

impedance mismatch between the different materials of the superlattice [223–225], the thermal boundary resistance at the interfaces, alloy scattering [223, 224], the formation of phonon minibands due to the interference of coherently reflected phonons from multiple interfaces [225, 226], phonon tunneling [227, 228], and coherent phonon heat conduction [131, 132].

In contrast to the previously discussed 2D phononic crystals and nanomeshes, superlattices constitute a type of 1D phononic crystal, which, in principle, are capable of overcoming the main limitations for coherent phonon heat conduction in lithographically fabricated 2D PnCs. In particular, these are an interface roughness, which is about one order of magnitude smaller than the phonon wavelength and a second-order periodicity of the same order as the wavelength of the heat-carrying phonons (Fig. 3.6c). Both conditions are nowadays accessible by epitaxial growth techniques such as molecular beam epitaxy (MBE), metal-organic-chemical vapor deposition (MOCVD) and atomic layer deposition (ALD) which under ideal conditions enable atomically flat superlattice structures over many superlattice periods. Consequently, superlattices constitute an ideal platform to study the particle and wave nature of phonons via their thermal transport properties [131, 132, 229].

While the experimental study of coherent phonon effects in 2D phononic crystals is mainly limited to Si caused by the maturity of Si nanofabrication techniques, the epitaxial growth of superlattices allows a much wider range of materials which satisfy the requirements on interface roughness and periodicity. These include for example the semiconductor-semiconductor SLs GaAs/AlAs [131], $CaTiO_3$/SrTiO [132], SiGe [223, 224], Si/SiOx [230], and AlN/GaN [231], the metal-semiconductor SLs W/Al_2O_3 [232], TiN/AlScN [233, 234], and ZrN/ScN [235], as well as inorganic-organic SLs such as ZnO/benzene [236, 237] and TiO_2/benzene [238]. As the large quantity of recent works renders a comprehensive discussion within the scope of this chapter impossible, only few selected examples are mentioned, which focus on the possibility of coherent wave-like effects in superlattices.

This research field was widely stimulated by the report of coherent phonon heat conduction in epitaxially grown GaAs/AlAs superlattices with an individual layer thickness of 12 nm. Time-domain thermoreflectance measurements (section 2.1.2) have shown a linear increase of the cross-plane thermal conductivity with increasing number of periods in the temperature range between 30 und 150 K (Fig. 3.10) which was attributed to thermal transport by coherent phonons [131]. Above 150 K, the increase of k is less pronounced which indicates the presence of diffusive interface scattering as the wavelength of the heat-carrying phonons decreases with increasing temperature. However, the persistent increase of k as function of SL periods evidences the existence of partial phonon coherence and their contribution to the heat propagation even at elevated temperatures over 150 K [131].

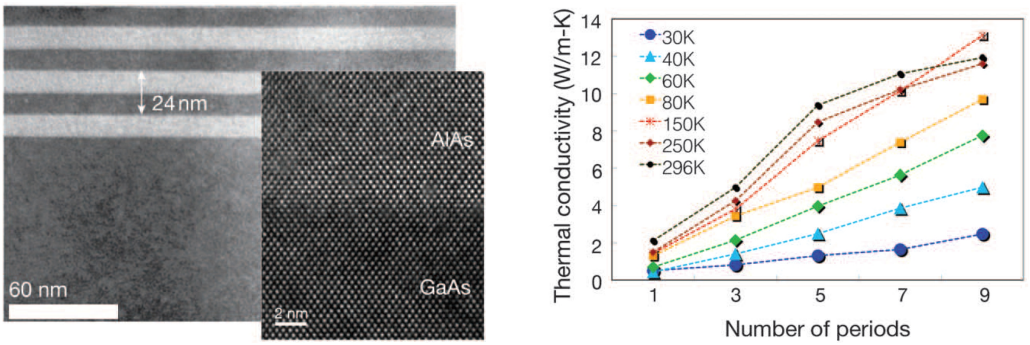

Figure 3.10: (left) Cross-sectional TEM image of the 3-period GaAs/AlAs SL, (inset) HRTEM image of one of the interfaces. (right) TDTR measurements of thermal conductivity of GaAs/AlAs superlattices as a function of number of SL periods for different temperatures between 30 K and 296 K [131]. (Reprinted with permission of AAAS from Science 338, 936. Copyright (2012) American Association for the Advancement of Science.

In a slightly different approach, Ravichandran et al., have studied the thermal conductivity of perovskite superlattices with intrinsically low phonon Umklapp scattering as function of periodicity [132]. The authors observed a minimum thermal conductivity for a specific superlattice periodicity that was attributed to a crossover between coherent wave-like and non-coherent particle-like phonon heat conduction (Fig. 3.11a). The minimum forms because of opposing dependences of k as function of interface density in the coherent and non-coherent transport regime. In the non-coherent regime, a reduction of the period thickness reduces the thermal conductivity as phonons experience diffusive boundary scattering at each interface. In other words, the phonons behave particle-like and thus the thermal resistance increases with increasing interface density. A further decrease in the period thickness reverses this trend and results in an increase of k. This behavior is not compatible with only diffusive phonon scattering. Considering that the period thickness is now in the range of the coherence length of thermal phonons, the observed increase in k for small period thicknesses reflects the wave nature of phonons and was attributed to the presence of coherent phonon heat conduction. The combination of both effects results in a minimum of k that becomes more pronounced at lower temperatures due to the increase of the phonon wavelength and reduction of Umklapp scattering.
Following these initial works on coherent phonon heat conduction, several follow-up works have appeared in recent years that investigate the impact of phonon coherence in various superlattice structures. These include a variety of theoretical works which investigate phonon coherence in various superlattices [240] and random multilayers [241, 242] such as Si/Ge [229], GaAs/AlAs [243], graphene/h-BN [244, 245],

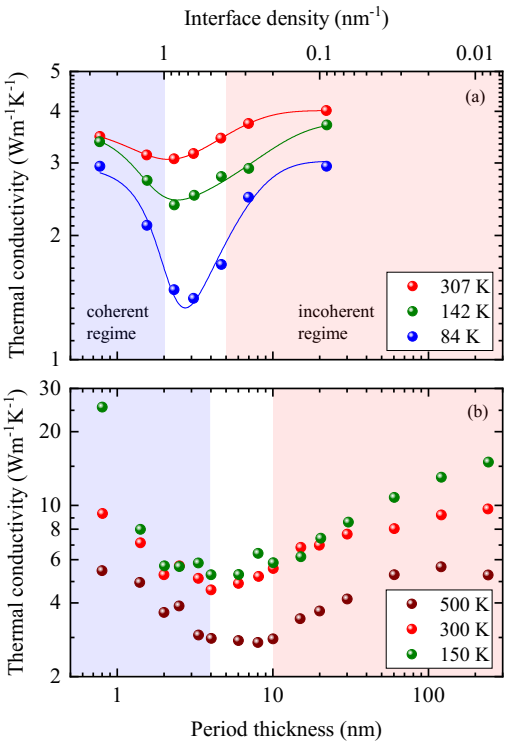

Figure 3.11: Measured thermal conductivity values for $(STO)_m$=$(CTO)_n$ superlattices [132] (a) and $TiN/Al_{0.72}Sc_{0.28}N$ metal/semiconductor superlattices [239] (b) as function of period thickness (interface density) at different temperatures measured by TDTR. Solid lines (a) are guides to the eye. A minimum in the thermal conductivity is visible in both superlattice systems which persists over a wide range of temperatures. Adapted from references [132] and [239].

C^{12}/C^{13} [246], and van der Waals superlattices [247]. Recently, additional experimental support for coherent phonon heat conduction in SLs was published by Saha et al. [239]. Fig. 3.11b displays the measured cross-plane thermal conductivity of $TiN/Al_{0.72}Sc_{0.28}N$ metal/semiconductor SLs as function of period thickness for temperatures of 150 K, 300 K, and 500 K. Similarly to the previously discussed work by Ravichandran et al. [132], the minimum of k becomes more pronounced at lower temperatures and is explained by the crossover between the non-coherent and coherent phonon regimes.

Apart from these works, the lowest in-plane thermal conductivity of Si-based planar superlattices was recently reported considering exclusively non-coherent effects [230]. Hybrid nano-membrane superlattices were fabricated by strain-engineered role-up and compression of 20 nm Si and 2nm amorphous SiO_x layers. Thermal conductivity measurements were conducted using the suspended microchip suspended platform technique (see section 2.2.3). The strong reduction of the thermal conductivity

(about 3 times lower than in an individual 20 nm thick Si layer) was attributed to a dominant phonon scattering in the SiO_2 layers. The results are in agreement with the previously discussed reduction of the thermal conductivity in Si membranes (section 3.4.1) [54] and phononic crystals [248] by the native oxide and emphasize the crucial role of the surface configuration not only in suspended ultra-thin films but also in superlattice structures.
The here discussed works demonstrate that 1D superlattices constitute a versatile class of nanostructures for both, the study of fundamental properties such as the conditions for phonon interference and coherence, and, for the realization of materials with very low thermal conductivity by the exploitation of coherent and non-coherent phonon effects. Together with their 2D and 3D counterparts, 1D superlattices can be used to build phononic metamaterials which hold the promise of many more interesting discoveries and applications in the field of nanoscale thermal transport in the near future.

3.4.4 Nanowires

Nanowires, in their idealized 1D geometry, constitute another interesting class of materials for the study of thermal transport and phonon coherence at the nanoscale. In particular, Si nanowires have attracted great attention due to their excellent physical and chemical properties and ideal interface compatability with conventional Si technology [8, 249]. Since the thermal conductivity of bulk Si is governed by phonons with a broad distribution of mean free paths [6], Si nanowires are well-suited to study size effects on the thermal conductivity. Several works have reported a diameter dependent reduction of the thermal conductivity of Si nanowires as compared to bulk Si [12, 250, 251]. Fig. 3.12 displays the temperature dependent thermal conductivity of two series of Si nanowires with varying diameters fabricated by vapour liquid solid growth (VLS) [250] and electroless etching [12]. Both series exhibit a reduction of thermal conductivity with decreasing NW diameter which is caused by an increase of diffusive phonon boundary at the surface of thinner NWs resulting in the reduction of the phonon mean free path.
Comparing the two data set in Fig. 3.12, it is interesting to note the significantly stronger reduction of k in the etched NWs as compared to the VLS grown ones. As discussed already in the previous sections 3.4.1 to 3.4.3, not only the dimension but also the surface composition and roughness affects the thermal transport in nanostructures [54, 55, 154]. High-resolution TEM images of the NWs reveal smooth surfaces in the VLS NWs (roughness of 1-2 monolayers) as compared to a mean roughness height and period of up to 5 nm in the etched NWs [12]. Thus, the roughness at the surface of the NWs reduces specular phonon reflection in favor of diffusive scattering and backscattering of phonons, resulting in an additional reduc-

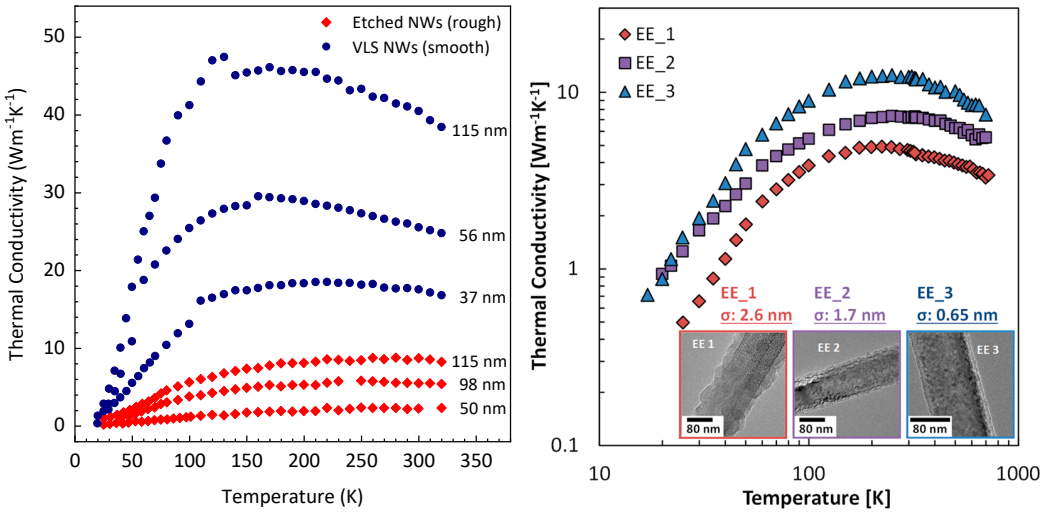

Figure 3.12: Left: Temperature dependent thermal conductivity of vapour-liquid-solid (VLS) grown Si NWs (dark blue circles) [250] and Si NWs fabricated by electroless etching (EE) (red diamonds) [12] with diameters between 37 nm and 115 nm. Adapted by permission from Springer Nature: Nature 451, 163. Copyright (2008). Right: Temperature-dependent thermal conductivity of electroless etched (EE) Si nanowires with different surface roughness between 0.65 nm and 2.6 nm [252]. Reprinted with permission from Nano Letters 16, 4133. Copyright (2016) American Chemical Society.

tion of thermal conductivity beyond size effects. Similar observations were reported by Boukai et al. [13] who measured a reduction of k in 10-20 nm wide Si NWs by more than 2 orders of magnitude as compared to the bulk value, thus approaching or even surpassing the amorphous limit of Si of 1.7-2.1 $\mathrm{Wm^{-1}K^{-1}}$ [6, 253]. Such a drastic reduction could not be explained by theoretical models considering only the diameter and average roughness of the NWs. Instead, Lim et al. found that the reduction of k is more correctly described considering both root-mean square (rms) value and correlation length of the surface roughness [254]. Subsequently, Lee et al. [252] conducted a detailed study of the temperature dependent thermal conductivity of NWs with well-defined surface roughness and correlation length which revealed persistent reductions of k with increasing rms roughness and decreasing correlation length of the entire temperature range from 20-700 K (Fig. 3.12b).
Recently, Mukherjee et al. [255] have studied the influence of isotope disorder and crystal phases on the thermal conductivity of Si NWs. The NWs were investigated by HAADF-STEM analysis and differentiated in cubic, rhombohedral, and mixed polymorphs. The highest thermal conductivity was observed for isotopically pure ^{29}Si NWs in the cubic crystal phase. Both structural and isotopic disorder were shown to reduce the thermal conductivity with the lowest k obtained for $^{28}\mathrm{Si_x}{}^{30}\mathrm{Si_{1-x}}$ NWs

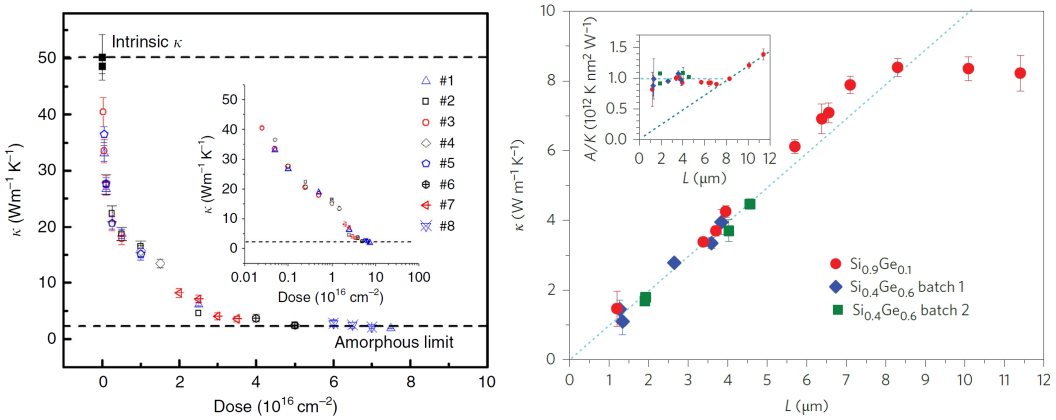

Figure 3.13: Left: Thermal conductivity as function of He ion irradiation dose for eight different Si NW samples. Inset: Same data plotted on a logarithmic scale. Solid black squares denotes the thermal conductivity of non-irradiated NWs as reference [256]. Reprinted from Nature Communications 8, 15919. Copyright (2017) licensed under CC BY 4.0. Right: Thermal conductivity of SiGe NWs with different diameters and alloy compostions as function of NW length l. The inset displays the same data plotted as thermal resistance per unit area (A/k) as function of l. Dotted lines indicate linear fits to the data in the ballistic ($l < 8.3\,\mu$m) and diffusive ($l > 8.3\,\mu$m) regimes [124]. Reprinted by permission from Springer Nature: Nature Nanotechnology 8, 534. Copyright (2013).

with rhombohedral phase. Furthermore, the isotope-disorder induced reduction of k was found to be insensitive to the crystal phase, thus demonstrating the general role of phonon isotope scattering in the reduction of the thermal conductivity [255]. Phonon scattering at defects constitutes another scattering mechanism responsible for the reduction of k. The influence of defects introduced by helium ion irradiation on the thermal properties of NWs was studied by Zhao et al. [256]. A linear decrease in thermal conductivity by up to 70% was observed for point defect concentrations up to about 4% underlining the strong influence of phonon scattering by point defects on k (see Fig. 3.13a). For higher irradiation doses, the reduction in thermal conductivity saturates and approaches the amorphous limit of k as the irradiation dose is sufficient to induce the transition from the crystalline to the amorphous phase [256]. These works demonstrate the impact of intrinsic phonon scattering by defects, isotopes, and structural disorder in addition to the reduction of the phonon mean free path by diffusive boundary scattering at the (rough) surface of the NWs. Finally, several works have recently appeared focusing on the ballistic transport of phonons in NWs, meaning the absence of scattering mechanisms other than specular phonon reflections on the surface [124, 125, 210, 257]. Such ballistic heat transport was demonstrated in SiGe alloy NWs [124] and Si-Ge core-shell NWs [125] where the

phonon mean free path was found to be 8.3 μm and 5 μm, respectively. Using the microchip suspended platform technique (section 2.2.3), the thermal conductivity of the SiGe NWs was found to increase linearly with length l up to 8.3 μm (see Fig. 3.13b). This behavior is consistent with Laundauer's formulation for a ballistic thermal conductor where $k \propto l$ [258]. For longer NWs, k remains constant since additional dissipation occurs inside the SiGe NWs and heat transport occurs as in an ordinary diffusive thermal conductor [124]. The reason for the long phonon mean free path is found in the localization of high frequency phonons resulting in the reduction of the thermal conductivity k in the NWs. Taking into account that phonon scattering by defects increases with ω^4, the ballistic heat conduction over long distances must be carried by low frequency acoustic phonons. It was shown that alloy concentrations below 10% are sufficient to localize most high frequency phonons enabling low-frequency phonons, which occupy 0.1% of the excited phonon spectra, to become the dominant heat carriers [125]. The remaining long-wavelength phonons experience only specular reflection at surfaces and low defect scattering resulting in the observed long phonon mean free path. In the case of pure Si NWs, semi-ballistic heat transport was observed only at low temperatures as phonons with long wavelength contribute to heat transport and undergo specular reflection at the NW surface [210].

The previously discussed works make use of several different experimental techniques to tackle the delicate task of thermal transport measurements in single NWs. The most common technique is to suspend the NWs between microfabricated platforms for heating and sensing (section 2.2.3) [106, 124, 125, 250, 252]. More recently, the thermal conductivity was also determined using a modified microchip suspended platform consisting of 2 sensor pads at the edges of the suspended NW which is heated by a focused electron beam [125, 256, 259]. For electrically conducting nanowires, a convenient approach is to use self-heating in a 3-omega type measurement (section 2.2.1), although it requires careful consideration of both thermal and electrical contact resistances [260, 261]. Scanning thermal microscopy (section 2.2.2) furthermore enables high-resolution thermal imaging of composition, diameter, or defect gradients along the NWs [104, 262]. Non-contact techniques, such as Raman thermometry (section 2.1.1) are less frequently applied for thermal measurements of single nanowires [255, 262, 263]. The main challenge lies in the accurate determination of the absorbed power which is complicated when the diameter of the NW d is smaller than the diffraction-limited size of the heating or probing laser ($d \leq 500\,nm$) [37]. Finally, thermoreflectance based techniques are gaining increasing attention for the study of ballistic transport in NWs [210, 264]. For a detailed discussion of experimental approaches and challenges of thermal transport measurements in single NW, the reader may refer to the reviews in Refs. [3, 43, 45, 265].

3.4.5 Quantum dots

Very few experimental works exist that address the thermal properties of quantum dots. The main reason is the tremendous challenge to realize a thermal probing technique with a spatial resolution commensurate to the dimensions of quantum dots, i.e. ≤ 10 nm. This requirement disqualifies almost all of the in chapter 2 discussed methods for the study of thermal properties of quantum dots. Furthermore, temperature changes due to energy dissipation in e.g. quantum dot emitters are exceptionally small and require not only nm spatial resolution but also μK temperature resolution. Consequently, experimental studies of the thermal conductivity usually address the collective properties of quantum dots in a matrix material. These include both randomly distributed Ge quantum dots in Si [266, 267] and periodic Ge dots in Si/Ge superlattices [74, 266–270]. Thermal conductivity measurements were conducted using the 3-omega method (section 2.2.1) [74, 266–270] and thermoreflectance based on ASOPS (sections 2.1.2 and 2.1.3) [74]. These studies are usually motivated by the prospect to achieve very low thermal conductivity in materials with good electrical conductivity for more efficient thermoelectric energy conversion. In a comparative study between vertically aligned and disaligned quantum dots, a two-fold reduction in the thermal conductivity in the uncorrelated structures was observed as compared to the aligned QD structure (7 instead of 14 $\mathrm{Wm^{-1}K^{-1}}$ at room temperature) and attributed to the randomization of the dot spatial distribution [267].

In 2010, Pernot et al. [74] achieved a record low thermal conductivity value of 0.9 $\mathrm{Wm^{-1}K^{-1}}$ at room temperature in 5 layers of epitaxial Ge dots separated by Si spacers. The experimental observations were explained by a totally diffusive mismatch model for the barriers, i.e. phonons scatter in a completely diffusive way [74]. High-resolution transmission electron microscopy (HRTEM) and atomic force microscopy (AFM) imaging of the layer structures could further exclude the presence of dislocations or extended defects as additional phonon scattering centers. The question remains if there are any indications for an additional reduction of the thermal conductivity due to wave interference effects. However, the absence of a thermal conductivity minimum for a series of layer periods down to 3.7 nm rather supports the conclusion that the low thermal conductivity is solely achieved by highly diffusive phonon scattering at the dots and that no coherent effects participate (c.f. section 3.4.3 and Fig. 3.11) [74].

Recently, Halbertal et al., have demonstrated a major breakthrough in the thermal study of quantum dots and extended defects in carbon nanotubes and graphene using a superconducting quantum interference device placed on a sharp tip of a scanning microscope (see perspectives in section 2.3) [143, 144]. Using this approach, the energy dissipation of individual quantum dots by single-electron charging could be measured with sub-μK sensitivity. These recent advances constitute the first

promising examples of thermal imaging of nanoscale dissipation processes in quantum structures.

3.5 Conclusion and perspectives

This chapter has elucidated fundamental aspects of phonon mediated thermal transport such as phonon scattering mechanisms, phonon mean free path, phonon confinement, and phonon lifetimes. Subsequently, the largest part of this chapter has focused on the discussion of coherent and non-coherent thermal transport in nanostructures with different geometry. These include suspended thin films, two-dimensional phononic crystals, superlattices, nanowires, and quantum dots. While most of the existing studies focus on the thermal transport governed by non-coherent phonon scattering in order to reduce the thermal conductivity for thermoelectric applications, the field of heat conduction by coherent phonons is still in its infancy. Several recent examples for successful demonstration of coherent phonon wave effects and ballistic phonon propagation were discussed in phononic crystals, superlattices, and nanowires. All of them have in common that surface and interface roughness plays a crucial role in the preservation or destruction of phonon coherence. Furthermore, the periodicity of phonon structures with second-order periodicity should commensurate the wavelength of thermal phonons and the phonon mean free path should be sufficiently long to allow interference effects. With the continuing miniaturization in semiconductor devices and improvement of nanofabrication techniques, many of these conditions are nowadays complied with and heat manipulation and guidance based on coherent effects and ballistic transport have the potential to become a corner stone of future nanoscale heat engineering.
Apart form the discussed aspects in this chapter, two most recent research highlights shall not be left unmentioned. These are the discoveries of ultra-high thermal conductivity in boron arsenide (BAs) and the observation of second sound at elevated temperatures in graphite.

Ultra-high thermal conductivity materials:

While most of the literature on thermal properties focusses on low k materials for thermoelectric energy conversion, high k materials are crucial as heat spreaders for the thermal management of high-power electronics and high-power light emitters. Currently, they rely mostly on the metals Ag, Cu, and Al as well as the non-metals synthetic diamond, BN, and SiC, all of which have higher k values than the best conducting metal Ag. In 2018, three independent works were published in the same issue of Science which reported record high values of the thermal conductivity in cubic boron arsenide (BAs) single crystals at room temperature [271–273]. The obtained

values for k all lie within ±15% of the cross study average of 1140 $Wm^{-1}K^{-1}$ and were measured using TDTR (section 2.1.2). The results deserve particular attention as they break with conventional guidelines for high k materials which favor - apart from a simple crystal structure, strong interatomic bonding and low anharmonicity - mainly lattice atoms with low atomic mass [274]. This simple relation was firmly established in e.g. group IV elements with $k_{Ge} < k_{Si} < k_{Diamond}$ and was also taken for granted in binary compound semiconductors such as $k_{BAs} < k_{BP} < k_{BN}$. Thus, the predicted value of 200 $Wm^{-1}K^{-1}$ for BAs [274] was well within the expected range, although it was never measured since its prediction in 1973.
40 years later, the direct calculation of k became possible due to significant advances in computational power and algorithms solving the Boltzmann transport equation using atomic force constants calculated from first principles. Using these modern theoretical tools, Lindsay et al. and Feng et al. calculated k values for BAs of 2200 $Wm^{-1}K^{-1}$ considering 3-phonon scattering [275] and 1400 $Wm^{-1}K^{-1}$ including also 4-phonon scattering processes [276]. The experimental confirmation of such high k values in BAs [271–273] supports the theoretical prediction that ultra-high thermal conductivity in non-metals is related to acoustic phonon bunching combined with large acoustic-optical gaps [275]. In other words, a suppression of k limiting three-phonon scattering processes can occur, when the energy gap between acoustic and optical branches is large and when the three acoustic branches are bunched closely together [277]. As such, binary compound semiconductors with large mass ratios such as BAs are prime candidates for high-k materials where the remaining challenge lies in the growth of pure and defect free materials so that no other phonon scattering mechanisms at defects and impurities limits k. Moreover, the elimination of isotope scattering in isotopically pure crystals can further increase the thermal conductivity. In the case of BAs, phonon-isotope scattering is already weak since As is a monoisotopic element, i.e. it has only one stable isotope (^{75}As), and calculations predict an additional increase of k of about 40% for isotopically purified BAs [275]. Most recently, the influence of isotope scattering was experimentally demonstrated in cubic boron nitride (cBN). Using TDTR and FDTR measurements, Chen et al. reported an almost twofold higher thermal conductivity in isotopically pure $c^{10}BN$ and $c^{11}BN$ (about 1650 $Wm^{-1}K^{-1}$) as compared to $c^{nat}BN$ with natural isotope distribution (880 $Wm^{-1}K^{-1}$) [278].

Second sound at elevated temperatures:

Second sound, also called hydrodynamic phonon transport, is the non-resistive, wave-like propagation of heat by collective phonon flow (see Fig. 3.14), which was first predicted in single crystals of solid dielectrics in 1947 and experimentally observed in solid helium crystals in 1966 [280]. In 2019, Huberman et al. have reported

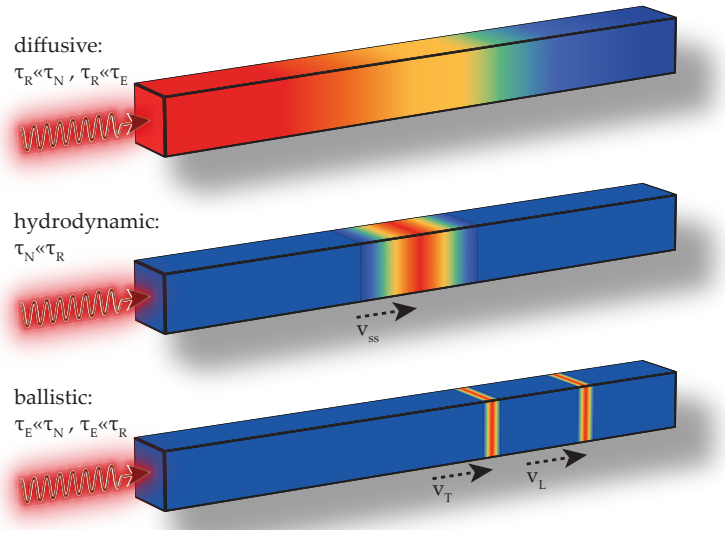

Figure 3.14: Schematic illustration of diffusive, hydrodynamic, and ballistic transport regimes. Following the generation of a thermal non-equilibrium by a heat pulse, the spatial distribution of the phonon density (red: high, blue: low) at any given time depends on the thermal transport regime. a) Diffusive transport: The phonon density (or temperature) decreases with distance from the heating spot as described by Fourier's law, b) Hydrodynamic transport: Heat is transported by non-resistive propagation of phonons in wave packets driven by Normal scattering (second sound), c) Ballistic transport: Phonons propagate with different group velocities on ballistic trajectories without scattering. Inspired by reference [279].

the experimental observation of second sound in graphite at temperatures as high as 125 K [130]. Particularly interesting in this work is the high-T range at which second sound is observed. Up to this work, only few materials were known to exhibit hydrodynamic heat transport which occurs in a transport regime between ballistic and diffusive transport and only at very low temperatures. They include ^{3}He (0.42 - 0.58 K) [280], Bi (1.2 - 4 K) [281], NaF (11 - 14.5 K) [282–284], and Al_2O_3 (3.4 K) [285]. Since no further progress was achieved in increasing the temperature range in which hydrodynamic phonon transport could appear, the topic was abandoned for almost 40 years. With the growing impact of 2D materials during the past decade, theoretical works have refocused on phonon hydrodynamics and predicted a much larger temperature window for second sound in graphene [220], graphite [286], and other 2D materials [287]. The recent work by Huberman et al. [130] marks the first experimental proof of hydrodynamic heat transport well above liquid nitrogen temperature. Within this transport regime, phonons experience mainly non-resistive Normal-scattering whereas all resistive scattering processes

including Umklapp-scattering play a negligable role. Since Normal scattering cannot dissipate a heat flux, the absence of other scattering processes results in the propagation of heat pulses as phonon density wave (Fig. 3.14) [279].
The reason why second sound was only observed in very few crystals at low temperatures lies within the stringent conditions for hydrodynamic phonon transport, i.e. the rare combination of strong Normal-scattering and weak Umklapp-scattering. Although Umklapp scattering can be easily suppressed at temperature much lower than the Debye temperature where the phonon population is limited to small wavevectors, this usually coincides with few Normal-scattering events resulting in ballistic transport. Thus, hydrodynamic thermal transport is favored in materials with high Debye temperature (reduced U-scattering) and large anharmonicity (strong N-scattering). These conditions also explain the favorable predictions for second sound in carbon-based layered materials as they combine a high Debye temperature caused by the light atomic mass of carbon and strong sp^2 hybridization with large anharmonicity of flexural modes [288]. A logical starting point in the search for other materials with pronounced hydrodynamic phonon transport are thus materials with a high population of interacting small-wavevector phonons, similar to the flexural modes in 2D systems [279].
Both recent discoveries, the unusually high thermal conductivity in BAs and the observation of non-resistive hydrodynamic heat transport in graphite challenge conventional thermal transport theories and open new pathway to non-resistive phonon propagation in ultra-high thermal conductivity materials.

4 Photonic and phononic properties of III-nitride semiconductors

This chapter lists the scientific articles related to III-nitride semiconductors and their nanostructures which are part of this cumulative thesis. The chapter consists of two main parts. The first part addresses phononic and excitonic properties in III-nitride thin films and single crystals, the second part focuses on nanostructures such as quantum wells, nanowires, and quantum dots. The applied experimental methods in these works encompass continuous-wave and picosecond time-resolved micro-photoluminescence spectroscopy (μPL, μTRPL), photoluminescence excitation spectroscopy (PLE), auto- and cross-correlation measurements in the Hanbury-Brown and Twiss configuration (HBT), (resonant) micro-Raman spectroscopy, uniaxial and hydrostatic pressure dependent Raman spectroscopy, and tip-enhanced Raman spectroscopy (TERS).

4.1 Thin films and single crystals

4.1.1 Phonon deformation potentials, Grüneisen parameters, and Born's effective charge

The first section addresses phonons in III-nitride single crystals and epitaxial films including their fundamental lattice vibrational properties such as phonon deformationen potentials, Grüneisen parameters, and Born's transverse effective charge values. The pressure coefficients and phonon deformation potentials of AlN, GaN, InN, and ZnO are determined by uniaxial and hydrostatic pressure-dependent micro-Raman measurements [289–291]. Furthermore, the hydrostatic pressure dependence of the ordinary and extraordinary refractive indices of GaN, AlN, and ZnO are determined by optical interference measurements inside a diamond anvil cell [292]. Finally, the phonon-plasmon coupling in the ternary alloy systems InGaN and AlGaN is studied by micro-Raman spectroscopy and theoretical modeling [293]. Published articles in this section include: [289–293]

4.1.2 Defects, impurities, and charge transfer mechanisms

This section contains publications that study the optical properties of epitaxially grown GaN thin films with particular focus on the spectroscopic investigation of impurities and defects and their respective energy and charge transfer mechanisms. In particular, the works focus on Mg and Si as the technologically most relevant dopants to obtain shallow acceptors and donors in GaN, respectively. The donor and acceptor binding energies as well as exciton localization and activation energies related to these impurity states are determined by a combination of temperature dependent PL and PLE spectroscopy [294, 295]. The identification of shallow impurity bound excitons and their related electronic and vibrational excited states is accomplished by high-resolution PLE which reveals charge and energy transfer processes between related optical transitions [296]. In combination with time-resolved PL, a clear distinction between effective mass like shallow donor bound excitons and defect or complex bound excitons is achieved [294]. Further works include the study of polarity effects and carrier localization in GaN lateral polar junctions [297], as well as structural and optical properties of ammono-thermal GaN [298] and epitaxial AlN [299]. Finally, a combined experimental and theoretical study of highly doped GaN:Ge indicates the stabilization of exciton-like particles by a degenerate electron gas formed for free carrier concentrations beyond the Mott density [300]. Published articles in this section include: [294–300].

4.2 Nanostructures

The second part of this chapter addresses optical and electronic properties in nitride based nanostructures. These include the study of quantum efficiency, electric field- and confinement effects, carrier dynamics, and non-classical light emission in quantum wells, nanowires, quantum wires, and quantum dots.

4.2.1 Quantum wells

The works in this section focus on the study of quantum efficiency and droop in InGaN/GaN commercial LED devices and AlGaN/AlN multi-quantum-well (MQW) heterostructures. The radiative and non-radiative charge carrier recombination processes are studied by time-resolved PL measurements on LED structures as function of operation current. The differential carrier lifetimes of InGaN LED structures are investigated by small-signal time-resolved photoluminescence (SSTRPL) in order to quantify Shockley-Read-Hall (SRH), Auger, and radiative recombination coefficients [301]. The technique combines steady-state electrical excitation with quasi-resonant, time-resolved optical excitation. In the case of the AlGaN/AlN

MQWs, resonant, time-resolved PL as function of excitation power density is applied to determine the internal quantum efficiency and quantify the radiative and non-radiative recombination coefficients [302]. Furthermore, a new method is presented in GaN/AlN MQW nanostructures that enables the tuning and suppression of the quantum-confined Stark effect in the polar growth direction. Using a pair of AlN layers on both sides of the quantum well structure, the corresponding interface charges shift the electric field gradient out of the active region, thus enabling a significantly enhanced radiative recombination rate inside the active region [303]. Published articles in this section include: [301–303].

4.2.2 Nanowires and quantum wires

The publications in this section focus on the investigation of structural and vibrational properties of nanowires with sub-diffraction spatial resolution by tip-enhanced Raman scattering (TERS). Vertically aligned InGaN/GaN quantum-well nanorods and Ge single nanowires are studied by TERS with a spatial resolution of about 30 nm. It is demonstrated that TERS mapping is capable of obtaining extensive information about local strain, composition fluctuation, charge accumulation, polymorphism, and clustering within these nanostructures [304, 305]. The surface sensitivity of TERS allows to study the distribution of In-accumulation inside the quantum well at the apex of the nanorods [304] and the gradient of Ge composition towards the surface of the nanowires [305]. The relaxation of far-field Raman selection rules is demonstrated for Ge doped GaN, graphene, and carbon nanotubes [306]. In the case of highly doped GaN, a significant increase of the intensity of the longitudinal-optical phonon-plasmon coupled (LPP) mode occurs that scales with the dopant concentration and demonstrates the importance of free carriers for the enhancement of near-field Raman scattering [306]. Three additional publications on plasmon-resonant TERS in InN, as well as In fluctuations and clustering in InGaN thin films and quantum wells studied by TERS are currently under review or being finalized. In addition, the photonic properties of few nm thin GaN quantum wires, grown on the non-polar side facets of AlN/GaN nanowire heterostructures are studied by steady-state and time-resolved micro-PL spectroscopy [307]. The intense quantum wire luminescence is a result of an efficient charge carrier transfer between the different optically active regions, feeding the quantum wire states with photo-excited charge carriers generated in the larger GaN parts of the heterostructure. The absence of electric fields due to the growth on the non-polar facets results in narrow, deep UV emission lines which are shifted to higher energies due to carrier confinement [307]. Published articles in this section include: [304–307].

4.2.3 Quantum dots

The last section of this chapter comprises articles that address the electronic and optical properties of quantum dots (QDs). The photon emission from the biexciton cascade in single GaN/AlN QDs is investigated as function of biexciton binding energy, temperature, and excitation density [308]. GaN QDs are an ideal material system for these studies since the fine-structure splitting of the excitonic bright states and the biexciton binding energy can be tuned close to zero as function of the QD dimensions. The emission process can be changed from cascaded single-photon emission to a bunched two-photon emission process as shown by the appearance of bunching around zero time delay in Hanbury-Brown and Twiss second-order correlation measurements [308]. In the case of InAs/GaAs QDs, time-resolved resonant Raman scattering experiments enable the distinction between the energetically overlapping coherent resonant Raman process and the incoherent phonon-assisted photoluminescence process which are governed by decay dynamics in the picosecond and nanosecond range, respectively [309]. In addition, the emission directionality of stacked InAs QDs is studied using 8-band $k \cdot p$ theory for QD stacks with varying barrier thickness and number of layers. The calculations reveal that the direction of emission from stacked QDs can be tuned from top emitters to edge emitters for increasing QD aspect ratio, decreasing barrier width, and increasing number of QD stacks, thus providing a framework for the design of photonic emitters based on stacked QDs [310]. Published articles in this section include: [308–310]. A more comprehensive discussion of nitride-based nanostructures is scheduled to be published in two book chapters [28, 29] which are part of a book on semiconductor nanophotonics [30]. Finally, the chapter closes with an extensive review article discussing the effects of polarity in GaN and ZnO single crystals and nanostructures [31].

5 Metal-oxide thin films and nanostructures

The final chapter comprises publications that address the optical, electronic, vibrational, and functional properties of metal-oxide thin films and nanostructures with focus on the II-VI semiconductor ZnO. Similar to the previous chapter, the first part of chapter 5 focuses on single crystals and thin films whereas the second part contains studies of a variety of different ZnO nanostructures. The applied experimental methods in these works include photoluminescence spectroscopy as function of temperature, polarization, excitation power density, uniaxial pressure, and external magnetic field strength, magneto-absorption, photoluminescence excitation (PLE), time resolved photoluminescence (TRPL), time-domain THz spectroscopy based on asynchronous optical sampling, cathodoluminescence (CL) imaging, μ-Raman scattering, Raman thermometry, nuclear magnetic resonance (NMR), and positron annihilation spectroscopy (PAS).

5.1 Excitons, phonons, and defects in ZnO thin films and single crystals

The emission and excitation spectra of ZnO near the band edge consist of a multitude of characteristic transition lines that can provide detailed information on impurities, dopants, strain, and defects. Well know features in the low-temperature emission spectra of ZnO include free- and donor bound excitons in their neutral and ionized charge states, two-electron satellites, and donor-acceptor pair transitions. In the spectral proximity of the shallow donor bound excitons, ZnO single crystals, thin films, and nanostructures commonly exhibit sharp exciton-like emission lines of ambiguous origin. Using a variety of complementary spectroscopic techniques, these transitions are identified as excitons bound to structural defect complexes which introduce additional donor states [311]. It is demonstrated that these defect-bound excitons exhibit specific characteristics such as low thermal activation energies, weak exciton-phonon coupling strength, short monoexponential decay dynamics, and small uniaxial pressure coefficients in clear distinction to the shallow donor-bound excitons in ZnO [311].

The combination of pressure-dependent photoluminescence spectroscopy, first-principle calculations based on the HSE+G_0W_0 approach, and $k \cdot p$ modeling using the deformation potential framework is applied to obtain detailed information on the stress dependence of the electronic band structure and exciton-polariton transitions in ZnO [312]. These include the zero-stress values as well as the strain and stress coefficients for the bandgap energies, valence band splittings, crystal-field splitting, and anisotropic spin-orbit coupling under uniaxial, biaxial, and hydrostatic pressure. In addition, the uniaxial stress rates are determined for the longitudinal-transverse splitting of the exciton-polaritons and their excitonic binding energies and the full set of excitonic deformation potential constants which preserve the wurtzite symmetry are derived [312]. Based on the joint experimental and theoretical study, clear evidence is found that the ordering of the topmost A(Γ_7) and B(Γ_9) valence bands in ZnO is robust even for large uniaxial and biaxial stress [312].
Further works in this section study the effects of nitrogen doping and doping induced defect formation in ZnO [313, 314]. Low-temperature photoluminescence studies of nitrogen-doped ZnO epilayers reveal pronounced differences in the optical emission spectra depending on the polarity of the growth plane [313]. Homoepitaxial growth on the non-polar a-plane or polar Zn-face of the c-plane favors the incorporation of nitrogen as acceptor as compared to the O-face of c-plane ZnO substrates [313]. Characteristic donor-acceptor pair (DAP) transitions provide evidence for the formation of shallow acceptors by amonia-doping in ZnO with an acceptor binding energy of about 160 meV. The observed shift of DAP transitions to smaller energies for nitrogen concentrations $> 5 \cdot 10^{19}$ cm^{-3} is indicative for the presence of fluctuating potentials arising from the interaction of free carriers with the electric field caused by high amounts of ionized donors and acceptors [313]. Apart from the negative ion-type defects due to the nitrogen impurities, doping of ZnO with nitrogen also results in the formation of intrinsic vacancy clusters as demonstrated by positron annihilation spectroscopy [314]. These vacancy clusters are found to be particularly stable for N-doping whereas the single Zn-vacancy defect or easy removable vacancy clusters are common for ZnO doped with other impurities [314]. Publications in this section include: [311–314]

5.2 Optical, thermal, and functional properties of ZnO nanostructures

The second part of this chapter focuses on the investigation of the optical, vibrational, thermal, and functional properties of ZnO nanostructures. Different synthesis and growth methods are applied to fabricate ZnO nanoparticles with variations in shape, size, and composition. Most investigated nanostructures are obtained using a

versatile organometallic ZnO precursor involving a tetrameric methyl-zinc-alkoxide with heterocubane structure (Zn_4O_4) [315]. Due to its good solubility, a wide variety of solvents can be used to synthesize ZnO nanostructures from colloidal solutions with specific geometrical and functional properties. Control over the nanoparticle shape is achieved using different emulsification agents which determine the main growth direction of the ZnO particles [316]. Using this approach a variety of different morphologies could be obtained using the same precursor system. These include elongated ZnO nanocrystals with prismatic morphology [315], hollow, yolk-shell, mesoporous, and solid nanospheres [316–318], lithium doped ZnO nanoparticles and nanorods [319, 320], anisotropic halogen [321] and europium [316] doped ZnO nanoparticles, and Al doped porous aerogel-like nanoparticles [322]. In addition nominally undoped as well as carbon and hydrogen doped ZnO nanowires are grown by a catalyst-free vapor-solid process [323] and metalorganic vapor phase epitaxy (MOCVD) [324]. The different nanostructures exhibit large differences in their functional properties caused by variations in the surface-to-volume ratio, elongation in polar and non-polar directions, dopant concentration, electrical, and thermal conductivity. The following examples provide a compressed summary of the specific properties of these nanostructures.

In the case of ZnO nanoprisms, a tuning of the absorption edge to lower energies could be achieved as demonstrated by PL and absorption spectroscopy [315]. This effect is not related to bandgap engineering by alloying but rather a direct consequence of the specific morphology of the nanoprisms, which are terminated by the polar [002] face. Changing the elongation of the anisotropic nanoprisms changes the electric field strength between the Zn^{2+} and O^{2-} terminated facets and thus reduces the optical bandgap by up to 200 meV [315]. Bandgap engineering of ZnO synthesized from molecular precursors is also obtained in spherical nanoparticles of the ternary $ZnO_{1-x}S_x$ alloy. As the material synthesis is performed at temperatures insufficient to overcome the diffusion barriers in the solid state, precise control of the sulfur concentration even beyond the thermodynamic solubility limit is possible [317]. Thus, a reduction of the optical bandgap by up to 700 meV could be achieved [317]. Furthermore, the thermal properties of nominally undoped ZnO nanospheres with different morphologies are studied. In particular, hollow ZnO nanospheres are identified as promising candidates for thermoelectrics as they possess an exceptionally low thermal conductivity which is reduced by two orders of magnitude as compared to bulk ZnO, while maintaining sufficient electrical conductivity [318].

Apart from the previously discussed nominally undoped ZnO nanostructures, several works focus on the synthesis and characterization of ZnO nanoparticles with a variety of different dopants including Li [319, 320], Cl, Br, I [321], Al [322], and

Eu [316]. Building on the Zn_4O_4 precursor system, Li doping is obtained by adding lithium acetate or lithium stearate to the aqueous phase [320]. Micro-Raman spectroscopy of lithium doped ZnO nanocrystals and nanorods enables the identification of characteristic Raman modes related to local Li vibrations in the ZnO lattice [319, 320]. In combination with nuclear magnetic resonance (NMR) spectroscopy, it is shown that Li^+ occupies the Zn^{2+} position in these nanostructures while maintaining perfect crystallinity as demonstrated by high resolution transmission electronic microscopy (HRTEM). The introduction of shallow donor states results in an increased electrical conductivity and improved sensitivity when applied as chemical gas sensor [320].
Starting from the same organometallic precursors, doping of ZnO nanoparticles with the halogens chlorine, bromine, and iodine could be realized [321]. The introduction of shallow donor states that increase the free electron concentration at room temperature in Cl doped ZnO is demonstrated by the longitudinal optical phonon-plasmon mode shift observed in micro-Raman spectroscopy and confirmed by time-domain THz spectroscopy [321]. Further improvement in the detection sensitivity of gas sensors is enabled by Al doped aerogel-like ZnO [322]. Doping with Al concentrations up to 4% is achieved without any change in the ratio of Al on Zn site to Al on interstitial site with Al^{3+} substituting for Zn^{2+} being the dominant process. For higher Al concentrations, micro-Raman spectroscopy reveals a strong phonon mode broadening indicating a significant distortion of the ZnO crystal lattice. While the incorporation of Al^{3+} on Zn^{2+} lattice site reduces the effective lattice parameters due to the smaller ionic radius of Al^{3+}, the opposite effect is observed for Eu doped ZnO where Zn^{2+} substitution by larger Eu^{3+} ions result in a lattice expansion as demonstrated by a linear frequency shift of the non-polar phonon modes for Eu concentrations of up to 0.7% [316]. Moreover, the effects of carbon doping and hydrogen codoping are studied in ZnO nanowires grown by MOCVD. Temperature and excitation power-dependent steady-state and time-resolved PL measurements show clear signatures of donor-acceptor-pair transitions in the optical spectra. Based on these observations, two shallow acceptor states with binding energies of 180 meV and 130 meV are identified as the commonly observed nitrogen and defect related acceptors in ZnO [324]. Publications in this chapter include: [315–324]. Beyond these works, the effects of polarity in ZnO single crystals, thin films, and nanostructures are discussed in detail in the previously mentioned extensive review article on GaN and ZnO [31].

6 Summary

This cumulative habilitation thesis has presented an overview of my post-doctorate scientific works related to the study of phononic and photonic properties of semiconductor nanostructures. These include quasi-2D structures such as ultra-thin (suspended) films, quantum wells, and 2D phononic crystals, 1D structures including nanowires, nanorods, and quantum wires, and 0D quantum dots. It comprises publications from three of my major research topics during the past years, i.e. nanoscale thermal transport and phonon coherence, photonic and phononic properties of III-nitride semiconductors and their nanostructures, and optical, electronic, vibrational, and functional properties of ZnO nanostructures. While the discussion of the nitride and oxide related publications was limited to a compressed summary of the most essential results, a more comprehensive treatment of the experimental techniques and physical aspects of nanoscale thermal transport was presented with respect to the state-of-the art of the research field.
In order to obtain the scientific results presented within the publications of this thesis, a wide variety of experimental techniques was applied. Thus, a considerable amount of time and effort was dedicated to the conceptional design, development, and implementation of new or improved experimental techniques. In particular, two techniques shall be highlighted, which were developed, implemented, and used extensively for the publications on nanoscale thermal transport (chapters 2 and 3). These are two-laser Raman thermometry and femtosecond time-domain reflectance spectroscopy by asynchronous optical sampling. In conjunction with Brillouin light scattering, scanning thermal microscopy, and 3-omega measurements, these techniques have unraveled a multitude of information about the phononic and thermal transport properties of ultra-thin membranes and phononic crystals. Some of the scientific highlights in this topic include:

Demonstration of the tuning of coherent and non-coherent phonon regimes by short range disorder in 2D phononic crystals

It was shown that short range disorder results in a pronounced modification of the phononic properties (dispersion, coherence) in the hypersonic (GHz) range while leaving the thermal properties unaffected [55]. Based on the experimental data and theoretical modeling, a general criteria for phonon coherence as function of

roughness and disorder was derived and used to explain why the room temperature thermal conductivity in lithographically patterned structures is typical not affected by phonon coherence [55]. These findings have important ramification for novel phononic crystal based applications in RF communication technologies and optomechanics, which depend on the ability to modify the phonon dispersion relation and thus the group velocity of acoustic phonons. Using controlled levels of disorder, these results might pave the way towards a new class of disordered phononics in analogy to the already actively applied field of disordered photonics.

Tuning thermal transport in ultra-thin membranes by surface nanoscale engineering

Silicon provides an ideal platform to study the relations between structure and heat transport since its thermal conductivity can be tuned over more than 2 orders of magnitude by nanostructuring and size reduction [36, 37]. Using a combination of atomistic modeling and experiments, the origin of the thermal conductivity reduction in ultrathin suspended silicon membranes was investigated down to a thickness of 4 nm. It was shown that heat transport is mostly controlled by surface scattering where rough layers and the native oxide at the surfaces limit the mean free path of thermal phonons below 100 nm [54]. In addition, it was demonstrated that the removal of the native oxide layers by chemical processing allows to increase the thermal conductivity by more than 1 order of magnitude for ultra-thin membranes [54]. The results have important implications for the materials design of future phononic applications since they define the length scale at which nanostructuring affects thermal phonons most effectively.

Modification of the phonon dispersion relation and thermal conductivity in ultra-thin Si membrane based 2D phononic crystals

The dispersion relation and thermal properties of 2D phononic crystals made of Si membranes with different characteristic dimensions (thickness, hole spacing and hole diameter) was investigated by inelastic light scattering techniques (Brillouin light scattering and 2 laser Raman thermometry). The measured phononic crystals showed significant changes in the acoustic phonon propagation due to Bragg scattering with respect to the Si membrane. The symmetry, localization and polarization of the acoustic modes in the phononic crystals was successfully modeled using finite element method (FEM) simulations [160]. Moreover, it was shown that thermal properties of the phononic crystals can be tuned in a simple and efficient manner by changing the neck size between the holes of the phononic crystal lattice [56]. The thermal conductivity in the phononic crystals can be reduced at best by a factor of

40 with respect to the value of bulk Si at room temperature. It thereby approaches the amorphous limit of Si while maintaining a feature size that is significantly larger than the electron mean free path in highly doped Si. These results are encouraging for the application of nanoscale engineered Si based structures as thermoelectric devices operating at high temperatures.

The study of nitride- and oxide-based nanostructures was conducted with a comparable variety of experimental techniques. In particular, the light emission (PL) and inelastic light scattering (Raman) processes of nanostructures were probed as function of excitation energy (resonance) and power density, polarization, temperature, magnetic field, uniaxial and hydrostatic pressure. The measurements were conducted in micro- and near-field configuration, using steady state and pulsed excitation for single photon counting, time delayed, and time-correlated spectroscopy. Selected research highlights in these topics include:

Non-destructive identification of phase segregation, clustering, and composition fluctuation in nitride-based thin films and quantum wells

InGaN/GaN heterostructures with high In content commonly experience a non-uniform In distribution resulting in the formation of local clusters and defects that increase non-radiative recombination channels and limit the performance of light emitting devices. Using tip-enhanced Raman scattering mapping, the presence of InN clusters in caped InGaN quantum wells was demonstrated by this non-destructive near-field imaging technique [304]. Additional information on strain distribution, chemical composition, polymorphism, and charge accumulation was derived by TERS mapping with a spatial resolution below 35 nm [304]. It was shown that TERS is particularly sensitive to quantum well structures with small cap layers below 5 nm and experiences a pronounced enhancement with increasing free carrier concentration [306]. Based on these observations it can be concluded that tip-enhanced Raman characterization of semiconductors with large surface charge accumulations is particularly sensitive due to a resonance enhancement with free surface charge carriers. The results are encouraging as they demonstrate the potential of tip-enhanced Raman scattering as a non-destructive, nanoscale characterization technique with great sensitivity to In-rich nitride hetero- and nanostructures.

Quantification of radiative and non-radiative recombination mechanisms in InGaN and AlGaN based LEDs and quantum wells

Closely related to the previous topic is the quantification of radiative and non-radiative recombination mechanisms in InGaN and AlGaN multi-quantum well het-

erostructures and light emitting diodes. Using small-signal time-resolved photoluminescence spectroscopy (SSTRPL), the internal quantum efficiency of InGaN LEDs was determined under operation conditions [301]. The technique enables differential carrier lifetime measurements by electrical pumping identical to operating conditions with simultaneous time-dependent quasi-resonant optical probe excitation. Using current density and temperature dependent SSTRPL measurements, the reason for the efficiency reduction of InGaN LEDs towards longer wavelength was identified as a combination of diminishing electron-hole wave function overlap due to the quantum-confined Stark effect and the increasing localization of holes, which shifts the balance between radiative and Auger recombination [301]. The efficiency droop in AlGaN quantum-well heterostructures was found to behave nearly identical to the case of InGaN QWs. The reduction of internal quantum efficiency at high excitation power densities was related to the presence of strong non-radiative Auger recombination. The results have important implications as they identify and quantify major limiting factors that need to be tackle in order to increase the efficiency of light emitters both in the InGaN and AlGaN material systems.

Electronic properties of impurity and defect bound excitons and free exciton-polaritons in ZnO and GaN

The wide bandgap semiconductors ZnO and GaN exhibit narrow emission lines at cryogenic temperatures, which are characteristic fingerprints for the presence of specific defects and impurities. Using a combination of high-resolution emission and excitation spectroscopy, detailed information on the electronic structure such as exciton localization energies, donor binding energies, electronic excited states, and charge transfer mechanisms were obtained for a variety of different defects and impurities in ZnO and GaN [294, 296, 311]. The application of external magnetic fields enabled an unambiguous identification of the donor or acceptor character of impurities and defects [311]. The combination of modern first-principle calculations based on the HSE+G_0W_0 approach, $k \cdot p$ modeling using the deformation potential framework, and polarized PL measurements as function of uniaxial and hydrostatic pressure provided detailed information on the electronic band structure of ZnO, including the spin-dependent electronic deformation potentials and the strain and stress rates for bandgap energies, exciton-polariton transition- and binding energies, crystals-field splitting, spin-orbit coupling, and exchange interaction [312]. The results have valuable implications as they contribute to the general knowledge of near-bandgap recombinations in GaN and ZnO and facilitate the identification of the chemical identify of impurities and their electronic properties by simple PL spectroscopy, provided that strain and temperature as main reasons for spectral shifts are sufficiently precise quantified.

Apart from the few selected highlights which were briefly recapitulated in this summary, a multitude of additional results were obtained including the study of the photon statistics of single GaN quantum dots [308], the observation of intense and sharp UV emission lines of non-polar GaN quantum wires with strong confinement effects [307], the tuning of the quantum confined Stark effect in polar AlN/GaN multi-quantum well structures [303], the observation of exciton-like quasi-particles in highly doped GaN which are stabilized by a three dimensional electron gas [300], the quantification of the pressure dependence of refractive indices and optical phonon transverse effective charges in InN, GaN, AlN, and ZnO [289–292] as well as detailed studies of phonons, carrier recombinations, polarity effects, and thermal conductivities in a multitude of doped and alloyed ZnO nanostructures [315–324]. For a detailed discussion, the interested reader is referred to the original publications that constitute the main work of this cumulative thesis.

7 Bibliography

[1]L. Brillouin, "Diffusion de lumière par un corps transparent homogène", Ann. Phys. **17**, 88 (1922) (cit. on p. 6).

[2]C. V. Raman, "A new radiation", Indian J. Phys. **2**, 387–398 (1928) (cit. on p. 6).

[3]D. G. Cahill, P. V. Braun, G. Chen, D. R. Clarke, S. Fan, K. E. Goodson, P. Keblinski, W. P. King, G. D. Mahan, A. Majumdar, H. J. Maris, S. R. Phillpot, E. Pop, and L. Shi, "Nanoscale thermal transport. II. 2003-2012", Applied Physics Reviews **1**, 011305 (2014) (cit. on pp. 6, 12, 32, 57).

[4]M. D. Losego, M. E. Grady, N. R. Sottos, D. G. Cahill, and P. V. Braun, "Effects of chemical bonding on heat transport across interfaces", Nature Materials **11**, 502–506 (2012) (cit. on p. 6).

[5]F. Menges, H. Riel, A. Stemmer, and B. Gotsmann, "Quantitative thermometry of nanoscale hot spots", Nano Letters **12**, 596–601 (2012) (cit. on pp. 6, 26).

[6]K. T. Regner, D. P. Sellan, Z. Su, C. H. Amon, A. J. McGaughey, and J. A. Malen, "Broadband phonon mean free path contributions to thermal conductivity measured using frequency domain thermoreflectance", Nature Communications **4**, 1640 (2013) (cit. on pp. 6, 50, 54, 55).

[7]T. Siegrist, P. Merkelbach, and M. Wuttig, "Phase Change Materials: Challenges on the Path to a Universal Storage Device", Annual Review of Condensed Matter Physics **3**, 215–237 (2012) (cit. on pp. 7, 33).

[8]B. Tian, X. Zheng, T. J. Kempa, Y. Fang, N. Yu, G. Yu, J. Huang, and C. M. Lieber, "Coaxial silicon nanowires as solar cells and nanoelectronic power sources", Nature **449**, 885–889 (2007) (cit. on pp. 7, 54).

[9]N. P. Padture, M. Gell, E. H. Jordan, Z. A. Sechrist, and S. M. George, "Thermal barrier coatings for gas-turbine engine applications", Science **296**, 280–284 (2002) (cit. on p. 7).

[10]C. Chiritescu, D. G. Cahill, N. Nguyen, D. Johnson, A. Bodapati, P. Keblinski, and P. Zschack, "Ultralow Thermal Conductivity in Disordered, Layered WSe2 Crystals", Science **315**, 351 (2007) (cit. on p. 7).

[11]R. Venkatasubramanian, E. Siivola, T. Colpitts, and B. O'Quinn, "Thin-film thermoelectric devices with high room-temperature figures of merit", Nature **413**, 597–602 (2001) (cit. on p. 7).

[12]A. I. Hochbaum, R. Chen, R. D. Delgado, W. Liang, E. C. Garnett, M. Najarian, A. Majumdar, and P. Yang, "Enhanced thermoelectric performance of rough silicon nanowires", Nature **451**, 163–167 (2008) (cit. on pp. 7, 54, 55).

[13]A. I. Boukai, Y. Bunimovich, J. Tahir-Kheli, J. K. Yu, W. A. Goddard, and J. R. Heath, "Silicon nanowires as efficient thermoelectric materials", en, Nature **451**, 168–171 (2008) (cit. on pp. 7, 41, 55).

[14]L. E. Bell, "Cooling, Heating, Generating Power, and Recovering Waste Heat with Thermoelectric Systems", Science **321**, 1457–1461 (2008) (cit. on p. 7).

[15]A. A. Balandin, S. Ghosh, W. Bao, I. Calizo, D. Teweldebrhan, F. Miao, and C. N. Lau, "Superior Thermal Conductivity of Single-Layer Graphene", Nano Letters **8**, 902–907 (2008) (cit. on pp. 7, 13).

[16]S. Ghosh, I. Calizo, D. Teweldebrhan, E. P. Pokatilov, D. L. Nika, A. A. Balandin, W. Bao, F. Miao, and C. N. Lau, "Extremely high thermal conductivity of graphene: Prospects for thermal management applications in nanoelectronic circuits", Applied Physics Letters **92**, 151911 (2008) (cit. on p. 7).

[17]A. Shchepetov, M. Prunnila, F. Alzina, L. Schneider, J. Cuffe, H. Jiang, E. I. Kauppinen, C. M. Sotomayor Torres, and J. Ahopelto, "Ultra-thin free-standing single crystalline silicon membranes with strain control", Applied Physics Letters **102**, 192108 (2013) (cit. on p. 7).

[18]K. M. F. Shahil and A. A. Balandin, "Graphene-Multilayer Graphene Nanocomposites as Highly Efficient Thermal Interface Materials", Nano Letters **12**, 861–867 (2012) (cit. on p. 7).

[19]J. B. Hertzberg, M. Aksit, O. O. Otelaja, D. A. Stewart, and R. D. Robinson, "Direct Measurements of Surface Scattering in Si Nanosheets Using a Microscale Phonon Spectrometer: Implications for Casimir-Limit Predicted by Ziman Theory", Nano Letters **14**, 403–415 (2014) (cit. on p. 7).

[20]B. Li, L. Wang, and G. Casati, "Thermal diode: Rectification of heat flux", Physical Review Letters **93**, 184301 (2004) (cit. on pp. 7, 44).

[21]M. J. Martínez-Pérez, A. Fornieri, and F. Giazotto, "Rectification of electronic heat current by a hybrid thermal diode", Nature Nanotechnology **10**, 303–307 (2015) (cit. on pp. 7, 29, 44).

[22]T. Han, X. Bai, D. Gao, J. T. Thong, B. Li, and C. W. Qiu, "Experimental demonstration of a bilayer thermal cloak", Physical Review Letters **112**, 054302 (2014) (cit. on pp. 7, 29, 44).

[23]Y. Li, X. Shen, Z. Wu, J. Huang, Y. Chen, Y. Ni, and J. Huang, "Temperature-Dependent Transformation Thermotics: From Switchable Thermal Cloaks to Macroscopic Thermal Diodes", Physical Review Letters **115**, 195503 (2015) (cit. on pp. 7, 44).

[24]S. Narayana and Y. Sato, "Heat flux manipulation with engineered thermal materials", Physical Review Letters **108**, 214303 (2012) (cit. on pp. 7, 44).

[25]H. Xu, X. Shi, F. Gao, H. Sun, and B. Zhang, "Ultrathin three-dimensional thermal cloak", Physical Review Letters **112**, 054301 (2014) (cit. on pp. 7, 29, 44).

[26]R. Anufriev, A. Ramiere, J. Maire, and M. Nomura, "Heat guiding and focusing using ballistic phonon transport in phononic nanostructures", Nature Communications **8**, 15505 (2017) (cit. on pp. 7, 29, 49, 50).

[27]D. Hatanaka, I. Mahboob, K. Onomitsu, and H. Yamaguchi, "Phonon waveguides for electromechanical circuits", Nature Nanotechnology **9**, 520–524 (2014) (cit. on p. 7).

[28]F. Bertram, C. Berger, J. Christen, H. Eisele, L. A. T. Greif, A. Hoffmann, J. Maultzsch, M. Müller, E. Poliani, G. Schmidt, P. Veit, and M. R. Wagner, "Optical and Structural Properties of Nitride based Nanostructures", in *Semiconductor nanophotonics - materials, models, devices*, edited by M. Kneissl, A. Knorr, S. Reitzenstein, and A. Hoffmann (Springer - Series in Materials Science, 2020) Chap. 5 (cit. on pp. 8, 66).

[29]G. Schmidt, C. Berger, A. Dadgar, F. Bertram, A. Strittmatter, J. Christen, S. T. Jagsch, M. R. Wagner, and A. Hoffmann, "Nitride microcavities and single quantum dots for classical and non-classical light emitters", in *Semiconductor nanophotonics - materials, models, devices*, edited by M. Kneissl, A. Knorr, S. Reitzenstein, and A. Hoffmann (Springer - Series in Materials Science, 2020) Chap. 12 (cit. on pp. 8, 66).

[30]M. Kneissl, A. Knorr, S. Reitzenstein, and A. Hoffmann, eds., *Semiconductor Nanophotonics - Materials, Models, Devices* (Springer International Publishing, 2020), p. 390 (cit. on pp. 8, 66).

[31]J. Zuñiga-Perez, V. Consonni, L. Lymperakis, X. Kong, A. Trampert, S. Fernandez-Garrido, O. Brandt, H. Renevier, S. Keller, K. Hestroffer, M. R. Wagner, J. S. Reparaz, F. Akyol, S. Rajan, S. Rennesson, T. Palacios, and G. Feuillet, "Polarity in GaN and ZnO: Theory, measurement, growth, and devices", Applied Physics Reviews **3**, 041303 (2016) (cit. on pp. 8, 10, 66, 70).

[32]J. S. Reparaz and M. R. Wagner, "Thermal Transport and Phonon Coherence in Phononic Nanostructures", in *21st century nanoscience : a handbook*, edited by K. D. Sattler (CRC Press, Taylor & Francis Group, 2019) (cit. on pp. 9, 11, 32).

[33]D. G. Cahill, "Thermal conductivity measurement from 30 to 750 K: The 3 omega method", English, Review of Scientific Instruments **61**, 802–808 (1990) (cit. on pp. 11, 23, 25).

[34]D. G. Cahill, "Analysis of heat flow in layered structures for time-domain thermoreflectance", Review of Scientific Instruments **75**, 5119–5122 (2004) (cit. on pp. 11, 16, 18, 41).

[35]A. J. Schmidt, R. Cheaito, and M. Chiesa, "A frequency-domain thermoreflectance method for the characterization of thermal properties", Review of Scientific Instruments **80**, 094901 (2009) (cit. on pp. 11, 16–18, 41).

[36]E. Chavez-Angel, J. S. Reparaz, J. Gomis-Bresco, M. R. Wagner, J. Cuffe, B. Graczykowski, A. Shchepetov, H. Jiang, M. Prunnila, J. Ahopelto, F. Alzina, and C. M. Sotomayor Torres, "Reduction of the thermal conductivity in free-standing silicon nano-membranes investigated by non-invasive Raman thermometry", APL Materials **2**, 012113 (2014) (cit. on pp. 11, 12, 14, 16, 37, 40, 41, 72).

[37]J. S. Reparaz, E. Chavez-Angel, M. R. Wagner, B. Graczykowski, J. Gomis-Bresco, F. Alzina, and C. M. Sotomayor Torres, "A novel contactless technique for thermal field mapping and thermal conductivity determination: Two-Laser Raman Thermometry", Review of Scientific Instruments **85**, 034901 (2014) (cit. on pp. 11, 13, 15, 16, 37, 40, 41, 43, 57, 72).

[38]C. C. Williams and H. K. Wickramasinghe, "Scanning thermal profiler", Applied Physics Letters **49**, 1587–1589 (1986) (cit. on pp. 11, 25).

[39]D. G. Cahill, K. E. Goodson, and A. Majumdar, "Thermometry and Thermal Transport in Micro/Nanoscale Solid-State Devices and Structures", Journal of Heat Transfer **124**, 223 (2002) (cit. on p. 12).

[40]D. G. Cahill, W. K. Ford, K. E. Goodson, G. D. Mahan, A. Majumdar, H. J. Maris, R. Merlin, and S. R. Phillpot, "Nanoscale thermal transport", Journal of Applied Physics **93**, 793–818 (2003) (cit. on pp. 12, 32).

[41]C. D. Brites, P. P. Lima, N. J. Silva, A. Millán, V. S. Amaral, F. Palacio, and L. D. Carlos, "Thermometry at the nanoscale", Nanoscale **4**, 4799–4829 (2012) (cit. on pp. 12, 26).

[42]L. Shi, "Thermal and thermoelectric transport in nanostructures and low-dimensional systems", Nanoscale and Microscale Thermophysical Engineering **16**, 79–116 (2012) (cit. on pp. 12, 32).

[43]E. S. Toberer, L. L. Baranowski, and C. Dames, "Advances in Thermal Conductivity", Annual Review of Materials Research **42**, 179–209 (2012) (cit. on pp. 12, 57).

[44]A. Weathers and L. Shi, "Thermal transport measurement techniques for nanowires and nanotubes", Annual Review of Heat Transfer **16**, 101–134 (2013) (cit. on pp. 12, 27).

[45]M. M. Rojo, O. C. Calero, A. F. Lopeandia, J. Rodriguez-Viejo, and M. Martín-Gonzalez, "Review on measurement techniques of transport properties of nanowires", Nanoscale **5**, 11526–11544 (2013) (cit. on pp. 12, 57).

[46]A. J. Minnich, "Advances in the measurement and computation of thermal phonon transport properties", Journal of Physics Condensed Matter **27**, 53202 (2015) (cit. on pp. 12, 32).

[47]K. T. Regner, J. P. Freedman, and J. A. Malen, "Advances in Studying Phonon Mean Free Path Dependent Contributions to Thermal Conductivity", Nanoscale and Microscale Thermophysical Engineering **19**, 183–205 (2015) (cit. on pp. 12, 32).

[48]D. Zhao, X. Qian, X. Gu, S. A. Jajja, and R. Yang, "Measurement Techniques for Thermal Conductivity and Interfacial Thermal Conductance of Bulk and Thin Film Materials", Journal of Electronic Packaging **138**, 040802 (2016) (cit. on p. 12).

[49]R. Heiderhoff, A. Makris, and T. Riedl, "Thermal microscopy of electronic materials", Materials Science in Semiconductor Processing **43**, 163–176 (2016) (cit. on p. 12).

[50]F. Menges, H. Riel, A. Stemmer, and B. Gotsmann, "Nanoscale thermometry by scanning thermal microscopy", Review of Scientific Instruments **87**, 074902 (2016) (cit. on pp. 12, 26, 27).

[51]K. Hippalgaonkar, J. Hun Seol, D. Xu, and D. Li, "Experimental Studies of Thermal Transport in Nanostructures", in *Thermal transport in carbon-based nanomaterials* (Elsevier, 2017), pp. 319–357 (cit. on p. 12).

[52]P. Jiang, X. Qian, and R. Yang, "Tutorial: Time-domain thermoreflectance (TDTR) for thermal property characterization of bulk and thin film materials", Journal of Applied Physics **124**, 161103 (2018) (cit. on pp. 12, 18, 19).

[53]S. Volz, J. Ordonez-Miranda, A. Shchepetov, M. Prunnila, J. Ahopelto, T. Pezeril, G. Vaudel, V. Gusev, P. Ruello, E. M. Weig, M. Schubert, M. Hettich, M. Grossman, T. Dekorsy, F. Alzina, B. Graczykowski, E. Chavez-Angel, J. Sebastian Reparaz, M. R. Wagner, C. M. Sotomayor-Torres, S. Xiong, S. Neogi, and

D. Donadio, "Nanophononics: state of the art and perspectives", The European Physical Journal B **89**, 15 (2016) (cit. on pp. 12, 36, 37, 40).

[54]S. Neogi, J. S. Reparaz, L. F. C. Pereira, B. Graczykowski, M. R. Wagner, M. Sledzinska, A. Shchepetov, M. Prunnila, J. Ahopelto, C. M. Sotomayor-Torres, and D. Donadio, "Tuning Thermal Transport in Ultrathin Silicon Membranes by Surface Nanoscale Engineering", ACS Nano **9**, 3820 (2015) (cit. on pp. 13, 16, 21, 37, 40–43, 54, 72).

[55]M. R. Wagner, B. Graczykowski, J. S. Reparaz, A. El Sachat, M. Sledzinska, F. Alzina, and C. M. Sotomayor Torres, "Two-Dimensional Phononic Crystals: Disorder Matters", Nano Letters **16**, 5661 (2016) (cit. on pp. 13, 21, 36–40, 43, 44, 46, 54, 71, 72).

[56]B. Graczykowski, A. El Sachat, J. S. Reparaz, M. Sledzinska, M. R. Wagner, E. Chavez-Angel, Y. Wu, S. Volz, Y. Wu, F. Alzina, and C. M. Sotomayor Torres, "Thermal conductivity and air-mediated losses in periodic porous silicon membranes at high temperatures", Nature Communications **8**, 415 (2017) (cit. on pp. 13, 16, 41, 43, 72).

[57]A. J. Schmidt, X. Chen, and G. Chen, "Pulse accumulation, radial heat conduction, and anisotropic thermal conductivity in pump-probe transient thermoreflectance", Review of Scientific Instruments **79**, 114902 (2008) (cit. on p. 16).

[58]J. Zhu, D. Tang, W. Wang, J. Liu, K. W. Holub, and R. Yang, "Ultrafast thermoreflectance techniques for measuring thermal conductivity and interface thermal conductance of thin films", Journal of Applied Physics **108**, 094315 (2010) (cit. on p. 16).

[59]J. A. Malen, K. Baheti, T. Tong, Y. Zhao, J. A. Hudgings, and A. Majumdar, "Optical Measurement of Thermal Conductivity Using Fiber Aligned Frequency Domain Thermoreflectance", Journal of Heat Transfer **133**, 081601 (2011) (cit. on p. 16).

[60]C. Thomsen, J. Strait, Z. Vardeny, H. J. Maris, J. Tauc, and J. J. Hauser, "Coherent phonon generation and detection by picosecond light pulses", Physical Review Letters **53**, 989–992 (1984) (cit. on p. 20).

[61]C. Thomsen, H. T. Grahn, H. J. Maris, and J. Tauc, "Surface generation and detection of phonons by picosecond light pulses", Physical Review B **34**, 4129–4138 (1986) (cit. on pp. 20, 38).

[62]M. Harb, W. Peng, G. Sciaini, C. T. Hebeisen, R. Ernstorfer, M. A. Eriksson, M. G. Lagally, S. G. Kruglik, and R. J. D. Miller, "Excitation of longitudinal and transverse coherent acoustic phonons in nanometer free-standing films of (001) Si", Physical Review B **79**, 094301 (2009) (cit. on p. 20).

[63]M. Hettich, K. Jacob, O. Ristow, C. He, J. Mayer, M. Schubert, V. Gusev, A. Bruchhausen, and T. Dekorsy, "Imaging of a patterned and buried molecular layer by coherent acoustic phonon spectroscopy", Applied Physics Letters **101**, 191606 (2012) (cit. on pp. 20, 22).

[64]A. M. Lomonosov, A. Ayouch, P. Ruello, G. Vaudel, M. R. Baklanov, P. Verdonck, L. Zhao, and V. E. Gusev, "Nanoscale Noncontact Subsurface Investigations of Mechanical and Optical Properties of Nanoporous Low- k Material Thin Film", ACS Nano **6**, 1410–1415 (2012) (cit. on p. 20).

[65]K. Ishioka, A. Rustagi, A. Beyer, W. Stolz, K. Volz, U. Höfer, H. Petek, and C. J. Stanton, "Sub-picosecond acoustic pulses at buried GaP/Si interfaces", Applied Physics Letters **111**, 62105 (2017) (cit. on p. 20).

[66]Laserquantum.com, *Sub-nm layer measurements using ASOPS and laser induced ultrasound*, 2015 (cit. on p. 21).

[67]P. A. Elzinga, R. J. Kneisler, F. E. Lytle, Y. Jiang, G. B. King, and N. M. Laurendeau, "Pump/probe method for fast analysis of visible spectral signatures utilizing asynchronous optical sampling", Applied Optics **26**, 4303 (1987) (cit. on p. 21).

[68]C. Janke, M. Först, M. Nagel, H. Kurz, and A. Bartels, "Asynchronous optical sampling for high-speed characterization of integrated resonant terahertz sensors", Optics Letters **30**, 1405 (2005) (cit. on p. 21).

[69]A. Bartels, F. Hudert, C. Janke, T. Dekorsy, and K. Köhler, "Femtosecond time resolved optical pump probe spectroscopy at kilohertz scan rates over nanosecond time delays without mechanical delay line", Applied Physics Letters **88**, 041117 (2006) (cit. on p. 21).

[70]A. Bartels, R. Cerna, C. Kistner, A. Thoma, F. Hudert, C. Janke, and T. Dekorsy, "Ultrafast time-domain spectroscopy based on high-speed asynchronous optical sampling", Review of Scientific Instruments **78**, 035107 (2007) (cit. on pp. 21, 38).

[71]A. Bruchhausen, R. Gebs, F. Hudert, D. Issenmann, G. Klatt, A. Bartels, O. Schecker, R. Waitz, A. Erbe, E. Scheer, J. R. Huntzinger, A. Mlayah, and T. Dekorsy, "Subharmonic resonant optical excitation of confined acoustic modes in a free-standing semiconductor membrane at GHz frequencies with a high-repetition-rate femtosecond laser", Physical Review Letters **106**, 77401 (2011) (cit. on pp. 21, 38).

[72]A. Bruchhausen, M. Hettich, R. Gebs, M. Grossmann, O. Ristow, A. Bartels, T. Dekorsy, J. Lloyd-Hughes, M. Fischer, M. Beck, G. Scalari, J. Faist, A. Rudra, P. Gallo, and E. Kapon, "Investigation of coherent acoustic phonons in terahertz quantum cascade laser structures using femtosecond pump-probe spectroscopy", Journal of Applied Physics **112**, 033517 (2012) (cit. on p. 21).

[73]R. Gebs, G. Klatt, C. Janke, T. Dekorsy, and A. Bartels, "High-speed asynchronous optical sampling with sub-50fs time resolution", Optics Express **18**, 5974 (2010) (cit. on p. 21).

[74]G. Pernot, M. Stoffel, I. Savic, F. Pezzoli, P. Chen, G. Savelli, A. Jacquot, J. Schumann, U. Denker, I. Mönch, C. Deneke, O. G. Schmidt, J. M. Rampnoux, S. Wang, M. Plissonnier, A. Rastelli, S. Dilhaire, and N. Mingo, "Precise control of thermal conductivity at the nanoscale through individual phonon-scattering barriers", Nature Materials **9**, 491–495 (2010) (cit. on pp. 21, 58).

[75]S. Dilhaire, G. Pernot, G. Calbris, J. M. Rampnoux, and S. Grauby, "Heterodyne picosecond thermoreflectance applied to nanoscale thermal metrology", Journal of Applied Physics **110**, 114314 (2011) (cit. on p. 21).

[76]J. Cuffe, O. Ristow, E. Chávez, A. Shchepetov, P. O. Chapuis, F. Alzina, M. Hettich, M. Prunnila, J. Ahopelto, T. Dekorsy, and C. M. Sotomayor Torres, "Lifetimes of confined acoustic phonons in ultrathin silicon membranes", Physical Review Letters **110**, 095503 (2013) (cit. on pp. 21, 38–40).

[77]P. O. Vaccaro, M. I. Alonso, M. Garriga, J. Gutiérrez, D. Peró, M. R. Wagner, J. S. Reparaz, C. M. Sotomayor Torres, X. Vidal, E. A. Carter, P. A. Lay, M. Yoshimoto, and A. R. Goñi, "Localized thinning for strain concentration in suspended germanium membranes and optical method for precise thickness measurement", AIP Advances **8**, 115131 (2018) (cit. on pp. 21, 39, 43).

[78]A. Schliesser, N. Picqué, and T. W. Hänsch, "Mid-infrared frequency combs", Nature Photonics **6**, 440–449 (2012) (cit. on p. 22).

[79]T. Yasui, E. Saneyoshi, and T. Araki, "Asynchronous optical sampling terahertz time-domain spectroscopy for ultrahigh spectral resolution and rapid data acquisition", Applied Physics Letters **87**, 061101 (2005) (cit. on p. 22).

[80]G. Klatt, R. Gebs, H. Schäfer, M. Nagel, C. Janke, A. Bartels, and T. Dekorsy, "High-resolution terahertz spectrometer", IEEE Journal of Selected Topics in Quantum Electronics **17**, 159–168 (2011) (cit. on p. 22).

[81]T. Yasui, K. Kawamoto, Y.-d. Hsieh, Y. Sakaguchi, M. Jewariya, H. Inaba, K. Minoshima, F. Hindle, and T. Araki, "Enhancement of spectral resolution and accuracy in asynchronous-optical-sampling terahertz time-domain spectroscopy

for low-pressure gas-phase analysis", Optics Express **20**, 15071 (2012) (cit. on p. 22).

[82]A. Abbas, Y. Guillet, J.-M. Rampnoux, P. Rigail, E. Mottay, B. Audoin, and S. Dilhaire, "Picosecond time resolved opto-acoustic imaging with 48 MHz frequency resolution", Optics Express **22**, 7831 (2014) (cit. on p. 22).

[83]O. Kliebisch, D. C. Heinecke, and T. Dekorsy, "Ultrafast time-domain spectroscopy system using 10 GHz asynchronous optical sampling with 100 kHz scan rate", Optics Express **24**, 29930 (2016) (cit. on p. 22).

[84]Y. Guillet, A. Abbas, S. Ravaine, and B. Audoin, "Ultrafast microscopy of the vibrational landscape of a single nanoparticle", Applied Physics Letters **114**, 091904 (2019) (cit. on p. 22).

[85]B. F. Spencer, W. F. Smith, M. T. Hibberd, P. Dawson, M. Beck, A. Bartels, I. Guiney, C. J. Humphreys, and D. M. Graham, "Terahertz cyclotron resonance spectroscopy of an AlGaN/GaN heterostructure using a high-field pulsed magnet and an asynchronous optical sampling technique", Applied Physics Letters **108**, 212101 (2016) (cit. on p. 22).

[86]H. Guerboukha, K. Nallappan, and M. Skorobogatiy, "Toward real-time terahertz imaging", Advances in Optics and Photonics **10**, 843–938 (2018) (cit. on p. 22).

[87]H. S. Carslaw and J. C. Jaeger, *Conduction of Heat in Solids* (Oxford University Press, 1959), p. 111 (cit. on p. 23).

[88]T. Borca-Tasciuc, A. R. Kumar, and G. Chen, "Data reduction in 3ω method for thin-film thermal conductivity determination", Review of Scientific Instruments **72**, 2139–2147 (2001) (cit. on p. 25).

[89]B. W. Olson, S. Graham, and K. Chen, "A practical extension of the 3ω method to multilayer structures", Review of Scientific Instruments **76**, 053901 (2005) (cit. on p. 25).

[90]J. Ordonez-Miranda, M. Hermens, I. Nikitin, V. G. Kouznetsova, O. van der Sluis, M. A. Ras, J. S. Reparaz, M. R. Wagner, M. Sledzinska, J. Gomis-Bresco, C. M. Sotomayor Torres, B. Wunderle, and S. Volz, "Measurement and modeling of the effective thermal conductivity of sintered silver pastes", International Journal of Thermal Sciences **108**, 185 (2016) (cit. on p. 25).

[91]K. Kim, W. Jeong, W. Lee, and P. Reddy, "Ultra-high vacuum scanning thermal microscopy for nanometer resolution quantitative thermometry", ACS Nano **6**, 4248–4257 (2012) (cit. on pp. 25, 26).

[92]A. Majumdar, J. Lai, M. Chandrachood, O. Nakabeppu, Y. Wu, and Z. Shi, "Thermal imaging by atomic force microscopy using thermocouple cantilever probes", Review of Scientific Instruments **66**, 3584–3592 (1995) (cit. on p. 26).

[93]L. Aigouy, G. Tessier, M. Mortier, and B. Charlot, "Scanning thermal imaging of microelectronic circuits with a fluorescent nanoprobe", Applied Physics Letters **87**, 184105 (2005) (cit. on p. 26).

[94]Y. De Wilde, F. Formanek, R. Carminati, B. Gralak, P. A. Lemoine, K. Joulain, J. P. Mulet, Y. Chen, and J. J. Greffet, "Thermal radiation scanning tunnelling microscopy", Nature **444**, 740–743 (2006) (cit. on p. 26).

[95]S. Sadat, A. Tan, Y. J. Chua, and P. Reddy, "Nanoscale thermometry using point contact thermocouples", Nano Letters **10**, 2613–2617 (2010) (cit. on p. 26).

[96]M. E. Pumarol, M. C. Rosamond, P. Tovee, M. C. Petty, D. A. Zeze, V. Falko, and O. V. Kolosov, "Direct nanoscale imaging of ballistic and diffusive thermal transport in graphene nanostructures", Nano Letters **12**, 2906–2911 (2012) (cit. on p. 26).

[97]F. Menges, P. Mensch, H. Schmid, H. Riel, A. Stemmer, and B. Gotsmann, "Temperature mapping of operating nanoscale devices by scanning probe thermometry", Nature Communications **7**, 10874 (2016) (cit. on p. 26).

[98]Y. Yue and X. Wang, "Nanoscale thermal probing", Nano Reviews **3**, 11586 (2012) (cit. on p. 26).

[99]W. Jeong, S. Hur, E. Meyhofer, and P. Reddy, "Scanning Probe Microscopy for Thermal Transport Measurements", Nanoscale and Microscale Thermophysical Engineering **19**, 279–302 (2015) (cit. on pp. 26, 27).

[100]S. Gomès, A. Assy, and P.-O. Chapuis, "Scanning thermal microscopy: A review", physica status solidi (a) **212**, 477–494 (2015) (cit. on pp. 26, 27).

[101]J. Spièce, *Quantitative mapping of nanothermal transport via Scanning Thermal Microscopy* (Springer Nature Switzerland AG, 2019), p. 225 (cit. on pp. 26, 27).

[102]T. Borca-Tasciuc, "Scanning probe methods for thermal and thermoelectric property measurements", Annual Review of Heat Transfer **16**, 211–258 (2013) (cit. on p. 26).

[103]J. Martinek, P. Klapetek, and A. C. Campbell, "Methods for topography artifacts compensation in scanning thermal microscopy", Ultramicroscopy **155**, 55–61 (2015) (cit. on p. 26).

[104]A. E. Sachat, J. S. Reparaz, J. Spiece, M. I. Alonso, A. R. Goñi, M. Garriga, P. O. Vaccaro, M. R. Wagner, O. V. Kolosov, C. M. Sotomayor Torres, and F. Alzina, "Thermal transport in epitaxial SiGe alloy nanowires with varying composition and morphology", Nanotechnology **28**, 505704 (2017) (cit. on pp. 26, 27, 57).

[105]K. Kim, W. Jeong, W. Lee, S. Sadat, D. Thompson, E. Meyhofer, and P. Reddy, "Quantification of thermal and contact resistances of scanning thermal probes", Applied Physics Letters **105**, 203107 (2014) (cit. on p. 27).

[106]L. Shi, D. Li, C. Yu, W. Jang, D. Kim, Z. Yao, P. Kim, and A. Majumdar, "Measuring Thermal and Thermoelectric Properties of One-Dimensional Nanostructures Using a Microfabricated Device", Journal of Heat Transfer **125**, 881 (2003) (cit. on pp. 27, 57).

[107]J. W. Roh, K. Hippalgaonkar, J. H. Ham, R. Chen, M. Z. Li, P. Ercius, A. Majumdar, W. Kim, and W. Lee, "Observation of anisotropy in thermal conductivity of individual single-crystalline bismuth nanowires", ACS Nano **5**, 3954–3960 (2011) (cit. on p. 27).

[108]Z. Wang, R. Xie, C. T. Bui, D. Liu, X. Ni, B. Li, and J. T. Thong, "Thermal transport in suspended and supported few-layer graphene", Nano Letters **11**, 113–118 (2011) (cit. on p. 27).

[109]M. C. Wingert, Z. C. Y. Chen, S. Kwon, J. Xiang, and R. Chen, "Ultra-sensitive thermal conductance measurement of one-dimensional nanostructures enhanced by differential bridge", Review of Scientific Instruments **83**, 024901 (2012) (cit. on p. 27).

[110]J. Zheng, M. C. Wingert, E. Dechaumphai, and R. Chen, "Sub-picowatt/kelvin resistive thermometry for probing nanoscale thermal transport", Review of Scientific Instruments **84**, 114901 (2013) (cit. on p. 28).

[111]S. Sadat, E. Meyhofer, and P. Reddy, "High resolution resistive thermometry for micro/nanoscale measurements", Review of Scientific Instruments **83**, 084902 (2012) (cit. on p. 28).

[112]S. Sadat, E. Meyhofer, and P. Reddy, "Resistance thermometry-based picowatt-resolution heat-flow calorimeter", Applied Physics Letters **102**, 163110 (2013) (cit. on p. 28).

[113]C. Yu, L. Shi, Z. Yao, D. Li, and A. Majumdar, "Thermal conductance and thermopower of an individual single-wall carbon nanotube", Nano Letters **5**, 1842–1846 (2005) (cit. on p. 28).

[114]I. K. Hsu, M. T. Pettes, A. Bushmaker, M. Aykol, L. Shi, and S. B. Cronin, "Optical absorption and thermal transport of individual suspended carbon nanotube bundles", Nano Letters **9**, 590–594 (2009) (cit. on p. 28).

[115]M. T. Pettes and L. Shi, "Thermal and structural characterizations of individual single-, double-, and multi-walled carbon nanotubes", Advanced Functional Materials **19**, 3918–3925 (2009) (cit. on p. 28).

[116]I. Jo, M. T. Pettes, J. Kim, K. Watanabe, T. Taniguchi, Z. Yao, and L. Shi, "Thermal conductivity and phonon transport in suspended few-layer hexagonal boron nitride", Nano Letters **13**, 550–554 (2013) (cit. on p. 28).

[117]J. H. Seol, I. Jo, A. L. Moore, L. Lindsay, Z. H. Aitken, M. T. Pettes, X. Li, Z. Yao, R. Huang, D. Broido, N. Mingo, R. S. Ruoff, and L. Shi, "Two-dimensional phonon transport in supported graphene", Science **328**, 213–216 (2010) (cit. on p. 28).

[118]S. Lee, F. Yang, J. Suh, S. Yang, Y. Lee, G. Li, H. Sung Choe, A. Suslu, Y. Chen, C. Ko, J. Park, K. Liu, J. Li, K. Hippalgaonkar, J. J. Urban, S. Tongay, and J. Wu, "Anisotropic in-plane thermal conductivity of black phosphorus nanoribbons at temperatures higher than 100 K", Nature Communications **6**, 8573 (2015) (cit. on p. 28).

[119]D. Li, Y. Wu, P. Kim, L. Shi, P. Yang, and A. Majumdar, "Thermal conductivity of individual silicon nanowires", Applied Physics Letters **83**, 2934–2936 (2003) (cit. on p. 28).

[120]A. I. Boukai, Y. Bunimovich, J. Tahir-Kheli, J. K. Yu, W. A. Goddard, and J. R. Heath, "Silicon nanowires as efficient thermoelectric materials", Nature **451**, 168–171 (2008) (cit. on p. 28).

[121]C. Guthy, C.-Y. Nam, and J. E. Fischer, "Unusually low thermal conductivity of gallium nitride nanowires", Journal of Applied Physics **103**, 064319 (2008) (cit. on p. 28).

[122]A. Mavrokefalos, A. L. Moore, M. T. Pettes, L. Shi, W. Wang, and X. Li, "Thermoelectric and structural characterizations of individual electrodeposited bismuth telluride nanowires", Journal of Applied Physics **105**, 104318 (2009) (cit. on p. 28).

[123]J. W. Roh, S. Y. Jang, J. Kang, S. Lee, J.-S. Noh, W. Kim, J. Park, and W. Lee, "Size-dependent thermal conductivity of individual single-crystalline PbTe nanowires", Applied Physics Letters **96**, 103101 (2010) (cit. on p. 28).

[124]T. K. Hsiao, H. K. Chang, S. C. Liou, M. W. Chu, S. C. Lee, and C. W. Chang, "Observation of room erature ballistic thermal conduction persisting over 8.3 μm in SiGe nanowires", Nature Nanotechnology **8**, 534–538 (2013) (cit. on pp. 28, 49, 56, 57).

[125]T.-K. Hsiao, B.-W. Huang, H.-K. Chang, S.-C. Liou, M.-W. Chu, S.-C. Lee, and C.-W. Chang, "Micron-scale ballistic thermal conduction and suppressed thermal conductivity in heterogeneously interfaced nanowires", Physical Review B **91**, 035406 (2015) (cit. on pp. 28, 56, 57).

[126]J. Kim, E. Ou, D. P. Sellan, and L. Shi, "A four-probe thermal transport measurement method for nanostructures", Review of Scientific Instruments **86**, 044901 (2015) (cit. on p. 28).

[127]K. Vahala, M. Herrmann, S. Knünz, V. Batteiger, G. Saathoff, T. W. Hänsch, and T. Udem, "A phonon laser", Nature Physics **5**, 682–686 (2009) (cit. on p. 29).

[128]J. Zhang, B. Peng, Ş. K. Özdemir, K. Pichler, D. O. Krimer, G. Zhao, F. Nori, Y. xi Liu, S. Rotter, and L. Yang, "A phonon laser operating at an exceptional point", Nature Photonics **12**, 479–484 (2018) (cit. on p. 29).

[129]A. Sood, F. Xiong, S. Chen, H. Wang, D. Selli, J. Zhang, C. J. McClellan, J. Sun, D. Donadio, Y. Cui, E. Pop, and K. E. Goodson, "An electrochemical thermal transistor", Nature Communications **9**, 4510 (2018) (cit. on p. 29).

[130]S. Huberman, R. A. Duncan, K. Chen, B. Song, V. Chiloyan, Z. Ding, A. A. Maznev, G. Chen, and K. A. Nelson, "Observation of second sound in graphite at temperatures above 100 K", Science **364**, 375–379 (2019) (cit. on pp. 29, 61).

[131]M. N. Luckyanova, J. Garg, K. Esfarjani, A. Jandl, M. T. Bulsara, A. J. Schmidt, A. J. Minnich, S. Chen, M. S. Dresselhaus, Z. Ren, E. A. Fitzgerald, and G. Chen, "Coherent Phonon Heat Conduction in Superlattices", Science **338**, 936–939 (2012) (cit. on pp. 29, 51, 52).

[132]J. Ravichandran, A. K. Yadav, R. Cheaito, P. B. Rossen, A. Soukiassian, S. J. Suresha, J. C. Duda, B. M. Foley, C.-h. H. Lee, Y. Zhu, A. W. Lichtenberger, J. E. Moore, D. A. Muller, D. G. Schlom, P. E. Hopkins, A. Majumdar, R. Ramesh, and M. A. Zurbuchen, "Crossover from incoherent to coherent phonon scattering in epitaxial oxide superlattices", Nature Materials **13**, 168–172 (2014) (cit. on pp. 29, 51–53).

[133]J. Liu, G.-M. Choi, and D. G. Cahill, "Measurement of the anisotropic thermal conductivity of molybdenum disulfide by the time-resolved magneto-optic Kerr effect", Journal of Applied Physics **116**, 233107 (2014) (cit. on pp. 29, 30).

[134]J. Y. Chen, J. Zhu, D. Zhang, D. M. Lattery, M. Li, J. P. Wang, and X. Wang, "Time-Resolved Magneto-Optical Kerr Effect of Magnetic Thin Films for Ultrafast Thermal Characterization", Journal of Physical Chemistry Letters **7**, 2328–2332 (2016) (cit. on p. 29).

[135]J. Kimling, A. Philippi-Kobs, J. Jacobsohn, H. P. Oepen, and D. G. Cahill, "Thermal conductance of interfaces with amorphous ¡math¿ ¡msub¿ ¡mi mathvariant="bold"¿SiO¡/mi¿ ¡mn¿2¡/mn¿ ¡/msub¿ ¡/math¿ measured by time-resolved magneto-optic Kerr-effect thermometry", Physical Review B **95**, 184305 (2017) (cit. on pp. 29, 30).

[136]R. B. Wilson and D. G. Cahill, "Anisotropic failure of Fourier theory in time-domain thermoreflectance experiments", Nature Communications **5**, 1–11 (2014) (cit. on pp. 30, 49).

[137]J. P. Feser, J. Liu, and D. G. Cahill, "Pump-probe measurements of the thermal conductivity tensor for materials lacking in-plane symmetry", Review of Scientific Instruments **85**, 104903 (2014) (cit. on p. 30).

[138]J. P. Feser and D. G. Cahill, "Probing anisotropic heat transport using time-domain thermoreflectance with offset laser spots", Review of Scientific Instruments **83**, 104901 (2012) (cit. on p. 30).

[139]J. Zhu, H. Park, J.-Y. Chen, X. Gu, H. Zhang, S. Karthikeyan, N. Wendel, S. A. Campbell, M. Dawber, X. Du, M. Li, J.-P. Wang, R. Yang, and X. Wang, "Revealing the Origins of 3D Anisotropic Thermal Conductivities of Black Phosphorus", Advanced Electronic Materials **2**, 1600040 (2016) (cit. on p. 30).

[140]R. Landauer, "Irreversibility and Heat Generation in the Computing Process", IBM Journal of Research and Development **5**, 183–191 (1961) (cit. on p. 30).

[141]A. Bérut, A. Arakelyan, A. Petrosyan, S. Ciliberto, R. Dillenschneider, and E. Lutz, "Experimental verification of Landauer's principle linking information and thermodynamics", Nature **483**, 187–189 (2012) (cit. on p. 30).

[142]J. P. Pekola, "Towards quantum thermodynamics in electronic circuits", Nature Physics **11**, 118–123 (2015) (cit. on p. 30).

[143]D. Halbertal, J. Cuppens, M. B. Shalom, L. Embon, N. Shadmi, Y. Anahory, H. R. Naren, J. Sarkar, A. Uri, Y. Ronen, Y. Myasoedov, L. S. Levitov, E. Joselevich, A. K. Geim, and E. Zeldov, "Nanoscale thermal imaging of dissipation in quantum systems", Nature **539**, 407–410 (2016) (cit. on pp. 30, 31, 58).

[144]D. Halbertal, M. B. Shalom, A. Uri, K. Bagani, A. Y. Meltzer, I. Marcus, Y. Myasoedov, J. Birkbeck, L. S. Levitov, A. K. Geim, and E. Zeldov, "Imaging resonant dissipation from individual atomic defects in graphene", Science **358**, 1303–1306 (2017) (cit. on pp. 31, 58).

[145]N. Yang, X. Xu, G. Zhang, and B. Li, "Thermal transport in nanostructures", AIP Advances **2**, 041410 (2012) (cit. on p. 32).

[146]T. Luo and G. Chen, "Nanoscale heat transfer - from computation to experiment", Physical Chemistry Chemical Physics **15**, 3389 (2013) (cit. on p. 32).

[147]P. A. Deymier, *Acoustic Metamaterials and Phononic Crystals*, Vol. 173 (Springer, Berlin, Heidelberg, 2013), pp. 1–378 (cit. on p. 32).

[148]Y. Guo and M. Wang, "Phonon hydrodynamics and its applications in nanoscale heat transport", Physics Reports **595**, 1–44 (2015) (cit. on p. 32).

[149]W. Kim, "Strategies for engineering phonon transport in thermoelectrics", Journal of Materials Chemistry C **3**, 10336–10347 (2015) (cit. on p. 32).

[150]Z. Xu, "Heat transport in low-dimensional materials: A review and perspective", Theoretical and Applied Mechanics Letters **6**, 113–121 (2016) (cit. on pp. 32, 43).

[151]G. Xie, D. Ding, and G. Zhang, "Phonon coherence and its effect on thermal conductivity of nanostructures", Advances in Physics: X **3**, 1480417 (2018) (cit. on p. 32).

[152]M. I. Hussein, C.-N. Tsai, and H. Honarvar, "Thermal Conductivity Reduction in a Nanophononic Metamaterial versus a Nanophononic Crystal: A Review and Comparative Analysis", Advanced Functional Materials **2019**, 1906718 (2019) (cit. on p. 32).

[153]M. Maldovan, "Sound and heat revolutions in phononics", Nature **503**, 209–217 (2013) (cit. on pp. 35, 37, 44).

[154]M. Maldovan, "Phonon wave interference and thermal bandgap materials", Nature Materials **14**, 667–674 (2015) (cit. on pp. 35, 44, 54).

[155]E. Yablonovitch, "Inhibited spontaneous emission in solid-state physics and electronics", Physical Review Letters **58**, 2059–2062 (1987) (cit. on pp. 35, 44).

[156]S. John, "Strong localization of photons in certain disordered dielectric superlattices", Physical Review Letters **58**, 2486–2489 (1987) (cit. on pp. 35, 44).

[157]S. Fan, P. R. Villeneuve, J. D. Joannopoulos, and E. F. Schubert, "High extraction efficiency of spontaneous emission from slabs of photonic crystals", Physical Review Letters **78**, 3294–3297 (1997) (cit. on p. 35).

[158]P. R. Villeneuve, S. Fan, S. G. Johnson, and J. D. Joannopouios, "Three-dimensional photon confinement in photonic crystals of low-dimensional periodicity", IEE Proceedings: Optoelectronics **145**, 384–390 (1998) (cit. on p. 35).

[159]S. Noda, M. Yokoyama, M. Imada, A. Chutinan, and M. Mochizuki, "Polarization mode control of two-dimensional photonic crystal laser by unit cell structure design", Science **293**, 1123–1125 (2001) (cit. on p. 35).

[160]B. Graczykowski, M. Sledzinska, F. Alzina, J. Gomis-Bresco, J. S. Reparaz, M. R. Wagner, and C. M. Sotomayor Torres, "Phonon dispersion in hypersonic two-dimensional phononic crystal membranes", Physical Review B **91**, 075414 (2015) (cit. on pp. 36, 37, 45, 72).

[161]F. Hudert, A. Bruchhausen, D. Issenmann, O. Schecker, R. Waitz, A. Erbe, E. Scheer, T. Dekorsy, A. Mlayah, and J.-R. Huntzinger, "Confined longitudinal acoustic phonon modes in free-standing Si membranes coherently excited by femtosecond laser pulses", Physical Review B **79**, 201307 (2009) (cit. on pp. 37–40).

[162]M. Schubert, M. Grossmann, C. He, D. Brick, P. Scheel, O. Ristow, V. Gusev, and T. Dekorsy, "Generation and detection of gigahertz acoustic oscillations in thin membranes", Ultrasonics **56**, 109–115 (2015) (cit. on pp. 37, 38, 40).

[163]J. Cuffe, E. Chávez, A. Shchepetov, P. O. Chapuis, E. H. El Boudouti, F. Alzina, T. Kehoe, J. Gomis-Bresco, D. Dudek, Y. Pennec, B. Djafari-Rouhani, M. Prunnila, J. Ahopelto, and C. M. Sotomayor Torres, "Phonons in slow motion: Dispersion relations in ultrathin Si membranes", Nano Letters **12**, 3569–3573 (2012) (cit. on p. 37).

[164]S. Bramhavar, C. Prada, A. A. Maznev, A. G. Every, T. B. Norris, and T. W. Murray, "Negative refraction and focusing of elastic Lamb waves at an interface", Physical Review B **83**, 014106 (2011) (cit. on p. 37).

[165]B. Graczykowski, J. Gomis-Bresco, F. Alzina, J. S Reparaz, A. Shchepetov, M. Prunnila, J. Ahopelto, and C. M Sotomayor Torres, "Acoustic phonon propagation in ultra-thin Si membranes under biaxial stress field", New Journal of Physics **16**, 073024 (2014) (cit. on p. 37).

[166]B. C. Daly, K. Kang, Y. Wang, and D. G. Cahill, "Picosecond ultrasonic measurements of attenuation of longitudinal acoustic phonons in silicon", Physical Review B **80**, 174112 (2009) (cit. on p. 38).

[167]J.-F. Robillard, A. Devos, I. Roch-Jeune, and P. A. Mante, "Collective acoustic modes in various two-dimensional crystals by ultrafast acoustics: Theory and experiment", Physical Review B **78**, 064302 (2008) (cit. on p. 38).

[168]V. Juvé, A. Crut, P. Maioli, M. Pellarin, M. Broyer, N. Del Fatti, and F. Vallée, "Probing elasticity at the nanoscale: Terahertz acoustic vibration of small metal nanoparticles", Nano Letters **10**, 1853–1858 (2010) (cit. on p. 38).

[169]A. Amziane, L. Belliard, F. Decremps, and B. Perrin, "Ultrafast acoustic resonance spectroscopy of gold nanostructures: Towards a generation of tunable transverse waves", Physical Review B **83**, 014102 (2011) (cit. on p. 38).

[170]C. Mechri, P. Ruello, and V. Gusev, "Confined coherent acoustic modes in a tubular nanoporous alumina film probed by picosecond acoustics methods", New Journal of Physics **14**, 023048 (2012) (cit. on p. 38).

[171]O. B. Wright and V. E. Gusev, "Acoustic generation in crystalline silicon with femtosecond optical pulses", Applied Physics Letters **66**, 1190–1192 (1995) (cit. on p. 38).

[172]C. M. Sotomayor Torres, A. Zwick, F. Poinsotte, J. Groenen, M. Prunilla, J. Ahopelto, A. Mlayah, and V. Paillard, "Observations of confined acoustic phonons in silicon membranes", Physica Status Solidi C **1**, 2609–2612 (2004) (cit. on p. 39).

[173]J. Groenen, F. Poinsotte, A. Zwick, C. M. Sotomayor Torres, M. Prunnila, and J. Ahopelto, "Inelastic light scattering by longitudinal acoustic phonons in thin silicon layers: From membranes to silicon-on-insulator structures", Physical Review B **77**, 045420 (2008) (cit. on p. 39).

[174]H. J. McSkimin and P. Andreatch, "Elastic Moduli of Silicon vs Hydrostatic Pressure at 25.0 C and -195.8 C", Journal of Applied Physics **35**, 2161–2165 (1964) (cit. on p. 40).

[175]M. Grossmann, M. Klingele, P. Scheel, O. Ristow, M. Hettich, C. He, R. Waitz, M. Schubert, A. Bruchhausen, V. Gusev, E. Scheer, and T. Dekorsy, "Femtosecond spectroscopy of acoustic frequency combs in the 100-GHz frequency range in Al/Si membranes", Physical Review B **88**, 205202 (2013) (cit. on p. 40).

[176]L. Landau and G. Rumer, "On the Absorption of Sound in Solids", Phys. Z. Sowjet **11**, 18 (1937) (cit. on p. 40).

[177]A. Akhieser, "On the Absorption of Sound in Solids", J. Phys. USSR **1**, 277 (1939) (cit. on p. 40).

[178]J. Ziman, *Electrons and Phonons: The Theory of Transport Phenomena in Solids. Oxford Classic Texts in the Physical Sciences* (Clarendon Press, 1960), p. 554 (cit. on p. 40).

[179]M. Zebarjadi, K. Esfarjani, M. S. Dresselhaus, Z. F. Ren, and G. Chen, "Perspectives on thermoelectrics: From fundamentals to device applications", en, Energy and Environmental Science **5**, 5147–5162 (2012) (cit. on p. 41).

[180]F. P. Incropera, D. P. DeWitt, T. L. Bergman, and A. S. Lavine, *Fundamentals of heat and mass transfer* (Wiley, 2011), p. 1048 (cit. on p. 41).

[181]M. Asheghi, Y. K. Leung, S. S. Wong, and K. E. Goodson, "Phonon-boundary scattering in thin silicon layers", Applied Physics Letters **71**, 1798–1800 (1997) (cit. on p. 41).

[182]Y. S. Ju and K. E. Goodson, "Phonon scattering in silicon films with thickness of order 100 nm", Applied Physics Letters **74**, 3005–3007 (1999) (cit. on p. 41).

[183]W. Liu and M. Asheghi, "Phonon-boundary scattering in ultrathin single-crystal silicon layers", Applied Physics Letters **84**, 3819–3821 (2004) (cit. on p. 41).

[184]X. Liu, X. Wu, and T. Ren, "In situ and noncontact measurement of silicon membrane thermal conductivity", Applied Physics Letters **98**, 174104 (2011) (cit. on p. 41).

[185]J. A. Johnson, A. A. Maznev, J. Cuffe, J. K. Eliason, A. J. Minnich, T. Kehoe, C. M. Torres, G. Chen, and K. A. Nelson, "Direct measurement of room-temperature nondiffusive thermal transport over micron distances in a silicon membrane", Physical Review Letters **110**, 025901 (2013) (cit. on pp. 41, 49).

[186]J. Cuffe, J. K. Eliason, A. A. Maznev, K. C. Collins, J. A. Johnson, A. Shchepetov, M. Prunnila, J. Ahopelto, C. M. Sotomayor Torres, G. Chen, and K. A. Nelson, "Reconstructing phonon mean-free-path contributions to thermal conductivity using nanoscale membranes", Physical Review B **91**, 245423 (2015) (cit. on p. 41).

[187]M. Kim, J. H. Seo, U. Singisetti, and Z. Ma, "Recent advances in free-standing single crystalline wide band-gap semiconductors and their applications: GaN, SiC, ZnO, β-Ga2O3, and diamond", Journal of Materials Chemistry C **5**, 8338–8354 (2017) (cit. on p. 43).

[188]G. Huang and Y. Mei, "Assembly and Self-Assembly of Nanomembrane Materials-From 2D to 3D", Small **14**, 1703665 (2018) (cit. on p. 43).

[189]V. A. Shah, S. D. Rhead, J. E. Halpin, O. Trushkevych, E. Chávez-Ángel, A. Shchepetov, V. Kachkanov, N. R. Wilson, M. Myronov, J. S. Reparaz, R. S. Edwards, M. R. Wagner, F. Alzina, I. P. Dolbnya, D. H. Patchett, P. S. Allred, M. J. Prest, P. M. Gammon, M. Prunnila, T. E. Whall, E. H. C. Parker, C. M. Sotomayor Torres, and D. R. Leadley, "High quality single crystal Ge nanomembranes for opto-electronic integrated circuitry", Journal of Applied Physics **115**, 144307 (2014) (cit. on p. 43).

[190]A. Sikora, J. Richard, H. Ftouni, J. Richard, C. Hébert, D. Eon, F. Omnès, and O. Bourgeois, "Highly sensitive thermal conductivity measurements of suspended membranes (SiN and diamond) using a 3ω-Völklein method", Review of Scientific Instruments **83**, 054902 (2012) (cit. on p. 43).

[191]A. Sood, J. Cho, K. D. Hobart, T. I. Feygelson, B. B. Pate, M. Asheghi, D. G. Cahill, and K. E. Goodson, "Anisotropic and inhomogeneous thermal conduction in suspended thin-film polycrystalline diamond", Journal of Applied Physics **119**, 175103 (2016) (cit. on p. 43).

[192]Z. Cheng, T. Bougher, T. Bai, S. Y. Wang, C. Li, L. Yates, B. M. Foley, M. Goorsky, B. A. Cola, F. Faili, and S. Graham, "Probing Growth-Induced Anisotropic Thermal Transport in High-Quality CVD Diamond Membranes by Multifrequency and Multiple-Spot-Size Time-Domain Thermoreflectance", ACS Applied Materials and Interfaces **10**, 4808–4815 (2018) (cit. on p. 43).

[193]A. A. Balandin, "Thermal properties of graphene and nanostructured carbon materials", Nature Materials **10**, 569–581 (2011) (cit. on p. 43).

[194]D. L. Nika and A. A. Balandin, "Two-dimensional phonon transport in graphene", Journal of Physics: Condensed Matter **24**, 233203 (2012) (cit. on p. 43).

[195]E. Pop, V. Varshney, and A. K. Roy, "Thermal properties of graphene: Fundamentals and applications", MRS Bulletin **37**, 1273–1281 (2012) (cit. on p. 43).

[196]M. M. Sadeghi, M. T. Pettes, and L. Shi, "Thermal transport in graphene", Solid State Communications **152**, 1321–1330 (2012) (cit. on p. 43).

[197]Y. Wang, A. K. Vallabhaneni, B. Qiu, and X. Ruan, "Two-dimensional thermal transport in graphene: A review of numerical modeling studies", Nanoscale and Microscale Thermophysical Engineering **18**, 155–182 (2014) (cit. on p. 43).

[198]Y. Xu, Z. Li, and W. Duan, "Thermal and thermoelectric properties of graphene", Small **10**, 2182–2199 (2014) (cit. on p. 43).

[199]X. Gu and R. Yang, "Phonon transport and thermal conductivity in two-dimensional materials", Annual Review of Heat Transfer **19**, 1–65 (2016) (cit. on p. 43).

[200]X. Xu, J. Chen, and B. Li, "Phonon thermal conduction in novel 2D materials", Journal of Physics Condensed Matter **28**, 483001 (2016) (cit. on p. 43).

[201]Y. Wang, N. Xu, D. Li, and J. Zhu, "Thermal Properties of Two Dimensional Layered Materials", Advanced Functional Materials **27**, 1604134 (2017) (cit. on p. 43).

[202]X. Gu, Y. Wei, X. Yin, B. Li, and R. Yang, "Colloquium : Phononic thermal properties of two-dimensional materials", Reviews of Modern Physics **90**, 041002 (2018) (cit. on p. 43).

[203]R. Martínez-Sala, J. Sancho, J. V. Sánchez, V. Gómez, J. Llinares, and F. Meseguer, "Sound attenuation by sculpture", Nature **378**, 241–241 (1995) (cit. on p. 44).

[204]P. Ben-Abdallah and S. A. Biehs, "Near-field thermal transistor", Physical Review Letters **112**, 044301 (2014) (cit. on p. 44).

[205]K. Joulain, J. Drevillon, Y. Ezzahri, and J. Ordonez-Miranda, "Quantum Thermal Transistor", Physical Review Letters **116**, 200601 (2016) (cit. on p. 44).

[206]A. Jain, Y.-J. Yu, and A. J. H. McGaughey, "Phonon transport in periodic silicon nanoporous films with feature sizes greater than 100 nm", Physical Review B **87**, 195301 (2013) (cit. on p. 44).

[207]N. Zen, T. A. Puurtinen, T. J. Isotalo, S. Chaudhuri, and I. J. Maasilta, "Engineering thermal conductance using a two-dimensional phononic crystal", Nature Communications **5**, 3435 (2014) (cit. on p. 44).

[208]S. Alaie, D. F. Goettler, M. Su, Z. C. Leseman, C. M. Reinke, and I. El-Kady, "Thermal transport in phononic crystals and the observation of coherent phonon scattering at room temperature", Nature Communications **6**, 7228 (2015) (cit. on p. 44).

[209]J. Lim, H.-T. Wang, J. Tang, S. C. Andrews, H. So, J. Lee, D. H. Lee, T. P. Russell, and P. Yang, "Simultaneous Thermoelectric Property Measurement and Incoherent Phonon Transport in Holey Silicon", ACS Nano **10**, 124–132 (2016) (cit. on p. 44).

[210]J. Maire, R. Anufriev, R. Yanagisawa, A. Ramiere, S. Volz, and M. Nomura, "Heat conduction tuning by wave nature of phonons", Science Advances **3**, e1700027 (2017) (cit. on pp. 44, 47, 56, 57).

[211]Y. Liao, T. Shiga, M. Kashiwagi, and J. Shiomi, "Akhiezer mechanism limits coherent heat conduction in phononic crystals", Physical Review B **98**, 134307 (2018) (cit. on p. 44).

[212]J. K. Yu, S. Mitrovic, D. Tham, J. Varghese, and J. R. Heath, "Reduction of thermal conductivity in phononic nanomesh structures", Nature Nanotechnology **5**, 718–721 (2010) (cit. on pp. 44, 48).

[213]P. E. Hopkins, C. M. Reinke, M. F. Su, R. H. Olsson, E. A. Shaner, Z. C. Leseman, J. R. Serrano, L. M. Phinney, and I. El-Kady, "Reduction in the thermal conductivity of single crystalline silicon by phononic crystal patterning", Nano Letters **11**, 107–112 (2011) (cit. on p. 44).

[214]R. Anufriev and M. Nomura, "Reduction of thermal conductance by coherent phonon scattering in two-dimensional phononic crystals of different lattice types", Physical Review B **93**, 045410 (2016) (cit. on p. 44).

[215]G. Xie, Z. Ju, K. Zhou, X. Wei, Z. Guo, Y. Cai, and G. Zhang, "Ultra-low thermal conductivity of two-dimensional phononic crystals in the incoherent regime", npj Computational Materials **4**, 21 (2018) (cit. on p. 44).

[216]J. Lee, W. Lee, G. Wehmeyer, S. Dhuey, D. L. Olynick, S. Cabrini, C. Dames, J. J. Urban, and P. Yang, "Investigation of phonon coherence and backscattering using silicon nanomeshes", Nature Communications **8**, 14054 (2017) (cit. on pp. 48, 49).

[217]N. K. Ravichandran and A. J. Minnich, "Coherent and incoherent thermal transport in nanomeshes", Physical Review B **89**, 205432 (2014) (cit. on p. 48).

[218]Y. Hu, L. Zeng, A. J. Minnich, M. S. Dresselhaus, and G. Chen, "Spectral mapping of thermal conductivity through nanoscale ballistic transport", Nature Nanotechnology **10**, 701–706 (2015) (cit. on p. 49).

[219]M. E. Siemens, Q. Li, R. Yang, K. A. Nelson, E. H. Anderson, M. M. Murnane, and H. C. Kapteyn, "Quasi-ballistic thermal transport from nanoscale interfaces observed using ultrafast coherent soft X-ray beams", Nature Materials **9**, 26–30 (2010) (cit. on p. 49).

[220]J. Lee, J. Lim, and P. Yang, "Ballistic phonon transport in holey silicon", Nano Letters **15**, 3273–3279 (2015) (cit. on pp. 49, 61).

[221]A. J. Minnich, J. A. Johnson, A. J. Schmidt, K. Esfarjani, M. S. Dresselhaus, K. A. Nelson, and G. Chen, "Thermal conductivity spectroscopy technique to measure phonon mean free paths", Physical Review Letters **107**, 095901 (2011) (cit. on p. 50).

[222]L. Zeng, K. C. Collins, Y. Hu, M. N. Luckyanova, A. A. Maznev, S. Huberman, V. Chiloyan, J. Zhou, X. Huang, K. A. Nelson, and G. Chen, "Measuring Phonon Mean Free Path Distributions by Probing Quasiballistic Phonon Transport in Grating Nanostructures", Scientific Reports **5**, 17131 (2015) (cit. on p. 50).

[223]S. T. Huxtable, A. R. Abramson, C.-L. L. Tien, A. Majumdar, C. LaBounty, X. Fan, G. Zeng, J. E. Bowers, A. Shakouri, and E. T. Croke, "Thermal conductivity of Si/SiGe and SiGe/SiGe superlattices", Applied Physics Letters **80**, 1737–1739 (2002) (cit. on p. 51).

[224]S. M. Lee, D. G. Cahill, and R. Venkatasubramanian, "Thermal conductivity of Si-Ge superlattices", Applied Physics Letters **70**, 2957–2959 (1997) (cit. on p. 51).

[225]R. Venkatasubramanian, "Lattice thermal conductivity reduction and phonon localizationlike behavior in superlattice structures", Physical Review B **61**, 3091–3097 (2000) (cit. on p. 51).

[226]M. V. Simkin and G. D. Mahan, "Minimum Thermal Conductivity of Superlattices", Physical Review Letters **84**, 927–930 (2000) (cit. on p. 51).

[227]G. Chen, "Thermal conductivity and ballistic-phonon transport in the cross-plane direction of superlattices", Physical Review B **57**, 14958–14973 (1998) (cit. on p. 51).

[228]B. K. Ridley, "Optical-phonon tunneling", Physical Review B **49**, 17253–17258 (1994) (cit. on p. 51).

[229]Z. Tian, K. Esfarjani, and G. Chen, "Green's function studies of phonon transport across Si/Ge superlattices", Physical Review B **89**, 235307 (2014) (cit. on pp. 51, 52).

[230]G. Li, M. Yarali, A. Cocemasov, S. Baunack, D. L. Nika, V. M. Fomin, S. Singh, T. Gemming, F. Zhu, A. Mavrokefalos, and O. G. Schmidt, "In-Plane Thermal Conductivity of Radial and Planar Si/SiOx Hybrid Nanomembrane Superlattices", ACS Nano **11**, 8215–8222 (2017) (cit. on pp. 51, 53).

[231]Y. K. Koh, Y. Cao, D. G. Cahill, and D. Jena, "Heat-Transport Mechanisms in Superlattices", Advanced Functional Materials **19**, 610–615 (2009) (cit. on p. 51).

[232]R. M. Costescu, D. G. Cahill, F. H. Fabreguette, Z. A. Sechrist, and S. M. George, "Ultra-Low Thermal Conductivity in W/Al2O3 Nanolaminates", Science **303**, 989–990 (2004) (cit. on p. 51).

[233]B. Saha, Y. R. Koh, J. Comparan, S. Sadasivam, J. L. Schroeder, M. Garbrecht, A. Mohammed, J. Birch, T. Fisher, A. Shakouri, and T. D. Sands, "Cross-plane thermal conductivity of (Ti,W)N/(Al,Sc)N metal/semiconductor superlattices", Physical Review B **93**, 045311 (2016) (cit. on p. 51).

[234]B. Saha, A. Shakouri, and T. D. Sands, "Rocksalt nitride metal/semiconductor superlattices: A new class of artificially structured materials", Applied Physics Reviews **5**, 021101 (2018) (cit. on p. 51).

[235]V. Rawat, Y. K. Koh, D. G. Cahill, and T. D. Sands, "Thermal conductivity of (Zr,W)N/ScN metal/semiconductor multilayers and superlattices", Journal of Applied Physics **105**, 024909 (2009) (cit. on p. 51).

[236]A. Giri, J. P. Niemelä, T. Tynell, J. T. Gaskins, B. F. Donovan, M. Karppinen, and P. E. Hopkins, "Heat-transport mechanisms in molecular building blocks of inorganic/organic hybrid superlattices", Physical Review B **93**, 115310 (2016) (cit. on p. 51).

[237]F. Krahl, A. Giri, J. A. Tomko, T. Tynell, P. E. Hopkins, and M. Karppinen, "Thermal Conductivity Reduction at Inorganic-Organic Interfaces: From Regular Superlattices to Irregular Gradient Layer Sequences", Advanced Materials Interfaces **2018**, 1701692 (2018) (cit. on p. 51).

[238]A. Giri, J. P. Niemelä, C. J. Szwejkowski, M. Karppinen, and P. E. Hopkins, "Reduction in thermal conductivity and tunable heat capacity of inorganic/organic hybrid superlattices", Physical Review B **93**, 024201 (2016) (cit. on p. 51).

[239]B. Saha, Y. R. Koh, J. P. Feser, S. Sadasivam, T. S. Fisher, A. Shakouri, and T. D. Sands, "Phonon wave effects in the thermal transport of epitaxial TiN/(Al,Sc)N metal/semiconductor superlattices", Journal of Applied Physics **121**, 015109 (2017) (cit. on p. 53).

[240]B. Latour, S. Volz, and Y. Chalopin, "Microscopic description of thermal-phonon coherence: From coherent transport to diffuse interface scattering in superlattices", Physical Review B **90**, 014307 (2014) (cit. on p. 52).

[241]Y. Wang, H. Huang, and X. Ruan, "Decomposition of coherent and incoherent phonon conduction in superlattices and random multilayers", Physical Review B **90**, 165406 (2014) (cit. on p. 52).

[242]Y. Wang, C. Gu, and X. Ruan, "Optimization of the random multilayer structure to break the random-alloy limit of thermal conductivity", Applied Physics Letters **106**, 073104 (2015) (cit. on p. 52).

[243]B. Yang and G. Chen, "Partially coherent phonon heat conduction in superlattices", Physical Review B **67**, 195311 (2003) (cit. on p. 52).

[244]C. da Silva, F. Saiz, D. A. Romero, and C. H. Amon, "Coherent phonon transport in short-period two-dimensional superlattices of graphene and boron nitride", Physical Review B **93**, 125427 (2016) (cit. on p. 52).

[245]T. Zhu and E. Ertekin, "Phonon transport on two-dimensional graphene/boron nitride superlattices", Physical Review B **90**, 195209 (2014) (cit. on p. 52).

[246]X. Mu, T. Zhang, D. B. Go, and T. Luo, "Coherent and incoherent phonon thermal transport in isotopically modified graphene superlattices", Carbon **83**, 208–216 (2015) (cit. on p. 53).

[247]R. Guo, Y. D. Jho, and A. J. Minnich, "Coherent control of thermal phonon transport in van der Waals superlattices", Nanoscale **10**, 14432–14440 (2018) (cit. on p. 53).

[248]M. Verdier, D. Lacroix, S. Didenko, J. F. Robillard, E. Lampin, T. M. Bah, and K. Termentzidis, "Influence of amorphous layers on the thermal conductivity of phononic crystals", Physical Review B **97**, 115435 (2018) (cit. on p. 54).

[249]R. Yan, D. Gargas, and P. Yang, "Nanowire photonics", Nature Photonics **3**, 569–576 (2009) (cit. on p. 54).

[250]D. Li, Y. Wu, P. Kim, L. Shi, P. Yang, and A. Majumdar, "Thermal conductivity of individual silicon nanowires", Applied Physics Letters **83**, 2934–2936 (2003) (cit. on pp. 54, 55, 57).

[251]O. Bourgeois, T. Fournier, and J. Chaussy, "Measurement of the thermal conductance of silicon nanowires at low temperature", Journal of Applied Physics **101**, 016104 (2007) (cit. on p. 54).

[252]J. Lee, W. Lee, J. Lim, Y. Yu, Q. Kong, J. J. Urban, and P. Yang, "Thermal Transport in Silicon Nanowires at High Temperature up to 700 K", Nano Letters **16**, 4133–4140 (2016) (cit. on pp. 55, 57).

[253]J. M. Larkin and A. J. H. McGaughey, "Thermal conductivity accumulation in amorphous silica and amorphous silicon", Physical Review B **89**, 144303 (2014) (cit. on p. 55).

[254]J. Lim, K. Hippalgaonkar, S. C. Andrews, A. Majumdar, and P. Yang, "Quantifying surface roughness effects on phonon transport in silicon nanowires", Nano Letters **12**, 2475–2482 (2012) (cit. on p. 55).

[255]S. Mukherjee, U. Givan, S. Senz, M. De La Mata, J. Arbiol, and O. Moutanabbir, "Reduction of Thermal Conductivity in Nanowires by Combined Engineering of Crystal Phase and Isotope Disorder", Nano Letters **18**, 3066–3075 (2018) (cit. on pp. 55–57).

[256]Y. Zhao, D. Liu, J. Chen, L. Zhu, A. Belianinov, O. S. Ovchinnikova, R. R. Unocic, M. J. Burch, S. Kim, H. Hao, D. S. Pickard, B. Li, and J. T. L. Thong, "Engineering the thermal conductivity along an individual silicon nanowire by selective helium ion irradiation", Nature Communications **8**, 15919 (2017) (cit. on pp. 56, 57).

[257]A. Malhotra and M. Maldovan, "Impact of Phonon Surface Scattering on Thermal Energy Distribution of Si and SiGe Nanowires", Scientific Reports **6**, 25818 (2016) (cit. on p. 56).

[258]L. G. C. Rego and G. Kirczenow, "Quantized thermal conductance of dielectric quantum wires", Physical Review Letters **81**, 232 (1998) (cit. on p. 57).

[259]D. Liu, R. Xie, N. Yang, B. Li, and J. T. L. Thong, "Profiling Nanowire Thermal Resistance with a Spatial Resolution of Nanometers", Nano Letters **14**, 806–812 (2014) (cit. on p. 57).

[260]T. Y. Choi, D. Poulikakos, J. Tharian, and U. Sennhauser, "Measurement of thermal conductivity of individual multiwalled carbon nanotubes by the 3-ω method", Applied Physics Letters **87**, 013108 (2005) (cit. on p. 57).

[261]E. Pop, D. Mann, Q. Wang, K. Goodson, and H. Dai, "Thermal conductance of an individual single-wall carbon nanotube above room temperature", Nano Letters **6**, 96–100 (2006) (cit. on p. 57).

[262]A. Soudi, R. D. Dawson, and Y. Gu, "Quantitative heat dissipation characteristics in current-carrying GaN nanowires probed by combining scanning thermal microscopy and spatially resolved Raman spectroscopy", ACS Nano **5**, 255–262 (2011) (cit. on p. 57).

[263]G. S. Doerk, C. Carraro, and R. Maboudian, "Single nanowire thermal conductivity measurements by raman thermography", ACS Nano **4**, 4908–4914 (2010) (cit. on p. 57).

[264]J. Maire, R. Anufriev, T. Hori, J. Shiomi, S. Volz, and M. Nomura, "Thermal conductivity reduction in silicon fishbone nanowires", Scientific Reports **8**, 4452 (2018) (cit. on p. 57).

[265]A. Malhotra and M. Maldovan, "Phononic pathways towards rational design of nanowire heat conduction", Nanotechnology **30**, 372002 (2019) (cit. on p. 57).

[266]W. L. Liu, T. Borca-Tasciuc, G. Chen, J. L. Liu, and K. L. Wang, "Anisotropic Thermal Conductivity of Ge Quantum-Dot and Symmetrically Strained Si/Ge Superlattices", Journal of Nanoscience and Nanotechnology **1**, 39–42 (2001) (cit. on p. 58).

[267]J. Alvarez-Quintana, X. Alvarez, J. Rodriguez-Viejo, D. Jou, P. D. Lacharmoise, A. Bernardi, A. R. Goñi, and M. I. Alonso, "Cross-plane thermal conductivity reduction of vertically uncorrelated Ge/Si quantum dot superlattices", Applied Physics Letters **93**, 013112 (2008) (cit. on p. 58).

[268]J. L. Liu, A. Khitun, K. L. Wang, W. L. Liu, G. Chen, Q. H. Xie, and S. G. Thomas, "Cross-plane thermal conductivity of self-assembled Ge quantum dot superlattices", Physical Review B **67**, 165333 (2003) (cit. on p. 58).

[269]M. Shamsa, W. Liu, A. A. Balandin, and J. Liu, "Phonon-hopping thermal conduction in quantum dot superlattices", Applied Physics Letters **87**, 202105 (2005) (cit. on p. 58).

[270]M. L. Lee and R. Venkatasubramanian, "Effect of nanodot areal density and period on thermal conductivity in SiGeSi nanodot superlattices", Applied Physics Letters **92**, 053112 (2008) (cit. on p. 58).

[271]J. S. Kang, M. Li, H. Wu, H. Nguyen, and Y. Hu, "Experimental observation of high thermal conductivity in boron arsenide", Science **361**, 575–578 (2018) (cit. on pp. 59, 60).

[272]S. Li, Q. Zheng, Y. Lv, X. Liu, X. Wang, P. Y. Huang, D. G. Cahill, and B. Lv, "High thermal conductivity in cubic boron arsenide crystals", Science **361**, 579–581 (2018) (cit. on pp. 59, 60).

[273]F. Tian, B. Song, X. Chen, N. K. Ravichandran, Y. Lv, K. Chen, S. Sullivan, J. Kim, Y. Zhou, T.-H. Liu, M. Goni, Z. Ding, J. Sun, G. A. G. Udalamatta Gamage, H. Sun, H. Ziyaee, S. Huyan, L. Deng, J. Zhou, A. J. Schmidt, S. Chen, C.-W. Chu, P. Y. Huang, D. Broido, L. Shi, G. Chen, and Z. Ren, "Unusual high thermal conductivity in boron arsenide bulk crystals", Science **361**, 582–585 (2018) (cit. on pp. 59, 60).

[274]G. Slack, "Nonmetallic crystals with high thermal conductivity", Journal of Physics and Chemistry of Solids **34**, 321–335 (1973) (cit. on p. 60).

[275]L. Lindsay, D. A. Broido, and T. L. Reinecke, "First-principles determination of ultrahigh thermal conductivity of boron arsenide: A competitor for diamond?", Physical Review Letters **111**, 025901 (2013) (cit. on p. 60).

[276]T. Feng, L. Lindsay, and X. Ruan, "Four-phonon scattering significantly reduces intrinsic thermal conductivity of solids", Physical Review B **96**, 161201(R) (2017) (cit. on p. 60).

[277]C. Dames, "Ultrahigh thermal conductivity confirmed in boron arsenide", Science **361**, 549–550 (2018) (cit. on p. 60).

[278]K. Chen, B. Song, N. K. Ravichandran, Q. Zheng, X. Chen, H. Lee, H. Sun, S. Li, G. A. G. Udalamatta Gamage, F. Tian, Z. Ding, Q. Song, A. Rai, H. Wu, P. Koirala, A. J. Schmidt, K. Watanabe, B. Lv, Z. Ren, L. Shi, D. G. Cahill, T. Taniguchi, D. Broido, and G. Chen, "Ultrahigh thermal conductivity in isotope-enriched cubic boron nitride", Science **367**, 555–559 (2020) (cit. on p. 60).

[279]L. Shi, "Nonresistive heat transport by collective phonon flow", Science **364**, 332–333 (2019) (cit. on pp. 61, 62).

[280]C. C. Ackerman, B. Bertman, H. A. Fairbank, and R. A. Guyer, "Second Sound in Solid Helium", Physical Review Letters **16**, 789–791 (1966) (cit. on pp. 60, 61).

[281]V. Narayanamurti and R. C. Dynes, "Observation of Second Sound in Bismuth", Physical Review Letters **28**, 2278 (1972) (cit. on p. 61).

[282]T. F. McNelly, S. J. Rogers, D. J. Channin, R. J. Rollefson, W. M. Goubau, G. E. Schmidt, J. A. Krumhansl, and R. O. Pohl, "Heat pulses in NaF: Onset of second sound", Physical Review Letters **24**, 100–102 (1970) (cit. on p. 61).

[283]H. E. Jackson and C. T. Walker, "Thermal conductivity, second sound, and phonon-phonon interactions in NaF", Physical Review B **3**, 1428–1439 (1971) (cit. on p. 61).

[284]D. W. Pohl and V. Irniger, "Observation of second sound in NaF by means of light scattering", Physical Review Letters **36**, 480–483 (1976) (cit. on p. 61).

[285]B. Danilchenko, V. Poroshin, and O. Sarbei, "An observation of second sound in sapphire", Soviet Journal of Experimental and Theoretical Physics Letters **30**, 215 (1979) (cit. on p. 61).

[286]D. Ding, X. Yin, and B. Li, "Sensing coherent phonons with two-photon interference", New Journal of Physics **20**, 023008 (2018) (cit. on p. 61).

[287]A. Cepellotti, G. Fugallo, L. Paulatto, M. Lazzeri, F. Mauri, and N. Marzari, "Phonon hydrodynamics in two-dimensional materials", Nature Communications **6**, 6400 (2015) (cit. on p. 61).

[288]P. Scuracchio, K. H. Michel, and F. M. Peeters, "Phonon hydrodynamics, thermal conductivity, and second sound in two-dimensional crystals", Physical Review B **99**, 144303 (2019) (cit. on p. 62).

[289]G. Callsen, J. S. Reparaz, M. R. Wagner, R. Kirste, C. Nenstiel, A. Hoffmann, and M. R. Phillips, "Phonon deformation potentials in wurtzite GaN and ZnO determined by uniaxial pressure dependent Raman measurements", Applied Physics Letters **98**, 061906 (2011) (cit. on pp. 63, 75).

[290]G. Callsen, M. R. Wagner, J. S. Reparaz, F. Nippert, T. Kure, S. Kalinowski, a. Hoffmann, M. J. Ford, M. R. Phillips, R. F. Dalmau, R. Schlesser, R. Collazo, and Z. Sitar, "Phonon pressure coefficients and deformation potentials of wurtzite AlN determined by uniaxial pressure-dependent Raman measurements", Physical Review B **90**, 205206 (2014) (cit. on pp. 63, 75).

[291]J. S. Reparaz, K. P. Da Silva, A. H. Romero, J. Serrano, M. R. Wagner, G. Callsen, S. J. Choi, J. S. Speck, and A. R. Goñi, "Comparative study of the pressure dependence of optical-phonon transverse-effective charges and linewidths in wurtzite InN", Physical Review B **98**, 165204 (2018) (cit. on pp. 63, 75).

[292]A. R. Goñi, F. Kaess, J. S. Reparaz, M. I. Alonso, M. Garriga, G. Callsen, M. R. Wagner, A. Hoffmann, and Z. Sitar, "Dependence on pressure of the refractive indices of wurtzite ZnO, GaN, and AlN", Physical Review B **90**, 045208 (2014) (cit. on pp. 63, 75).

[293]R. Kirste, S. Mohn, M. R. Wagner, J. S. Reparaz, and A. Hoffmann, "Phonon plasmon interaction in ternary group-III-nitrides", Applied Physics Letters **101**, 041909 (2012) (cit. on p. 63).

[294]G. Callsen, M. R. Wagner, T. Kure, J. S. Reparaz, M. Bügler, J. Brunnmeier, C. Nenstiel, A. Hoffmann, M. Hoffmann, J. Tweedie, Z. Bryan, S. Aygun, R. Kirste, R. Collazo, and Z. Sitar, "Optical signature of Mg-doped GaN: Transfer processes", Physical Review B **86**, 075207 (2012) (cit. on pp. 64, 74).

[295]R. Kirste, M. P. Hoffmann, J. Tweedie, Z. Bryan, G. Callsen, T. Kure, C. Nenstiel, M. R. Wagner, R. Collazo, A. Hoffmann, and Z. Sitar, "Compensation effects in GaN:Mg probed by Raman spectroscopy and photoluminescence measurements", Journal of Applied Physics **113**, 103504 (2013) (cit. on p. 64).

[296]G. Callsen, T. Kure, M. R. Wagner, R. Butté, and N. Grandjean, "Excited states of neutral donor bound excitons in GaN", Journal of Applied Physics **123**, 215702 (2018) (cit. on pp. 64, 74).

[297]R. Kirste, R. Collazo, G. Callsen, M. R. Wagner, T. Kure, J. Sebastian Reparaz, S. Mita, J. Xie, A. Rice, J. Tweedie, Z. Sitar, and A. Hoffmann, "Temperature dependent photoluminescence of lateral polarity junctions of metal organic chemical vapor deposition grown GaN", Journal of Applied Physics **110**, 093503 (2011) (cit. on p. 64).

[298]D. Gogova, P. P. Petrov, M. Buegler, M. R. Wagner, C. Nenstiel, G. Callsen, M. Schmidbauer, R. Kucharski, M. Zajac, R. Dwilinski, M. R. Phillips, A. Hoffmann, and R. Fornari, "Structural and optical investigation of non-polar (1-100) GaN grown by the ammonothermal method", Journal of Applied Physics **113**, 203513 (2013) (cit. on p. 64).

[299]R. Kirste, M. R. Wagner, C. Nenstiel, F. Brunner, M. Weyers, and A. Hoffmann, "Effect of TMGa preflow on the properties of high temperature AlN layers grown on sapphire", physica status solidi (a) **210**, 285–290 (2013) (cit. on p. 64).

[300]C. Nenstiel, G. Callsen, F. Nippert, T. Kure, S. Schlichting, N. Jankowski, M. P. Hoffmann, A. Dadgar, S. Fritze, A. Krost, M. R. Wagner, A. Hoffmann, and F. Bechstedt, "Electronic excitations stabilized by a degenerate electron gas in semiconductors", Communications Physics **1**, 38 (2018) (cit. on pp. 64, 75).

[301]F. Nippert, S. Y. Karpov, G. Callsen, B. Galler, T. Kure, C. Nenstiel, M. R. Wagner, M. Straßburg, H. J. Lugauer, and A. Hoffmann, "Temperature-dependent recombination coefficients in InGaN light-emitting diodes: Hole localization, Auger processes, and the green gap", Applied Physics Letters **109**, 161103 (2016) (cit. on pp. 64, 65, 74).

[302]F. Nippert, M. Tollabi Mazraehno, M. J. Davies, M. P. Hoffmann, H. J. Lugauer, T. Kure, M. Kneissl, A. Hoffmann, and M. R. Wagner, "Auger recombination in AlGaN quantum wells for UV light-emitting diodes", Applied Physics Letters **113**, 071107 (2018) (cit. on p. 65).

[303]S. Schlichting, G. M. O. Hönig, J. Müßener, P. Hille, T. Grieb, S. Westerkamp, J. Teubert, J. Schörmann, M. R. Wagner, A. Rosenauer, M. Eickhoff, A. Hoffmann, and G. Callsen, "Suppression of the quantum-confined Stark effect in polar nitride heterostructures", Communications Physics **1**, 48 (2018) (cit. on pp. 65, 75).

[304]E. Poliani, M. R. Wagner, J. S. Reparaz, M. Mandl, M. Strassburg, X. Kong, A. Trampert, C. M. S. Torres, J. Maultzsch, C. M. Sotomayor Torres, A. Hoffmann, and J. Maultzsch, "Nanoscale imaging of InN segregation and polymorphism in single vertically aligned InGaN/GaN multi quantum well nanorods by tip-enhanced Raman scattering", Nano Letters **13**, 3205–3212 (2013) (cit. on pp. 65, 73).

[305]J. S. Reparaz, N. Peica, R. Kirste, A. R. Goñi, M. R. Wagner, G. Callsen, M. I. Alonso, M. Garriga, I. C. Marcus, A. Ronda, I. Berbezier, J. Maultzsch, C. Thomsen, and A. Hoffmann, "Probing local strain and composition in Ge nanowires by means of tip-enhanced Raman scattering", Nanotechnology **24**, 185704 (2013) (cit. on p. 65).

[306]E. Poliani, M. R. Wagner, A. Vierck, F. Herziger, C. Nenstiel, F. Gannott, M. Schweiger, S. Fritze, A. Dadgar, J. Zaumseil, A. Krost, A. Hoffmann, J. Maultzsch, A. Ho, J. Maultzsch, A. Hoffmann, and J. Maultzsch, "Breakdown of Far-Field Raman Selection Rules by Light-Plasmon Coupling Demonstrated by Tip-Enhanced Raman Scattering", Journal of Physical Chemistry Letters **8**, 5462–5471 (2017) (cit. on pp. 65, 73).

[307]J. Müßener, L. A. T. Greif, S. Kalinowski, G. Callsen, P. Hille, J. Schörmann, M. R. Wagner, A. Schliwa, S. Martí-Sánchez, J. Arbiol, A. Hoffmann, and M. Eickhoff, "Optical emission of GaN/AlN quantum-wires: The role of charge transfer from a nanowire template", Nanoscale **10**, 5591–5598 (2018) (cit. on pp. 65, 75).

[308]G. Callsen, A. Carmele, G. Hönig, C. Kindel, J. Brunnmeier, M. R. Wagner, E. Stock, J. S. Reparaz, A. Schliwa, S. Reitzenstein, A. Knorr, A. Hoffmann, S. Kako, and Y. Arakawa, "Steering photon statistics in single quantum dots : From one- to two-photon emission", Physical Review B **87**, 245314 (2013) (cit. on pp. 66, 75).

[309]S. Werner, J. S. Reparaz, M. R. Wagner, P. Zimmer, N. N. Ledentsov, J. Kabuss, M. R. Dachner, M. Richter, A. Knorr, C. Thomsen, and A. Hoffmann, "Decay dynamics of excitonic polarons in InAs/GaAs quantum dots", Journal of Applied Physics **110**, 074303 (2011) (cit. on p. 66).

[310]L. A. Greif, S. T. Jagsch, M. R. Wagner, and A. Schliwa, "Tuning the Emission Directionality of Stacked Quantum Dots", ACS Photonics **5**, 4838–4845 (2018) (cit. on p. 66).

[311]M. R. Wagner, G. Callsen, J. S. Reparaz, J.-H. Schulze, R. Kirste, M. Cobet, I. A. Ostapenko, S. Rodt, C. Nenstiel, M. Kaiser, A. Hoffmann, A. V. Rodina, M. R. Phillips, S. Lautenschläger, S. Eisermann, and B. K. Meyer, "Bound excitons in ZnO: Structural defect complexes versus shallow impurity centers", Physical Review B **84**, 035313 (2011) (cit. on pp. 67, 68, 74).

[312]M. R. Wagner, G. Callsen, J. S. Reparaz, R. Kirste, A. Hoffmann, A. V. Rodina, A. Schleife, F. Bechstedt, and M. R. Phillips, "Effects of strain on the valence band structure and exciton-polariton energies in ZnO", Physical Review B **88**, 235210 (2013) (cit. on pp. 68, 74).

[313]S. Lautenschlaeger, S. Eisermann, G. Haas, E. A. Zolnowski, M. N. Hofmann, A. Laufer, M. Pinnisch, B. K. Meyer, M. R. Wagner, J. S. Reparaz, G. Callsen, A. Hoffmann, A. Chernikov, S. Chatterjee, V. Bornwasser, and M. Koch, "Optical signatures of nitrogen acceptors in ZnO", Physical Review B **85**, 235204 (2012) (cit. on p. 68).

[314]F. Tuomisto, C. Rauch, M. R. Wagner, A. Hoffmann, S. Eisermann, B. K. Meyer, L. Kilanski, M. C. Tarun, and M. D. McCluskey, "Nitrogen and vacancy clusters in ZnO", Journal of Materials Research **28**, 1977 (2013) (cit. on p. 68).

[315]C. Lizandara-Pueyo, S. Siroky, M. R. Wagner, A. Hoffmann, J. S. Reparaz, M. Lehmann, and S. Polarz, "Shape Anisotropy Influencing Functional Properties: Trigonal Prismatic ZnO Nanoparticles as an Example", Advanced Functional Materials **21**, 295–304 (2011) (cit. on pp. 69, 70, 75).

[316]M. Gerigk, P. Ehrenreich, M. R. Wagner, I. Wimmer, J. S. Reparaz, C. M. Sotomayor Torres, L. Schmidt-Mende, and S. Polarz, "Nanoparticle shape anisotropy and photoluminescence properties: Europium containing ZnO as a Model Case", Nanoscale **7**, 16969–16982 (2015) (cit. on pp. 69, 70, 75).

[317]D. Lehr, M. Luka, M. R. Wagner, M. Bügler, A. Hoffmann, and S. Polarz, "Band-Gap Engineering of Zinc Oxide Colloids via Lattice Substitution with Sulfur Leading to Materials with Advanced Properties for Optical Applications like Full Inorganic", Chemistry of Materials **24**, 1771 (2012) (cit. on pp. 69, 70, 75).

[318]S. Dilger, M. Wessig, M. R. Wagner, J. S. Reparaz, C. M. Sotomayor Torres, L. Qijun, T. Dekorsy, and S. Polarz, "Nanoarchitecture effects on persistent room temperature photoconductivity and thermal conductivity in ceramic semiconductors: Mesoporous, yolk-shell, and hollow ZnO spheres", Crystal Growth and Design **14**, 4593 (2014) (cit. on pp. 69, 70, 75).

[319]R. Kirste, Y. Aksu, M. R. Wagner, S. Khachadorian, S. Jana, M. Driess, C. Thomsen, and A. Hoffmann, "Raman and Photoluminescence Spectroscopic Detection of Surface-Bound Li+O2- Defect Sites in Li-Doped ZnO Nanocrystals Derived from Molecular Precursors", ChemPhysChem **12**, 1189–1195 (2011) (cit. on pp. 69, 70, 75).

[320]C. Lizandara-Pueyo, S. Dilger, M. R. Wagner, M. Gerigk, A. Hoffmann, and S. Polarz, "Li-doped ZnO nanorods with single-crystal quality – non-classical crystallization and self-assembly into mesoporous materials", CrystEngComm **16**, 1525–1531 (2014) (cit. on pp. 69, 70, 75).

[321]D. Lehr, M. R. Wagner, J. Flock, J. S. Reparaz, C. M. Sotomayor Torres, A. Klaiber, T. Dekorsy, and S. Polarz, "A single-source precursor route to anisotropic halogen-doped zinc oxide particles as a promising candidate for new transparent conducting oxide materials", Beilstein Journal of Nanotechnology **6**, 2161–2172 (2015) (cit. on pp. 69, 70, 75).

[322]K. Hagedorn, W. Li, Q. Liang, S. Dilger, M. Noebels, M. R. Wagner, J. S. Reparaz, A. Dollinger, J. Schmedt auf der Günne, T. Dekorsy, L. Schmidt-Mende, and S. Polarz, "Catalytically Doped Semiconductors for Chemical Gas Sensing: Aerogel-Like Aluminum-Containing Zinc Oxide Materials Prepared in the Gas Phase", Advanced Functional Materials **26**, 3424 (2016) (cit. on pp. 69, 70, 75).

[323]F. Güell, P. R. Martínez-Alanis, S. Khachadorian, R. R. Zamani, A. Franke, A. Hoffmann, M. R. Wagner, and G. Santana, "Spatially controlled growth of highly crystalline ZnO nanowires by an inkjet-Printing catalyst-Free method", Materials Research Express **3**, 025010 (2016) (cit. on pp. 69, 70, 75).

[324]F. Mohammadbeigi, T. Kure, G. Callsen, E. S. Kumar, M. R. Wagner, A. Hoffmann, and S. P. Watkins, "Influence of carbon doping and hydrogen co-doping on acceptor related optical transitions in ZnO nanowires", Semiconductor Science and Technology **32**, 045017 (2017) (cit. on pp. 69, 70, 75).

8 Acknowledgment

This work would not have been possible without the support and contributions of many colleagues and coworkers. In particular, I would like to express my gratitude to:

- Axel Hoffmann for being a constant source of support, not only for new scientific ideas but also for my professional and personal development over the past 15 years. I am thankful that he shared and encouraged my excitement about new research topics such as more recently the study of gallium oxide polymorphs, phonons in hybrid perovskites, and thermal transport in 2D materials, and I feel fortunate for the trust that he has placed in my decisions and the freedom I had to choose the topics to pursue. I am also thankful that he introduced me to his large scientific network over the years, supported my desire to establish new international collaborations, and recommended me for invited talks, advisory board and program committee positions at international conferences and workshops. It was a great joy to be part of a research environment that he always inspired by his scientific curiosity and respect for others. I am sure that I speak for many when I say that his willingness to help, his sense of responsibility, and his commitment to every member of his working group are exceptional and I am deeply grateful for the many years that I had the pleasure to work with him.

- Michael Kneissl for accepting to chair my habilitation panel, for his help in my applications for third party funding, for his support to finance a joint research lab for time-resolved spectroscopy on wide bandgap semiconductors, and for this commitment to promote the development and career advancement of "Nachwuchswissenschafter" both in his roles as speaker of the concluded collaborative research center 787 and executive director of the institute of solid state physics at TU Berlin.

- Janina Maultzsch for her continuing support and advice regarding applications and funding acquisition, support for project proposals, and for awakening my interest in 2D materials. It was a pleasure to be office "neighbors" and the corridor feels emptier without her.

- All members of the referee panel for their willingness to review this cumulative habilitation thesis and for the work and time that they put into this review.

- The professors of the institute of solid state physics M. Dähne, A. Hoffmann, M. Kneissl, S. Reitzenstein, and C. Thomsen for supporting my habilitation at TU Berlin.

- Matthew R. Phillips for welcoming me back into his lab as postdoctoral researcher and lecturer following my seven years earlier visit as exchange student, for introducing me to electron microscopy and giving me the opportunity to construct an in-situ Raman setup inside a scanning electron microscope, and for creating an amazing working environment that is cherished by students and colleagues alike and inspires scientific discussions in a social and friendly atmosphere.

- Clivia M. Sotomayor Torres for introducing me to the world of competitive European projects with monthly project meetings all over Europe, for selecting a great team of postdoctoral researcher that I had the pleasure to share offices and labs with, and for her agreement to act as host for my Marie Curie Inter European Fellowship.

- Juan Sebastian Reparaz, for the many years of inspiring scientific work and great friendship together and for convincing me to accept a postdoctoral research position at ICN2. Since our first common conference in 2006 in Mauterndorf, we have shared offices both in Berlin and Barcelona, traveled around the world to many conferences and workshops and spent countless days and nights discussing ideas for new physical effects and experimental breakthroughs. Since last year, we also share the wonderful present of having a daughter in both of our lives and I am looking forward to many more year of scientific exchange and personal friendship.

I was fortunate to work together with many talented students, PhD candidates, postdocs, and colleagues during my research times at the Technical University Berlin (TUB) and the Catalan Institute of Nanoscience and Nanotechnology (ICN2). In particular, I would like to acknowledge (in alphabetic order):

- In the groups of A. Hoffmann, J. Maultzsch, and C. Thomsen at TUB: M. Bügler, G. Callsen, M. Cobet, A. Franke, L. A. Th. Greif, L. Grote, D. Heinrich, F. Herziger, O. Hitzemann, G. Hönig, S. T. Jagsch, N. Jankowski, J. F. Ibaceta-Jaña, B. Janzen, M. Kaiser, M. Mohr, S. Kalinowski, F. Kampmann, S. Khachadorian, C. Kindel, T. Kure, E. Malguth, P. May, A. Mittelstädt, C. Nenstiel, F. Nippert, A. Pierret, E. Poliani, C. Rauch, M. Ries, P. Rosado, H.

Scheel, M. Schleuning, S. Schlichting, A. Schliwa, J.-H. Schulze, D. Seidlitz, H. Tornatzky, C. Tyborski, S. Werner, and S. Westerkamp.

- In the group of C. M. Sotomayor Torres at ICN2: F. Alzina, E. Chavez-Angel, J. Cuffe, A. El Sachat, J. Gomis-Bresco, B. Graczykowski, E. Guillotel, M. Kreuzer, D. Navarro-Urrios, J. S. Reparaz, C. D. Simão, and M. Sledzinska

I am also very grateful for the extensive support regarding daily administrative tasks, purchases, travels, outreach, and the preparation and management of projects. In particular, I would like to thank:

- At TUB: T. Kure, S. Morgner, D. Nitzsche, A. Sandersfeld, and D. Schreyer
- At ICN2: R. Andino López, N. Arias Cano, I. Caño Zafra, M. Corominas Camprubí, S. Domene Megias, E. Gómez Maza, M. González Gómez, E. Guillotel, M. Martí Barroso, A. de la Osa Chaparro, D. Torres Navarro, and J. Vela Llaurado.

Many experimental setups only achieved their full potential thanks to the innovative solutions and skills of experienced technicians. In particular, I would like to thank:

- The members of the precision mechanical workshop at TUB A. Ludewig, D. Beiße, M. Haupt, and W. Pieper.
- H. Scheel for his engagement in every new lab project, which spans the full range from intra-cavity frequency doubling alignments of laser cavities and programming microchips for motor controls to breaking through walls and hanging sand boxes at the ceiling for vibration damping.

Pursuing the broad spectrum of my research interests would not have been possible without a network of national and international collaborations. I would like to express my gratitude to the many colleagues and collaborators that I had the privilege of having worked and continue to work with (in alphabetic order):

- I. Aharonovich, J. Ahopelto, M. Albrecht, M. I. Alonso, F. Alzina, Y. Arakawa, J. Arbiol, T. P. Bartel, F. Bechstedt, F. Bertram, O. Bierwagen, D. Bimberg, G. Callsen, C. Carbonell Fernandez, A. Carmele, J.-M. Chauveau, J. Christen, R. Collazo, V. Consonni, A. Dadgar, B. Damilano, T. Dekorsy, N. Dietz†, D. Donadio, C. Draxl, M. Driess, M. Eickhoff, H. Eisele, N. Esser, M. Feneberg, G. Feuillet, R. Fornari, M. Ford, Z. Galazka, M. Garriga, W. Gehlhoff, R. Gillen, A. R. Goñi, N. Grandjean, M. Grundmann, F. Güell, A. Hierro, M. Higashiwaki, M. Hinterstein, A. Hoffmann, M. Hoffmann, K. Irmscher, S. Kako, A. Karg, S. Y. Karpov, S. Keller, R. Kiste, C. Kisielowski, M. Kneissl, A.

Knorr, M. Koch, C. Kranert, A. Krost†, W. Lambrecht, H. Lange, S. Lautenschläger, M. Lehmann, C. Lizandara-Pueyo, D. C. Look, G. Lu, H. J. Lugauer, J. L. Lyons, J. Maultzsch, P. Mazzolini, B. K. Meyer†, M. D. McCluskey, J. R. Morante, R. Muydinov, J. Müßner, C. Neumann, M. Nomura, T. Onuma, J. Ordonez-Miranda, T. Oshima, I. Ostapenko, D. Peró, M. R. Phillips, S. Polarz, M. Prunnila, A. Regoutz, S. Reich, S. Reitzenstein, J. S. Reparaz, A. V. Rodina, S. Rodt, D. J. Rogers, A. Rosenauer, J. Sann, K. Sattler, A. Schleife, A. Schliwa, G. Schmidt, L. Schmidt-Mende, M. Schubert, J. Serrano, A. Shchepetov, Z. Sitar, C. M. Sotomayor Torres, J. Speck, E. Stock, M. Straßburg, A. Strittmatter, C. Sturm, B. Szyszka, F. H. Teherani, C. Thomsen, C. Ton-That, M. Toth, F. Tuomisto, P. O. Vaccaro, J. B. Varley, L. Vines, S. Volz, H. von Wenckstern, E. Weig, T. Wernicke, M. Weyers, U. Woggon, B. Wunderle, and J. Zúñiga-Pérez.

Finally, I would like to acknowledge the funding from different sources and projects that have provided the financial basis to conduct many of the presented research works. In particular, I acknowledge funding by the following project:

- Collaborative research center 787 "Semiconductor nanophotonics: materials, models, devices" (DFG)
- Cluster of excellence "UniCat (Unifying concepts in catalysis)" (DFG)
- FP7-PEOPLE Marie Curie fellowship "Heat propagation and thermal conductivity in nanomaterials for nanoscale energy management (HeatProNano)" (EC)
- FP7-ENERGY "Membrane-based phonon engineering for energy harvesting (MERGING)" (EC)
- FP7-ICT "Nanostructured efficient white LEDs based on short-period superlattices and quantum dots (NEWLED)" (EC)

Most importantly, I am endlessly grateful for the unconditional support of my family and their interest in all aspects of my life beyond research.

My deepest gratitude goes to Marta for all her love and tremendous support. Since our path have crossed more than 6 years ago at ICN2 she has been a constant source of joy and happiness in my life. She has stimulated my ambition and helped me to get new perspectives of life, work, and academia. She is a source of incredible energy and this cummulative habilitation would have certainly taken even longer without her. Since about 3 month ago, our days and nights have been enriched with the life

of our daughter Olivia Sofia. I am endlessly grateful for the gift of her life and find myself astonished about the warmth of my heart that a joyful smile and laughter of her can cause. Already in her young age, she is a great source of motivation during my late-night working hours and I am indebted to Marta for many nights within the last weeks that she helped me to finish these last lines.